

# **Micro- and Nano-Electrostatic Force Fields: Generation, 3-Dimensional Measurement using a Novel AFM Method and Applications**

THÈSE N° 4127 (2008)

PRÉSENTÉE LE 4 JUILLET 2008

À LA FACULTE SCIENCES ET TECHNIQUES DE L'INGÉNIEUR  
LABORATOIRE D'OPTIQUE APPLIQUÉE  
PROGRAMME DOCTORAL EN SCIENCE ET GÉNIE DES MATÉRIAUX

ÉCOLE POLYTECHNIQUE FÉDÉRALE DE LAUSANNE

POUR L'OBTENTION DU GRADE DE DOCTEUR ÈS SCIENCES

PAR

**Martin JENKE**

Dipl.-Ing. (FH) in Physikalische Technik, Fachhochschule München, Allemagne  
et de nationalité allemande

acceptée sur proposition du jury:

Prof. C. Hébert, présidente du jury  
Dr P. Hoffmann, directeur de thèse  
Prof. B. Bhushan, rapporteur  
Prof. E. Meyer, rapporteur  
Prof. A. Stemmer, rapporteur



ÉCOLE POLYTECHNIQUE  
FÉDÉRALE DE LAUSANNE

Suisse  
2008



*The eternal mystery of the world is its comprehensibility... The fact that it is  
comprehensible is a miracle.*

*A. Einstein, "Physics and Reality," Journal of the Franklin Institute, March 1936*

*To my Parents*





# Abstract

Electro-static or electro-dynamic fields generated by micro- or nano-electrodes are today widely used in many different fields, such as micro- and nanogripping, "lab on a chip", and "lab in a cell", for the purpose of manipulation, separation, or analysis of micron-sized particles, cells, or single molecules. Commonly numerical simulations and Electrostatic Force Microscopy (EFM) methods, based on Atomic Force Microscopy (AFM), are used to study and predict the electrostatic force fields above produced structures. However, this measurement methods have several disadvantages. These disadvantages range from simple limitations (e.g. it is not possible to measure in three dimensions or expensive new equipment is needed) to much more serious disadvantages (e.g. missing compensation for known AFM problems, which results in wrong measurements).

In this thesis we propose a new EFM method based on simple static force distance curves, which allows measuring accurately, and simultaneously the topography, vertical electrostatic force field and attraction forces. The method is numerical simulated in 3D to study in detail, with simulations and measurements, electrostatic force fields above nanoelectrodes. To do this, we show for the first time the fabrication of interdigitated nanoelectrodes with pitches down to 50 nm with gas assisted focused ion beam milling. We present as well for the first time the fabrication of Pt coated AFM tips with radii between 50 and 600 nm, together with their calibration.

These tips not only close the gap between conventional tips with tip radii of about 10 nm and cantilevers with attached spheres. They show as well high mechanical stability, which solves a common problem in EFM, the mechanic

stability of the tip. The shape of the tip greatly influences the measurement. We demonstrate this using numerical simulations, and show that already small tip discrepancies can change the measured force up to 50 %. Moreover, we proved that changes in the relative humidity result in electrostatic force changes of up to 45 %.

We discovered that the resolution of EFM measurements on nanoelectrodes can be enhanced by using a tip radius of 2 to 2.5 times the pitch of the measured interdigitated nanoelectrode. Based on this and its influence on topography measurements, which are usually made before, in between or at the end of EFM measurements, we give hints for measurements with different tip radii.

Beside these important general improvements, discoveries and hints for EFM, we show as well some applications of our new EFM method and the before obtained results. We show that our new method can distinguish the force field caused by trapped charges in  $\text{SiO}_2$  from the force field caused by nanoelectrodes below it. This enables to study the influence of charge trapping in future semiconductor chips, which use charge trapping to store information.

Furthermore, we used our new EFM method and some gripping experiments to study electrostatic micro-and nanogripping. This experiments lead to some propositions for improvements in electrostatic micro-and nanogripping. Such as a new gripper design with gripping object size independent centering effect, which is studied using 3D numerical simulations.

# KEY-Words

SPM, AFM, EFM, force distance curves, electrostatic fields, force fields, microgripping, nanogripping, calibration of cantilevers, cantilevers with different tip radius.



# Zusammenfassung

Elektrostatische und elektrodynamische Felder die durch Mikro- oder Nanoelektroden erzeugt werden, finden heute in vielen unterschiedlichen Gebieten wie beispielsweise in „micro- and nanogripping“, „lab on a chip“ und „lab in a cell“ Verwendung. Mittels der elektrischen Felder werden Mikro- oder Nanopartikel, Zellen oder Moleküle manipuliert, separiert oder analysiert. Um die erzeugten Felder vorherzusagen und studieren zu können, verwendet man numerische Simulationen oder die Elektrostatische Kraft Mikroskopie (EFM), die auf der Raster Kraft Mikroskopie (AFM) basiert.

Die bisher verfügbaren EFM Methoden haben jedoch einige gravierende Nachteile. Diese reichen von einfachen Limitierungen (wie z.B. es ist keine Messung in 3D möglich oder ein komplett anderer neuerer und teurerer AFM Aufbau ist nötig) bis zu gravierenden Fehlern (wie z.B. keine Kompensation von bekannten AFM Messfehlern, die in falschen Resultaten münden). Im Rahmen dieser Doktorarbeit wurde eine neue EFM Messmethode entwickelt, die auf statischen Kraftkurven basiert und es erlaubt, gleichzeitig und akkurat die Topographie, das senkrechte elektrostatische Kraftfeld in 3D, und die Anziehungskraft zu messen. Diese neue Methode wurde auch numerisch simuliert (in 3D), um die elektrostatische Kraftfelder über den Nanoelektroden intensiv zu studieren.

Für diese Studien haben wir Nanokammelektroden mit bis zu einer minimalen Rasterbreite (pitch) von 50 nm mit Gas unterstütztem Ionenstrahlätzen hergestellt. Die Herstellung von 50 nm Kammelektroden ist hierbei besonders

hervor zu heben, da die Fabrikation solch kleiner Kammelektroden mittels Gas unterstütztem Ionenstrahlätzen erstmals publiziert wurde. Weiterhin haben wir zum erstem Mal erfolgreich mittels der Sputter-Deposition von Platin, metallische AFM Fühler mit Spitzenradien zwischen 100 und 600 nm herstellen und kalibrieren können. Die so erzeugten AFM Fühler schliessen die bisherige Lücke zwischen normalen AFM Fühlern mit Spitzen (Radius ca. 10 nm) und AFM Fühlern mit aufgeklebter Kugel (Radius ab 2  $\mu\text{m}$ ). Durch die neue mechanisch sehr stabile Platinspitze verändert sich der Radius während mehreren tausend durchgeführten Kraftkurven nicht mehr, was bei kommerziell erhältlichen metallisch beschichteten AFM Fühlern der Fall ist.

Die Form der AFM Spitze beeinflusst sehr stark die Kraftfeldmessung. Dies haben wir durch mehrere 3D Simulationen bewiesen. Kleine Unebenheiten in der Form können den gemessenen Kraftwert um bis zu 50 % verändern. Weiterhin haben wir festgestellt, dass eine Änderung der Luftfeuchtigkeit eine Kraftänderung um bis zu 45 % verursachen kann. Wir haben auch festgestellt, dass ein Verhältnis von 2 bis 2,5 zwischen Spitzenradius und pitch die beste Auflösung bei Kraftfeldmessungen auf Nanoelektroden ermöglicht. Basierend auf dieser Entdeckung und Ihrer Auswirkung auf topographische Messungen die normalerweise vor, während oder nach der EFM Messung erfolgen, geben wir einige Vorschläge für EFM Messungen mit AFM Spitzen mit unterschiedlichen Radien.

Neben diesen wichtigen generellen EFM Verbesserungen, Entdeckungen und Vorschlägen befassten wir uns auch mit Anwendungen der neuen EFM Methode und den erzielten Resultaten. Wir zeigen beispielsweise, dass wir mit unserer neuen Methode das Kraftfeld von Ladungen, welche in einem Oxid eingeschlossen sind, von einem Kraftfeld unterscheiden können, das durch darunter liegende Nanoelektroden erzeugt wird. Dies ermöglicht das Studium von in Oxiden eingeschlossenen Ladungen für zukünftigen Halbleiterchips die

mit neuen Technologien gefertigt werden und die diese für die Speicherung von Informationen verwenden.

Weiterhin haben wir mit unserer neuen Methode und einigen Mikrogreifer Experimenten den Prozess des elektrostatischen Mikro- und Nanogreifens untersucht. Diese Experimente resultierten in Vorschlägen um elektrostatische Mikro- und Nanogreifer zu verbessern. So haben wir ein neues Design entworfen und simuliert, das zu greifende Objekte grössenunabhängig in der Mitte zentrieren kann.

## Schlüsselworte

SPM, AFM, EFM, Kraft-Abstands- Kurven, elektrostatische Felder, Kraft Felder, Mikrogreifer, Nanogreifer, Kalibrierung von AFM cantilever, AFM cantilever mit unterschiedlichem Spitzen Radius.





# *Table of Contents*

## *Chapter 1 - Introduction*

1.1) General Introduction.....	17
1.2) Atomic Force Microscope (AFM).....	19
1.2.1) Detection Types.....	19
1.2.2) The Scanner.....	21
1.2.3) Basic AFM Modes.....	21
1.2.4) Electric Field Related AFM Modes.....	24
1.3) Focused Electron and Ion Beams (FEB / FIB).....	29
1.3.1) FEB / FIB History.....	29
1.3.2) FEB / FIB Structuring Basics.....	30
1.3.3) FEB / FIB Raster Scan Exposures.....	33
1.4) Bibliography of Chapter 1.....	34

## *Chapter 2 - Fabrication of Micro- and Nanoelectrodes*

2.1) Microelectrodes.....	39
2.2) Nanoelectrodes.....	41
2.3) Bibliography of Chapter 2.....	51

## *Chapter 3 - Experimental AFM Setup*

3.1) General Overview.....	53
3.2) Humidity Measurement and Control.....	54
3.3) AFM .....	56
3.4) Bibliography of Chapter 3.....	58

## *Chapter 4 - Coating of Cantilevers*

4.1) Cantilever with Tips.....	61
4.2) Cantilever with Spheres .....	66
4.3) Bibliography of Chapter 4.....	68

## *Chapter 5 - Cantilever Calibration*

5.1) Dimensional Methods.....	72
5.2) Dynamic Experimental Methods.....	75
5.3) Measurements and Comparison of Methods.....	78
5.4) Bibliography of Chapter 5.....	81

## *Chapter 6 - New EFM Method*

6.1) Introduction.....	85
6.2) Static FDC Basics / Balance of Forces.....	86
6.3) Static FDCs in Electric Fields .....	87
6.4) Topography.....	89
6.5) Vertical Electrostatic Force Field.....	91
6.6) Bibliography of Chapter 6.....	92

## *Chapter 7 - Numerical Simulation of the new Method*

7.1) Introduction.....	93
7.2) Our Numerical Model.....	94
7.3) Bibliography of Chapter 7.....	99

## *Chapter 8 - EFM Results: Characterisation*

8.1) Influence of Tip Shape Discrepancies.....	101
8.2) Resolution of EFM.....	104
8.3) Resolution Comparison between Force Field and Topography.....	114
8.4) Force Field of 50 nm Pitch Electrodes.....	116
8.5) Influence of Humidity on the Force Field.....	117
8.6) Analytical Force Field Description.....	120
8.7) Bibliography of Chapter 8.....	123

## *Chapter 9 - EFM Results: Hints and Interesting Aspects*

9.1) Cantilever Influence.....	125
9.2) Charge Injection.....	128
9.3) Practical Advices for Nanoelectrode Handling.....	131
9.4) Bibliography of Chapter 9.....	133

## *Chapter 10 - Micro- and Nanogripping*

10.1) Introduction.....	135
10.2) Tests for Electrostatic Microgripping.....	136
10.3) Electrostatic Gripping Measurements.....	142
10.4) Proposed Improvements for Electrostatic Gripping.....	144
10.5) Bibliography of Chapter 10.....	148

## *Chapter 11 - Conclusions and Perspectives*

## *Chapter 12 - Appendix*

12.1) SiO <sub>2</sub> .....	153
12.2) Thermal Noise Method.....	154
12.3) AFM Software.....	156
12.4) Datatreatment Software.....	162
12.5) Simulation Software.....	167

A Acknowledgments.....	173
------------------------	-----

B Scientific Publications.....	175
--------------------------------	-----

C Curriculum Vitae.....	177
-------------------------	-----



---

## Introduction

### 1.1) General Introduction

Driven by the ongoing miniaturisation in the semiconductor industry many scientific fields reach today the nano-scale ( $1 \text{ nm} = 10^{-9} \text{ m}$ ). Today we can produce structures, which are about 7000 times smaller as an adult human blood cell. Scientists speculate already about “lab in a cell” applications, where we insert nanostructures in human cells and which can influence certain parts of the cell<sup>1</sup>.

The ability to produce smaller and smaller structures creates a need of advanced analysis techniques and methods to analyse such structures. One of the important inventions of the last century is the development of the atomic force microscope (AFM) in 1986 by Binnig, Quate and Gerber<sup>2</sup>. The relative simple construction of the AFM enabled a fast spreading of AFM and with it the possibility to investigate the nano world. Today, AFM and its uncountable derivatives allow nanoscopic investigations in many different fields to a broad range of users.

However, as simple as AFM is, the obtained data are often misinterpreted. For example, most users usually interpret all AFM data as topographical information. This is correct only for one basic AFM mode (contact mode(chapter1.2.3.)) but not always correct for the other basic AFM modes (tapping / non contact mode(chapter1.2.3.)). Highly skilled users are therefore needed for the correct interpretation of AFM measurements and for

correct measurements with advanced AFM modes as magnetic force microscopy (MFM), electrostatic force microscopy (EFM) and others.

The development of AFM techniques and methods is still progressing. For example, within the electrostatic force microscopy sector exist already several measurement methods and techniques, but each of them have several disadvantages (see chapter 1.2.4.). At the same time electrostatic fields are of growing importance for different scientific fields, such as quantum electronics<sup>3,4</sup>, micro- and nanogripping<sup>5,6</sup>, “lab on a chip”<sup>7,8</sup>, and “lab in a cell”<sup>1</sup>, for the purpose of manipulation, separation, or analysis of micron-sized particles, cells, single molecules or nanotubes.

Therefore, there is a high need for an AFM method, which delivers accurate measurements in three dimensions and can be easily integrated in every high-end AFM. The challenges of such a method are that it must use available techniques, and deliver stable and accurate results. For the later, one has to improve several aspects of the EFM measurements. For example, cantilevers with a stable tip radius are needed and different surface information have to be acquired at the same time.

To test such a new method one needs to fabricate as well test structures at the nanoscale. We decided to use focused electron and ion beam methods for the fabrication of our test structures. The FEB and FIB methods have the advantage of high flexibility and are commonly used for the fabrication of prototypes in scientific research and industry. This will enable a faster transfer of several aspects of our results for further scientific or industrial research or development.

## **1.2) Atomic Force Microscope (AFM)**

Binnig, Quate and Gerber<sup>2</sup> developed in 1986 the atomic force microscope (AFM) with the aim to overcome some of the drawbacks of scanning tunnelling microscopy (STM). The Atomic force microscopy should work as well on insulating sample surfaces with a comparative resolution to STM. To reach atomic resolution with the AFM turned out to be a difficult, but not an impossible task<sup>9</sup>. Much more important today is the flexibility of the AFM. The first AFM operated only in normal environmental conditions (air, 20 - 30°C, 30 - 60 %rh) with a cantilever made of a small diamond, hand-glued onto a strip of gold foil. Today, the AFM operates under diverse physical conditions such as high or cryogenic temperature, ultra-high vacuum, controlled atmosphere or even in liquids. A wide variety of AFM cantilevers are available. The modern standard AFM cantilever is made of silicon (Si) or silicon nitride ( $\text{Si}_x\text{N}_y$ ), is between 100 and 400  $\mu\text{m}$  long, has a width between 50 and 100  $\mu\text{m}$ , and a thickness of 1 to 3  $\mu\text{m}$ . Its shape is either triangular or rectangular.

### **1.2.1) Detection Types**

Binnig, Quate and Gerber used an STM tip to determine the deflection of the AFM cantilever for the first AFM. The STM tip is placed at a short distance above the cantilever. During scanning, the tunnel current between the STM tip and cantilever is recorded and the deflection of the cantilever determined. This method offers high sensitivity, but is extremely sensitive to cantilever surface contamination. In addition, the tunnelling current can change the cantilever's effective spring constant.

For this and other reasons (complicated to build...) the method is today rarely used. In modern AFMs a laser beam is focused on the end of the cantilever. The laser beam is reflected by the cantilever's backside and one mirror before hitting a split-photodiode. Recording the motion of the laser spot on

the diode allows one to determine the deflection of the cantilever<sup>10, 11</sup> (figure 1-1). This method is much less sensitive to surface roughness and contamination on the backside of the cantilever. However, it requires cantilevers with high backside reflectivity and is less sensitive ( $1 \times 10^{-13} \text{ m/Hz}^{1/2}$ )<sup>12</sup> than the STM tip method.

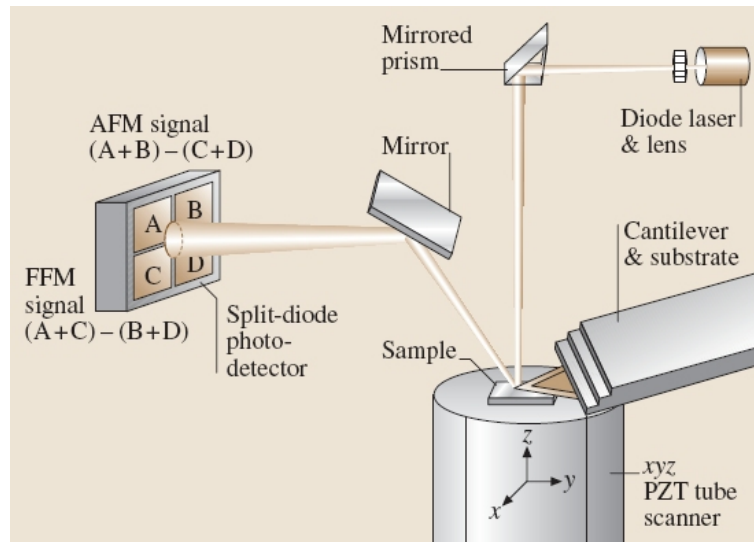


Figure 1-1: Sketch of an AFM with split-detector<sup>11</sup>.

For a higher sensitivity ( $1.7 \times 10^{-13} \text{ m/Hz}^{1/2}$ )<sup>12</sup> the laser – reflection setup is changed to a laser interferometry setup. The laser beam is focused again on the backside of a cantilever, but on the way back it interferes with a reference beam producing an interference pattern. The cantilever deflection is measured by observing the variation in the intensity of the interference pattern.

The ongoing miniaturisation allows one to fabricate AFMs with laser – reflection detection set-up in only hand filling size and with a mass of only a few 100 grams. This has led to a nearly complete vanishing of the piezoresistive cantilever deflection detection method, which was a long time method of choice if space is limited. There, in the arms of the cantilever embedded piezoresistors measure the deflection of the cantilever<sup>13</sup>.

The deflection changes are detected as resistance changes of the



piezoresistive layer using a Wheatstone bridge. This method is still used for special cases, like vacuum or light sensitive systems.

### **1.2.2) The Scanner**

Today, PZT ceramic (Pb-Zr-Ti-O) piezoelectric tube scanners are usually used for the cantilever movement in x, y, z. Depending on the scanner design and type the scanner can perform movements from a few micrometers to several hundred micrometers with a precision down to a few nm. Piezoelectric materials however have three major problems: hysteresis, non-linearity and creep. These problems can be corrected during post-processing or by using detectors that allow one to track the real movement of the scanner and correct it using a feedback loop. For the latter strain gauges<sup>14</sup> are fixed to the x, y and z-piezoes, and the movement of the piezos is corrected in a closed loop. Strain gauges have less than 0.5% non-linearity and no hysteresis.

### **1.2.3) Basic AFM Modes**

The variety of AFM modes is today endless. However, there exist three basic AFM modes, which are commonly used. These are the contact, non contact and tapping modes. The modes differ mainly in the distance of the tip from the surface and whether the cantilever vibrates or not.

#### Contact Mode

In contact mode, the AFM tip touches the surface and doesn't vibrate. Within this mode the AFM generates images by operating in two different configurations: constant-height (figure 1-2 (b)) or constant-force (figure 1-2 (a)). In constant-height mode, the spatial variation of the cantilever deflection is used to construct directly a topographical image of the surface.

This mode is usable for acquiring atomic-scale images of flat surfaces, but not for rough surfaces, where the AFM tip can be easily damaged.

In constant-force mode, the cantilever's deflection signal is fed into the input of a feedback circuit. The feedback circuit moves the piezo-scanner up and down in the z-direction and tries to keep the cantilever deflection constant. The z-piezo-scanner signal therefore corresponds to the topography of the sample. Both modes can be used in different environments, including liquids. This is one of the reasons why this mode is the most used AFM mode.

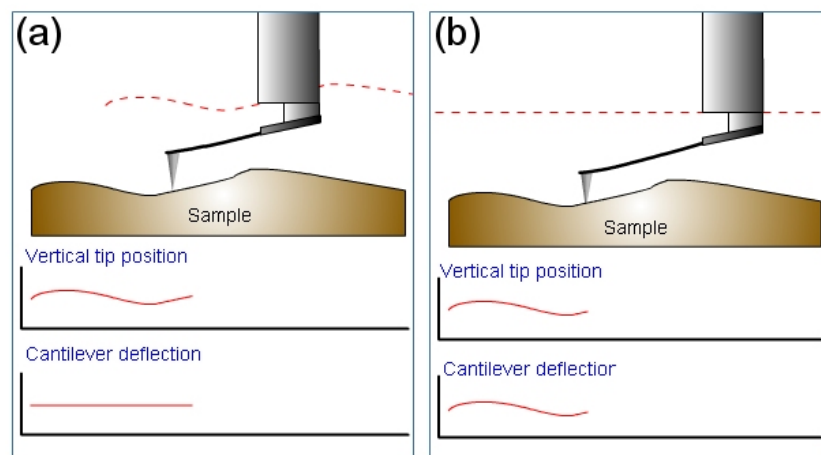


*Figure 1-2: Contact AFM modes: (a) Constant force mode. (b) Constant height mode<sup>15</sup>.*

### Non-Contact Mode

Non-contact AFM (NC-AFM) is a group of related techniques in which the cantilever is actively oscillated with a piezo-actuator near the surface, usually with a frequency close to or at one of its resonance frequencies. Force interactions between the tip and the sample surface, more precisely their gradient<sup>16</sup>, change the resonance frequency, oscillating amplitude and phase of the cantilever. These changes are tracked and used to control the tip-sample distance. A feedback loop is used to maintain either the resonant frequency (frequency modulation mode)<sup>17</sup> (figure 1-3) or the oscillating amplitude (amplitude modulation mode)<sup>18</sup> constant by moving the scanner in the vertical direction. Whereas, the frequency modulation mode is much

more sensitive as the amplitude modulation mode, because the frequency modulation mode is adapted for high-Q (quality) AFM measurements in vacuum. However, the z-piezo movement recorded with both modes corresponds to force changes. These force changes are often interpreted as height changes. This interpretation is not correct because there exist many reasons for interaction force changes beside height changes (e.g. different materials, charging...).

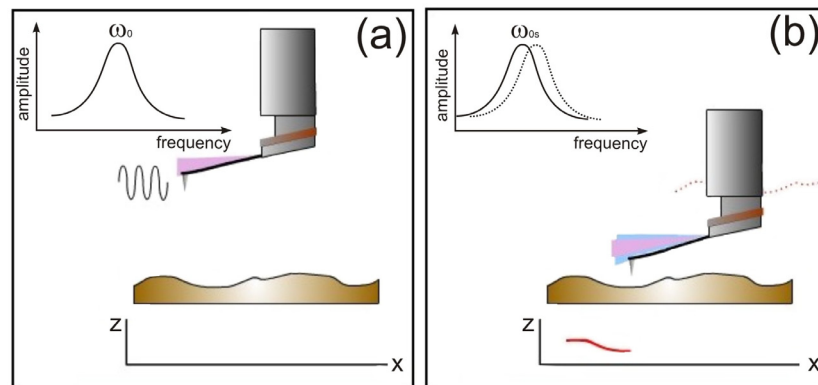


*Figure 1-3: Non contact AFM frequency modulation mode: (a) The cantilever is far from the surface and excited at its resonance frequency ( $\omega_0$ ). (b) The cantilever approaches the sample until a before defined tip to sample surface distance is reached. The cantilever scans at this distances the sample surface. Topographical variations during this scanning result in surface force gradient and cantilever resonance frequency changes. A FM demodulator detects the resonance frequency changes and adjust the tip to sample distance to maintain the original resonance frequency ( $\omega_0$ ).*

### Semicontact / Tapping / Intermittent Contact Mode

In the tapping mode (figure 1-4) the cantilever is again oscillated close to the first of its resonance modes. In contrast to non-contact AFM the tip is hitting the surface. The sample is scanned similarly to the non-contact mode using a feedback loop that controls the height according to the amplitude. Tapping mode AFM is often used to measure material properties and biological samples. The reason for the latter is that the mode was adapted for working in liquid environment<sup>19</sup>.

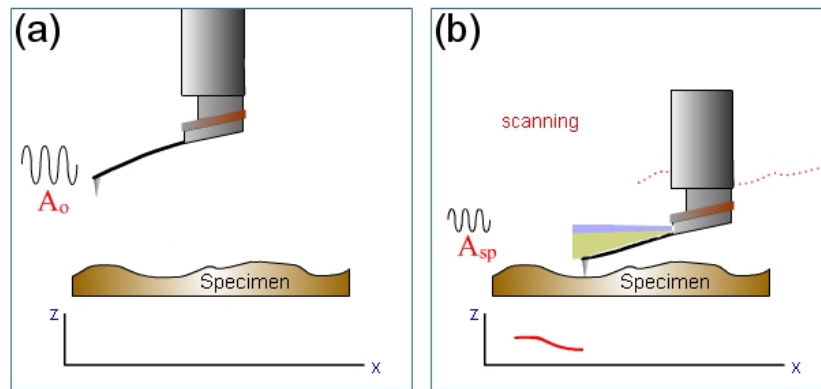


*Figure 1-4: Tapping AFM mode: (a) The cantilever is far (several  $\mu\text{m}$ ) from the surface. No damping due to tip-surface interaction forces. (b) When the cantilever approaches the sample surface, the surface force gradient increases. The cantilever vibration is damped. In contrast to the non-contact mode, the cantilever approaches now further until the tip touches the sample surface<sup>15</sup>.*

## 1.2.4) Electric Field Related AFM Modes

In addition to the presented basic AFM modes there exist several other AFM modes. In the following I present a few AFM modes for the measurement of electric fields, which are important for this work.

### Non-Contact Electric Force Microscopy (EFM)

EFM is used to measure electric fields on surfaces. The fields are usually generated by structures on or under a sample surface. These structures often cause surface topography changes. In order to compensate for these topography changes, two-pass techniques are used (figure 1-5). With the first scan the topography is measured using the AFM tapping mode. For the second scan the AFM tip is retracted to a previously defined distance from the surface. During the scan the z-piezo follows the previously measured topography profile performing a non-contact mode scan with an applied voltage between tip and surface. As result the amplitude changes correspond to the electrical potential distribution on the surface at this

distance. The obtained images are determined by the capacitive tip-sample electric force derivative<sup>20</sup>. As a result non-contact EFM has a higher resolution than the often used Scanning Kelvin Microscopy (SKM).

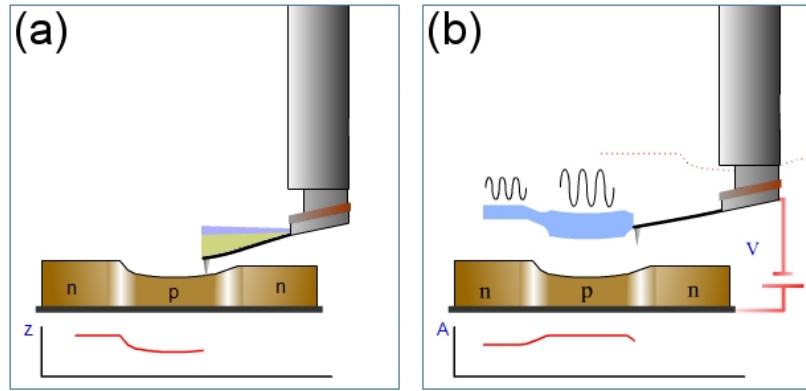


*Figure 1-5: Non-Contact Electric Force Microscopy (EFM): (a) 1st pass: Sample profile acquisition with tapping mode scan. (b) 2nd pass: Surface potential acquisition by applying a dc voltage (V) between tip and substrate*

### Scanning Kelvin Microscopy (SKM)<sup>20</sup>

Scanning Kelvin Microscopy is a two pass or one pass technique similar to non-contact EFM. At the two pass technique one obtains the topography with the first pass (figure 1-6 (a)). At the second pass (figure 1-6 (b) / (c)) the topography recorded with the first pass is retraced at a set distance from the sample surface. During the second pass the cantilever is no longer excited mechanically but electrically by applying a voltage ( $V_{tip}$ ) with DC and AC components between tip and substrate.

$$V_{tip} = V_{dc} + V_{ac} \sin(\omega t) \quad \text{Eq. 1-2}$$

The resulting capacitive force ( $F_{cap}$ ) between tip and a surface at potential ( $V_s$ ) is:

$$F_{cap} = \frac{1}{2} (V_{tip} - \phi(x))^2 \left( \frac{dC}{dz} \right) \quad \text{Eq. 1-3}$$

where  $C(z)$  is the tip-surface capacitance and  $\phi(x)$  the surface potential. The

resulting first harmonic force is:

$$F_{cap} = \left( \frac{dC}{dz} (V_{dc} - \phi(x) V_{ac}) \sin(\omega t) \right) \quad \text{Eq. 1-4}$$

The feedback loop changes during the SKM measurement the DC tip potential  $V_{dc}$  until the  $\omega$  component vanishes, e.g.  $V_{dc}(x)$  becomes equal to  $\phi(x)$ . Therefore,  $V_{dc}(x)$  reflects the surface potential distribution on the sample.

The one pass technique is similar to the two pass technique. One applies only an additional small AC-bias, which excites a higher eigenmode as used for the surface potential measurement. This higher eigenmode can now be used to detect in the same non contact scan the surface potential and the topography.

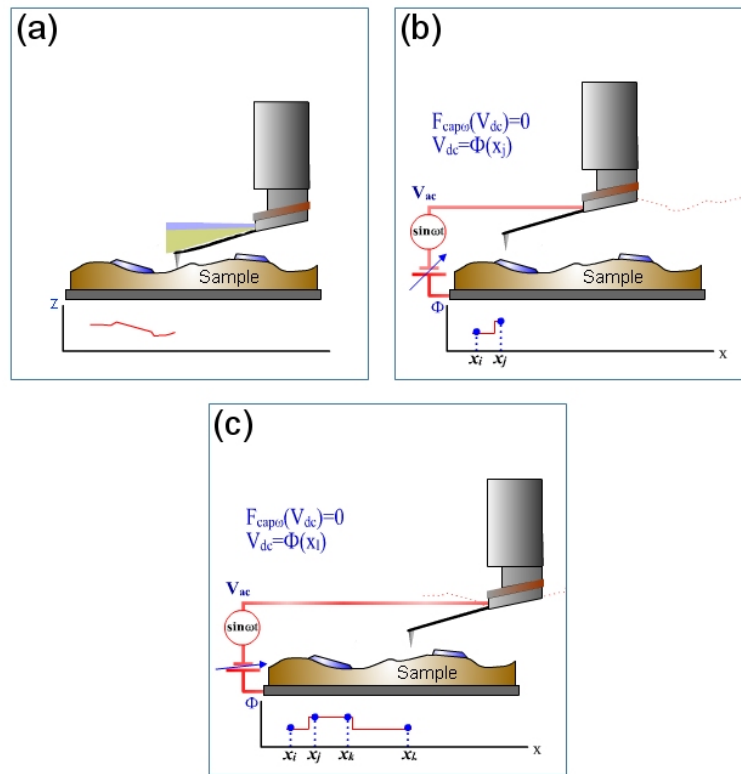


*Figure 1-6: Scanning Kelvin Probe Microscopy: (a) 1st pass: Sample profile acquisition with tapping mode scan. (b) (c) 2nd pass: Surface potential acquisition by applying a voltage ( $V_{tip}$ ) with DC and AC components between tip and substrate<sup>15</sup>.*

However, non-contact EFM and SKM have several disadvantages: During acquisition it can happen that the sample shifts (e.g. due to external stimuli). In this case, topography and E-field measurements do not correlate any more, if one uses the above described two pass techniques. All dynamic AFM measurements detect usually only normal forces, but no lateral forces. Lateral forces are usually detected with static AFM methods. Furthermore, even if theoretically 3D measurements are possible with both techniques only 2D measurements in an area parallel to the sample surface are usually performed.

#### Layered / Volume Imaging or Mapping (LI)

Layered Imaging (LI)<sup>21-24</sup> (also called Volume Imaging (VI) or Mapping) uses periodically performed static force distance curves (FDCs). For a FDC the cantilever is moved to a distance  $z_x$  above the surface. The cantilever approaches the surface from this position until the tip touches it and a previously defined deflection value is reached. At this moment the movement is reversed and the cantilever moves back to position  $z_x$ . During the movement, the cantilever deflection is monitored. From the deflection, the tip-sample force can be determined. The surface force is the sum of all long (e.g. electrostatic) and short range surface forces (e.g. Van der Waals) above the sample. The disadvantages of this method are: 1.) The surface forces can not be separated; 2.) Usually no corrections on the obtained data are performed; 3.) No topographical information are included.

#### Pulsed Force Mode (PFM)

The group of Marti et al.<sup>25 26</sup> introduced around 1997 the pulsed force mode (PFM). In the PFM a sinusoidal voltage is used to modulate the z-piezo of the AFM leading to oscillation amplitudes of typically 20–500 nm at a frequency of 100 Hz–2 kHz (up to 50kHz in the Ptak mode<sup>27</sup>). The average distance between tip and sample is adjusted such that the tip is in contact with the sample at

the lowest point of the oscillation and reaches a defined maximum deflection at the highest point of the oscillation. In principle this allows recording static force curves at high frequency (figure 1-7 (a)). Due to the fast cycling the cantilever performs a free oscillation after each cycle (figure 1-7 (b)). This oscillation plus the information from the FDC and the z-piezo allows one to obtain topography, adhesion and cantilever stiffness simultaneously. The mode has been developed further by Stifter, Sun, Krotil and others<sup>28-31</sup>. The latest development was published 2006 by Ptak<sup>27</sup>. His work was done in collaboration with one of the biggest AFM producers (Veeco) and allows high rate PFM. This work is the reason for the integration of this mode into commercial AFMs in 2006 / 07. The mode allows high speed, full FDC recording, with simultaneous topography and hardness measurements. However, like all method's this method has its disadvantages. Similar to the non-contact mode, the cantilever stiffness has to be higher than for normal contact or FDC measurements, which results in less sensitivity.

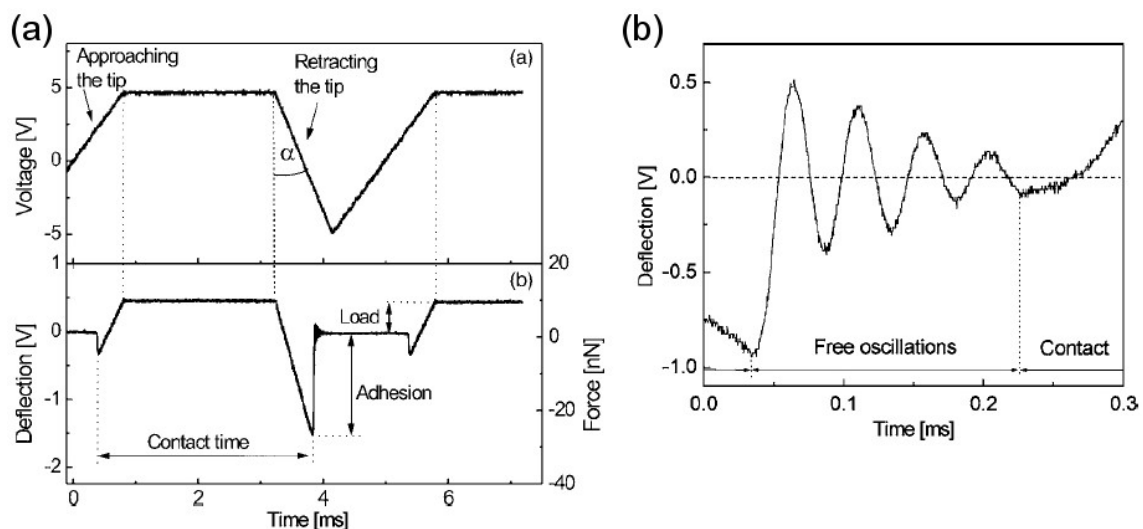


*Figure 1-7: Pulsed force mode: (a) top: Voltage signal applied on z-piezo. bottom: Resulting deflection signal. (b) The cantilever oscillates freely with its resonance frequency the first milliseconds after the detachment from the sample surface.*

As in all high speed or dynamic AFM modes the cantilever tip is quickly damaged. In addition, for the latest development<sup>27</sup> a special cooled z-piezo is used in combination with an extremely fast data treatment, to obtain high



acquisition rates. This makes it necessary to buy an AFM specially built for this mode.

Regarding this work, the new Ptak<sup>27</sup> method already includes some of the advantages of our new method, which is presented in the next chapters. However, it demonstrates as well the importance of this work and of static force distance curves in general, which are during recent years treated with less importance than dynamic FDCs. In addition, our new method includes additional procedures. In fact, an integration of our new method into PFM is possible and will result in new possibilities for both techniques.

### **1.3) Focused Electron and Ion Beams (FEB / FIB)**

#### **1.3.1) FEB / FIB History**

Focused electron beams (FEB) are routinely used today in Scanning Electron Microscopes (SEMs). The first SEM was constructed in the late 1930's by "von Ardenne" and was known as the "Universal Microscope"<sup>32-37</sup>. The first usable SEM however was constructed 1942 by Zworykin's at al. and had already a resolution of 50 nm<sup>38</sup>. Afterwards, SEM was for a long time forgotten by the scientific community. It took until 1962 to construct the first commercial SEMs (Cambridge Instrument Company). In the same year Oatley's team<sup>39-46</sup> started investigating potential applications of FEB, which already included etching, microfabrication and microelectronics.

Ion beam sources and Focused Ion Beams (FIBs) were developed in the 1970's to 1990's<sup>47-50</sup>. Due to the long experience with FEBs the first commercial systems were already available in the 1990's, which is fast in comparison with the time needed to produce the first commercial FEB systems. FIB systems operate in a similar fashion to a scanning electron microscope (SEM) except they use an ion beam, instead of an electron beam. FIB systems today use typically a finely focused beam of gallium ions that can be operated at low

beam currents for imaging or high beam currents for site specific sputtering, milling or deposition<sup>51-53</sup>.

### 1.3.2) FEB / FIB Structuring Basics

Both, FEB and FIB systems allow removal and deposition of materials, and photolithographical processing. Photolithography masks of modern computer chips are produced by FEB. For this, commonly a polymer layer is spin-coated on a quartz substrate with a metal layer on top. An electron beam is scanned over the surface, which changes the chemical composition of the polymer network on different parts of the mask. These parts are successively removed using chemicals. Afterwards, the non-protected metal is removed by standard dry or wet etching. E-beam lithography systems have, typically, beam energies of 20 to 100 keV and minimum beam diameters down to 1 nm. Single line widths down to 10 nm are achieved<sup>54</sup>. More complicated structures, however, have typical minimal structure sizes above 20 nm, due to proximity effects.

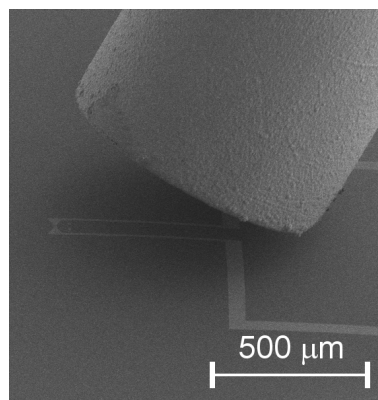


*Figure 1-8: SEM of needle for gas injection above a structured surface.*

FEB induced etching and deposition is a reaction of surface adsorbed molecules with the electron beam (figure 1-9). For this a gas is introduced

using a needle above the sample surface directly in front of the electron beam path (figure 1-8).

The vertical etch or deposition rate ( $R(r)$ ) in a simplified rotational symmetry system can be theoretical calculated as a function of the distance  $r$  from the centre of the primary beam using<sup>55</sup>:

$$R(r) = Vn(r) \int_0^{E_0} \sigma(E) f(r, E) dE \quad \text{Eq. 1-5}$$

where  $V$  is the volume of the decomposed molecule or etched atom,  $n(r)$  is the number of adsorbed molecules per surface unit,  $\sigma(E)$  is the energy dependent electron impact dissociation cross section,  $E_0$  is the energy of the incident primary electrons and  $f(r, E)$  the flux distribution.

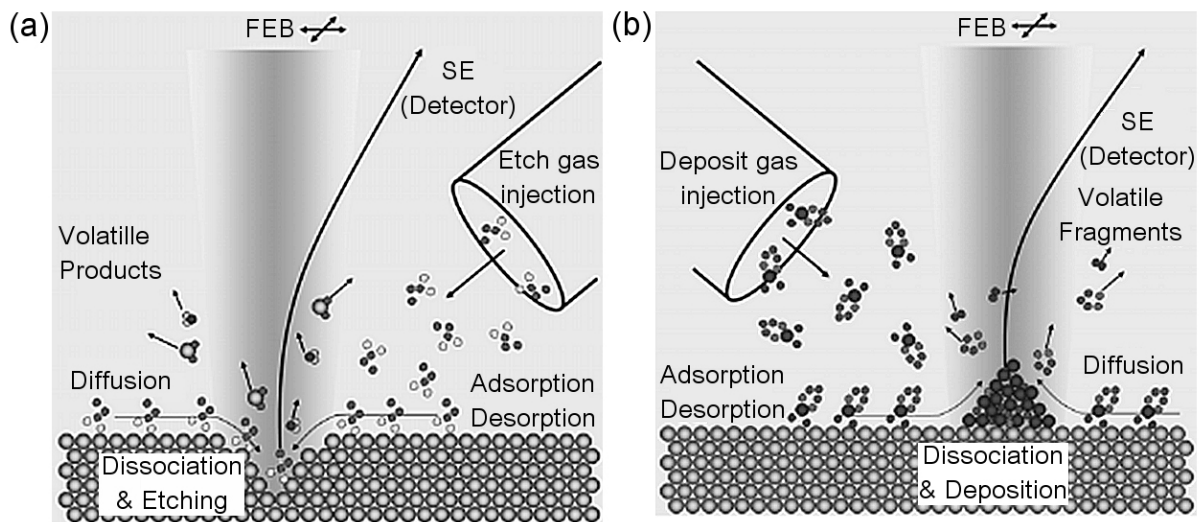


*Figure 1-9: Processes during FEB induced (a) etching: The surface-adsorbed molecules dissociate under electron impact into reactive species and react with the substrate material to create volatile compounds. (b) deposition: The non-volatile dissociation products form the deposit growing coaxially into the beam. Volatile fragments are pumped away.<sup>56</sup>*

Similar considerations apply to FIB induced etching and deposition (figure 1-10). The only difference is that one must take into account the physical sputter contribution of the much heavier ion (in comparison with the electrons).<sup>57</sup>

$$R(r) = Vn(r) \int_0^{E_0} \sigma(E) f(r, E) dE \pm S_p \quad \text{Eq. 1-6}$$

The plus sign applies for gas-assisted FIB etching whereas the minus sign stands for gas-assisted FIB deposition. A more practical expression for the etch or deposition rate can be obtained when the volume of the removed /deposited material (V), the required ion current ( $I_i$ ), and the milling / deposition time are known<sup>58</sup>:

$$R = \frac{V}{Q} = \frac{V}{I_i t} \quad \text{Eq. 1-7}$$

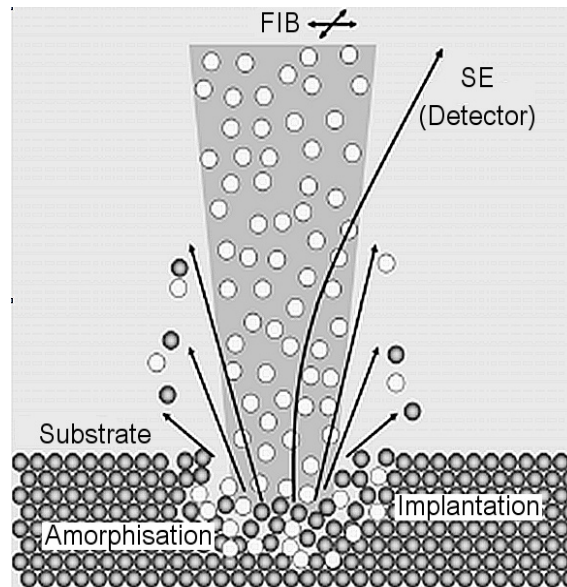


*Figure 1-10: Principle of FIB milling (or sputtering) without gas assistance. This purely physical material removal is also present during gas-assisted FIB etching, deposition and observation. Hence, the FIB damages the sample in low depth and as well implants ions during observation.<sup>56</sup>*

An important disadvantage of FIB in comparison with FEB is the implantation of ions into the substrate (etching / milling) or the deposit. A clear advantage of FIB is its high etch / milling rate in nearly all materials and the possibility to

obtain small structure sizes on charging substrates if a charge neutralization by FEB is used.

### 1.3.3) FEB / FIB Raster Scan Exposures

For obtaining complex exposure figures very often serpentine scans controlled by pixel stream files, or bitmap files are used. The beam rasters ( $\Delta x$ ,  $\Delta y$ ) a surface as shown in figure 1-11 and dwells for a time  $t_d$  ( $/t_y$ ) at each position. Hence, each pixel is exposed during  $t_d$  ( $/t_y$ ) and, in case of overlap (figure 1-11), also from adjacent pixels of multiples of  $t_d$  and  $t_y$ . After one pattern scan is completed, the beam is blanked for the refresh time  $t_r$ . The scan pattern is repeated  $p$  times ( $p$  = number of passes).

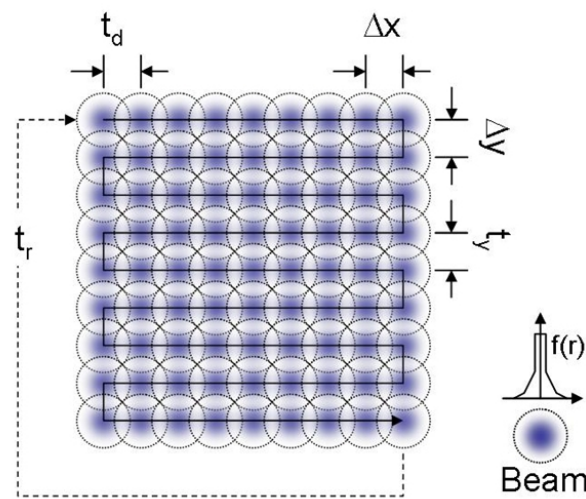


*Figure 1-11: Schematic of the beam movement during a raster scan with overlap. The beam moves in  $\Delta x/\Delta y$  steps with a dwell time  $t_d$  and a refresh time  $t_r$ .<sup>56</sup>*

Knowing the overlap, total area of the milled pattern ( $A$ ), number of pixels ( $n_w$ ), beam diameter ( $d_b$ ) and the depth / height of the milled / deposited material, one can calculate the pixel density ( $\rho_p$ ) of the bitmap<sup>58</sup>:

$$\rho_p = \frac{1 \mu\text{m} \times 100}{d_b \text{ overlap}} \quad \text{Eq. 1-8}$$

the dose (D):

$$D = \frac{n_w t_d p}{A} I_i \quad \text{Eq. 1-9}$$

and the sputtering rate (R) using equation 1-7.

## 1.4) Bibliography of Chapter 1

1. Andersson, H. and A. Van den Berg, *Microtechnologies and nanotechnologies for single-cell analysis*. Current Opinion in Biotechnology, 2004. **15**: p. 44 - 49.
2. Binnig, G., C.F. Quate, et al., *Atomic Force Microscope*. Physical Review Letters, 1986. **56**(9): p. 930 LP - 933.
3. Boussaad, S., B.A. Diner, et al., *Influence of Redox Molecules on the Electronic Conductance of Single-Walled Carbon Nanotube Field-Effect Transistors: Application to Chemical and Biological Sensing*. Journal of the American Chemical Society, 2008. **130**(12): p. 3780-3787.
4. Kinder, J.M. and E.J. Mele, *Formation of subgap states in carbon nanotubes due to a local transverse electric field*. Physical Review B (Condensed Matter and Materials Physics), 2007. **76**(19): p. 195438-11.
5. Enikov, E.T., L.L. Minkov, et al., *Microassembly experiments with transparent electrostatic gripper under optical and vision-based control*. Ieee Transactions on Industrial Electronics, 2005. **52**(4): p. 1005-1012.
6. Hesselbach, J., S. Büttgenbach, et al., *Centering electrostatic microgripper and magazines for microassembly tasks*. Microrobotics and Microassembly III, 2001. **4568**: p. 270 - 277.
7. Medoro, G., N. Manaresi, et al., *A lab-on-a-chip for cell detection and manipulation*. Ieee Sensors Journal, 2003. **3**(3): p. 317-325.
8. Verpoorte, E. and N.F. De Rooij, *Microfluidics meets MEMS*. Proceedings of the Ieee, 2003. **91**(6): p. 930-953.
9. Schwarz, U.D., H. Holscher, et al., *Atomic resolution in scanning force microscopy: Concepts, requirements, contrast mechanisms, and image interpretation*. Physical Review B, 2000. **62**(19): p. 13089-13097.
10. Meyer, E., H. Heinzelmann, et al., *Atomic Force Microscopy for the Study of Tribology and Adhesion*. Thin Solid Films, 1989. **181**: p. 527-544.

11. Bhushan, B., *Springer Handbook of Nanotechnology*. 2004, Berlin Heidelberg New York: Springer Verlag.
12. Putman, C.A.J., B.G. De Grooth, et al., *A detailed analysis of the optical beam deflection technique for use in atomic force microscopy*. Journal of Applied Physics, 1992. **72**(1): p. 6-12.
13. Yuan, C.W., E. Batalla, et al., *Low-Temperature Magnetic Force Microscope Utilizing a Piezoresistive Cantilever*. Applied Physics Letters, 1994. **65**(10): p. 1308-1310.
14. IPC Systems Ltd. *THE STRAIN GAUGE*. 2008; <http://www.sensorland.com/HowPage002a.html>.
15. NTMDT. *AFM modes*. 2008; [www.ntmdt.com](http://www.ntmdt.com)
16. Wickramasinghe, H.K., *Scanning Probe Microscopy - Current Status and Future-Trends*. Journal of Vacuum Science & Technology a-Vacuum Surfaces and Films, 1990. **8**(1): p. 363-368.
17. Albrecht, T. R., P. Grütter, et al., *Frequency modulation detection using high-Q cantilevers for enhanced force microscope sensitivity*. Journal of Applied Physics, 1991. **69**(2): p. 668-673.
18. Martin, Y., C.C. Williams, et al., *Atomic Force Microscope Force Mapping and Profiling on a Sub 100-Å Scale*. Journal of Applied Physics, 1987. **61**(10): p. 4723-4729.
19. Hansma, P.K., J.P. Cleveland, et al., *Tapping Mode Atomic-Force Microscopy in Liquids*. Applied Physics Letters, 1994. **64**(13): p. 1738-1740.
20. Nonnenmacher, M., M.P. Oboyle, et al., *Kelvin Probe Force Microscopy*. Applied Physics Letters, 1991. **58**(25): p. 2921-2923.  
Stark, R. W., Naujoks, N., et al., *Multifrequency electrostatic force microscopy in the repulsive regime*. Nanotechnology, 2007. **18**(6): 065502.
21. Taboada-Serrano, P., V. Vithayaveroj, et al., *Surface charge heterogeneities measured by atomic force microscopy*. Environmental Science & Technology, 2005. **39**(17): p. 6352-6360.
22. Jiao, Y. and T.E. Schaffer, *Accurate height and volume measurements on soft samples with the atomic force microscope*. Langmuir, 2004. **20**(23): p. 10038-10045.
23. Chaiyut, N., T. Amornsakchai, et al., *Force volume imaging of defects in highly drawn high-density polyethylene*. Polymer Testing, 2007. **26**(3): p. 396-401.
24. Radmacher, M., R.W. Tillmann, et al., *From Molecules to Cells - Imaging Soft Samples with the Atomic Force Microscope*. Science, 1992. **257**(5078): p. 1900-1905.

25. RosaZeiser, A., E. Weilandt, et al., *The simultaneous measurement of elastic, electrostatic and adhesive properties by scanning force microscopy: pulsed-force mode operation*. Measurement Science & Technology, 1997. **8**(11): p. 1333-1338.
26. Krottil, H.U., T. Stifter, et al., *Pulsed force mode: a new method for the investigation of surface properties*. Surface and Interface Analysis, 1999. **27**(5-6): p. 336-340.
27. Ptak, A., M. Kappl, et al., *Modified atomic force microscope for high-rate dynamic force spectroscopy*. Applied Physics Letters, 2006. **88**(26): p. 263109-3.
28. Stifter, T., E. Weilandt, et al., *Influence of the topography on adhesion measured by SFM*. Applied Physics a-Materials Science & Processing, 1998. **66**: p. S597-S605.
29. Sun, C.H., D.E. Aston, et al., *Structural evolution of octyltriethoxysilane films on glass surfaces during annealing at elevated temperature*. Journal of Colloid and Interface Science, 2002. **248**(1): p. 96-102.
30. Krottil, H.U., T. Stifter, et al., *Combined dynamic adhesion and friction measurement with the scanning force microscope*. Applied Physics Letters, 2000. **77**(23): p. 3857-3859.
31. Krottil, H.U., T. Stifter, et al., *Concurrent measurement of adhesive and elastic surface properties with a new modulation technique for scanning force microscopy*. Review of Scientific Instruments, 2000. **71**(7): p. 2765-2771.
32. Ardenne, M., *The scanning electron microscope: Practical construction*. Zeitschrift für Technische Physik, 1938. **19**: p. 407-416.
33. Ardenne, M., *The mapping of the finest single particles, in particular of molecules, with the universal-electron microscope*. Zeitschrift Für Physikalische Chemie - Abteilung A - Chemische Thermodynamik Kinetik Elektrochemie Eigenschaftslehre, 1940. **187**: p. 1-12.
34. Ardenne, M., *Heating-super microscope with the universal-electron microscope*. Kolloid-Zeitschrift, 1941. **97**: p. 257-272.
35. Ardenne, M. and H.H. Weber, *Electron microscopic analysis of muscle protein "myosin"*. Kolloid-Zeitschrift, 1941. **97**: p. 322-325.
36. Ardenne, M., *Das Elektronen-Rastermikroskop. Theoretische Grundlagen*. Zeitschrift Für Physik, 1938. **109**: p. 553-572.
37. Ardenne, M., *Das Elektronen-Rastermikroskop. Praktische Ausführungen*. Zeitschrift Für Technische Physik, 1938. **19**: p. 407-416.
38. Zworykin, V., J. Hillier, et al., *A scanning electron microscope*. ASTM bulletin, 1942(117): p. 15-23.
39. Oatley, C.W., *The Early History of the Scanning Electron-Microscope*. Journal of Applied Physics, 1982. **53**(2): p. R1-R13.



40. Oatley, C.W., D. McMullan, et al., *The Development of the Scanning Electron-Microscope*. Advances in Imaging and Electron Physics, 1985: p. 443-482.
41. Pease, R.F.W. and W.C. Nixon, *High Resolution Scanning Electron Microscopy*. Journal of Scientific Instruments, 1965. **42**(2): p. 81-&.
42. Everhart, T.E. and R.F.M. Thornley, *Wide-Band Detector for Micro-Microampere Low-Energy Electron Currents*. Journal of Scientific Instruments, 1960. **37**(7): p. 246-248.
43. Wells, O.C., *Correction of Errors in Electron Stereomicroscopy*. British Journal of Applied Physics, 1960. **11**(5): p. 199-201.
44. Everhart, T.E., *Simple Theory Concerning the Reflection of Electrons from Solids*. Journal of Applied Physics, 1960. **31**(8): p. 1483-1490.
45. Smith, K.C.A. and C.W. Oatley, *The Scanning Electron Microscope and Its Fields of Application*. British Journal of Applied Physics, 1955. **6**(11): p. 391-399.
46. McMullan, D., J. Thewlis, et al., *An Improved Scanning Electron Microscope for Opaque Specimens*. Proceedings of the Institution of Electrical Engineers-London, 1953. **100**(75): p. 245-259.
47. Orloff, J., *High-Resolution Focused Ion-Beams*. Review of Scientific Instruments, 1993. **64**(5): p. 1105-1130.
48. Li, Z., F. Holmes, et al., *Energy-Distribution Measurement of a Gallium Liquid-Metal Ion-Source Modulated at High-Frequency by a Focused Laser-Beam*. Journal of Vacuum Science & Technology B, 1991. **9**(5): p. 2593-2595.
49. Zhou, L. and J. Orloff, *Design of a High-Resolution Focused Ion-Beam System Using Liquid-Metal Ion-Source*. Journal of Vacuum Science & Technology B, 1990. **8**(6): p. 1721-1724.
50. Benassayag, G., J. Orloff, et al., *Focused Droplet Beam from a Gold Liquid-Metal Ion-Source*. Journal De Physique, 1986. **47**(C-7): p. 389-397.
51. Reyntjens, S. and R. Puers, *A review of focused ion beam applications in microsystem technology*. Journal of Micromechanics and Microengineering, 2001. **11**(4): p. 287-300.
52. Lehrer, C., L. Frey, et al., *Limitations of focused ion beam nanomachining*. Journal of Vacuum Science & Technology B, 2001. **19**(6): p. 2533-2538.
53. Gamo, K., *Focused Ion-Beam Technology*. Vacuum, 1991. **42**(1-2): p. 89-93.
54. Saifullah, M.S.M., K.R.V. Subramanian, et al., *Sub-10 nm Electron Beam Nanolithography Using Spin-Coatable TiO<sub>2</sub> Resists*. NANO LETTERS, 2003. **3**(11): p. 1587 – 1591.

55. Dubner, A.D. and A. Wagner, *In situ measurement of ion-beam-induced deposition of gold*. Journal of Applied Physics, 1989. **65**(9): p. 3636-3643.
56. Utke, I., P. Hoffmann and J. Melngailis, *Gas assisted focused electron beam and ion beam processing and fabrication*. JVSTB 2008, (in press).
57. Dubner, A.D. and A. Wagner, *In situ measurement of ion-beam-induced deposition of gold*. Journal of Applied Physics, 1989. **65**(9): p. 3636-3643.
58. Santschi, C., M. Jenke, et al., *Interdigitated 50 nm Ti electrode arrays fabricated using XeF<sub>2</sub> enhanced focused ion beam etching*. Nanotechnology, 2006. **17**(11): p. 2722-2729.

## Fabrication of Micro- and Nanoelectrodes

Electrostatic fields can be generated by micro- and nano-electrodes of different shapes. For this thesis interdigitated comb electrodes with different pitches (/period) (figure 2-1) and active area are fabricated in order to investigate the influence of different electrode sizes on electric force field measurements. The produced pitch size ranges from  $10\text{ }\mu\text{m}$  down to  $50\text{ nm}$  and the active area size ranges from  $36\text{ mm}^2$  down to  $1\text{ }\mu\text{m}^2$ . However, for some specific applications (e.g. microgripping; chapter 11) we fabricated, as well, interdigitated electrodes with other shapes. In this chapter the applied fabrication processes are described on the example of interdigitated comb electrodes.

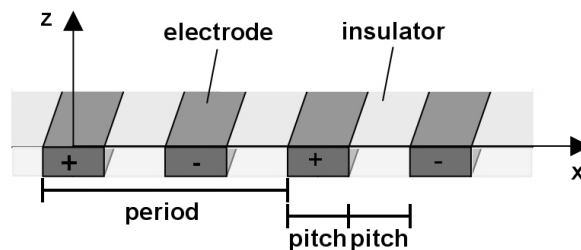


*Figure 2-1: Definition of pitch and period.*

### 2.1) Microelectrodes

The interdigitated comb microelectrodes are fabricated using the EPFL clean room facilities (CMI) with the following micro-fabrication steps: A  $50\text{ nm}$  Ti (to improve adhesion) and a  $100\text{ nm}$  Pt layer are sputtered (Spider-600, Pfeiffer Vacuum, D) onto a  $525 \pm 50\text{ }\mu\text{m}$  thick 4 inch double-side polished fused silica

wafer. The metal layer is structured using standard positive UV photolithography (MA6, Süss MicroTec Inc., USA; Shipley, Microposit S1805, USA) and a high density inductively coupled plasma etcher with chlorine chemistry (STS Multiplex ICP, Surface Technology Systems (STS), UK).

Different types of micrometer sized electrodes have been produced using this fabrication method. Interdigitated comb electrodes with active areas between  $40 \text{ mm}^2$  and  $900 \text{ } \mu\text{m}^2$  and pitches from  $15 \text{ } \mu\text{m}$  to  $1 \text{ } \mu\text{m}$  (figure 2-2 / 2-). In addition, electrodes of special shape have been produced for micro-gripping applications.

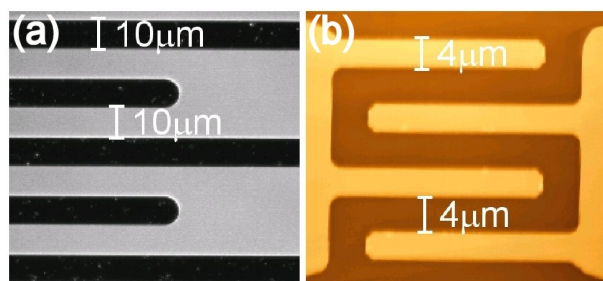


*Figure 2-2: Topview microscope image of microelectrodes with (a)  $10 \text{ } \mu\text{m}$  and (b)  $4 \text{ } \mu\text{m}$  pitch. The active area are  $40 \text{ mm}^2$  and  $900 \text{ } \mu\text{m}^2$ , respectively.*

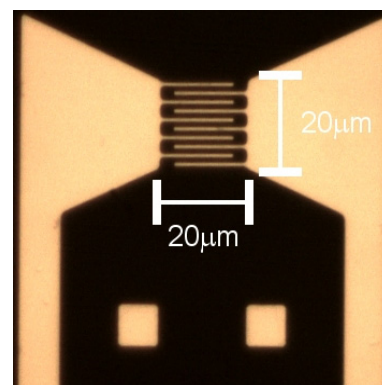


*Figure 2-3: Microelectrodes with about  $1 \text{ } \mu\text{m}$  pitch and  $400 \text{ } \mu\text{m}^2$  area. The design is optimised for gripping tests.*

The minimum pitch size we fabricated with UV (290 to 390 nm wavelength) lithography is about  $1 \text{ } \mu\text{m}$  on an area of  $400 \text{ } \mu\text{m}^2$ . The yield at this pitch size is low, 25 % (= 1.5 electrodes per wafer). For pitch sizes  $>2 \text{ } \mu\text{m}$  the yields are usually close to 100%. In contrast to these “small” area electrodes, which are limited mainly by resolution, electrodes with  $36 \text{ mm}^2$  are mainly limited by contamination due to particles and residual resist spots. Due to this, the minimum producible pitch size increases to  $5 \text{ } \mu\text{m}$ . The average yield is 50% for  $5 \text{ } \mu\text{m}$  pitch size electrodes and above. One resist spot and one particle failure are shown in figure 2-4.

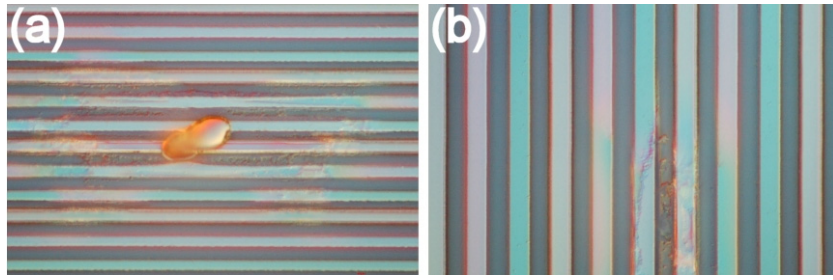


*Figure 2-4: Failures due to (a) particles and (b) remaining resist spots, on (a) 3  $\mu\text{m}$  and (b) 5  $\mu\text{m}$  pitch electrodes, respectively.*

## **2.2) Nanoelectrodes**

For the fabrication of nano-sized pitch electrodes several different fabrication methods have been tested in parallel; namely, electron beam lithography (EBL), electron beam deposition, focused ion beam milling and focused ion beam gas assisted milling (FIBgam). The best experimental results were obtained with EBL and FIBgam. Therefore, we will concentrate in the following on these two techniques. For our experiments we used a dual beam instrument, a Nova 600 NanoLab from FEI, equipped with a electron and a  $\text{Ga}^+$  ion gun. The principle of a dual beam system is described in detail elsewhere<sup>1</sup>.

### **Electron Beam Lithography (EBL)**

Based on the article "Sub-10 nm Electron Beam Nanolithography Using Spin-Coatable  $\text{TiO}_2$  Resists" by M.S.M. Saifullah<sup>2</sup> we decided to test  $\text{TiO}_2$  sol-gel resists for the fabrication of the electrodes. The advantages of these resists are their high resolution, relatively high resistance to chemicals (after full exposure) and relative insensitivity to visible light. Their disadvantages are their high sensitivity to water and the fact that the resists are not well characterised.

The used TiO<sub>2</sub> sol-gel resist is produced in dry atmosphere by mixing 1.43 g Benzoylacetone, 3 ml Tetrabutyl orthotitanate and 30 ml Pentanol. 7 ml of the resist are spin coated with 3000 rpm for 30 sec. on about 1 x 1 cm square Si-chips in standard environment (room temperature, 30 to 60 %rh). After drying for 45 min. at 80°C and subsequent 30 min. “cool down” at standard environment, the resist is “exposed” using the electron beam. The structures are developed in acetone for 10 min. and rinsed with isopropanol.

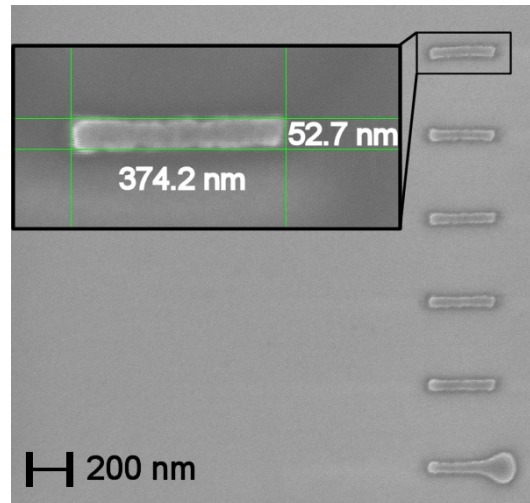


*Figure 2-5: Array of 6 lines with 52 nm width and 374 nm length.*

During the first tests we successfully fabricated reproducible lines down to about 50 nm in width using a 65 nm to 77 nm thick TiO<sub>2</sub> containing resist (figure 2-5). Despite these good results, we had problems fabricating more sophisticated and more closely spaced structures due to proximity effects. The width of exposed lines changed with their distance from the next line. Backscattered electrons are the reason for this behaviour. They “expose” our highly sensitive TiO<sub>2</sub> containing resist in an area around the primary beam. To investigate and solve this problem we had the simple idea to use lines with white to black gradients (figure 2-6). This enables one to test large dose ranges in the same run.

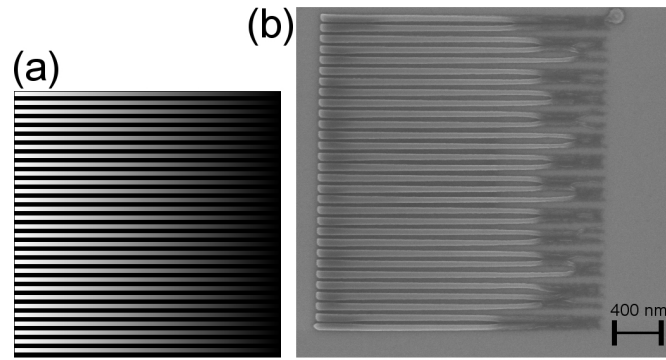


Figure 2-6: (a) Bitmap file used to fabricate (b). (b) SEM of an array of lines with 50 nm pitch. Due to the white to black gradient exposure doses from 753.29 C/m<sup>2</sup> (left) to 0 C/m<sup>2</sup> (right) are tested. (calculated using Eq. 1-9)

Using this method we found out that a dose between 450 and 600 C/m<sup>2</sup> enables fabrication on flat substrates structures down to 50 nm pitch with varying distances of 50, 100 and 200 nm. (figure 2-7)

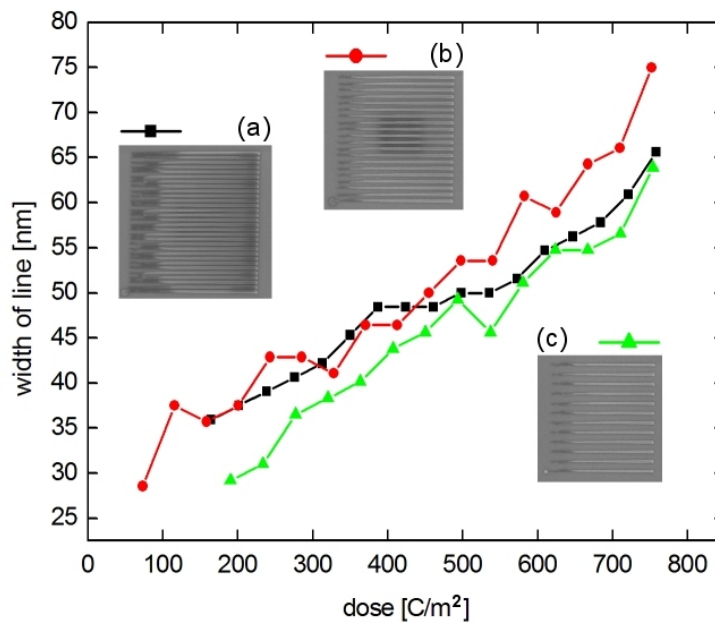


Figure 2-7: Measured line width in relation to the calculated dose. The lines are designed with 50 nm line width and varying distance. (a) 50 nm (b) 100 nm (c) 200 nm distance to the next line.

It is extremely expensive and time consuming to expose a full wafer at this resolution. Therefore, we tried to spincoat our resist on prestructured Ti-layers. This created several problems. The most serious problem is that we did not achieve a good coverage of the structures during the spin coating.

To conclude, we fabricated lines down to 50 nm in width and varying distances (down to 50 nm) to the next lines on non-structured Si-wafers. On the other hand, the spin coating of this resist on structured substrates is problematic and couldn't be solved. For this kind of substrates, we used FIBgam, which is presented next.

### **Focused Ion Beam gas assisted milling (FIBgam)**

For gas assisted focused ion beam milling we prestructured a Si-wafer using the following processes: A 50 nm Ti layer is sputtered (Spider-600, Pfeiffer Vacuum, D) on a Si-Wafer with thermal dry oxide (100nm). The Ti layer is photolithographically (MA6, Süss MicroTec Inc., USA; Shipley, Microposit S1805, USA) prestructured leaving a  $10 \times 10 \mu\text{m}^2$  Ti region that is electrically connected to two large contact pads. This region is structured (design figure 2-8) using a  $\text{Ga}^+$  focused ion beam milling with  $\text{XeF}_2$  gas assistance (Nova 600 NanoLab, FEI, USA).

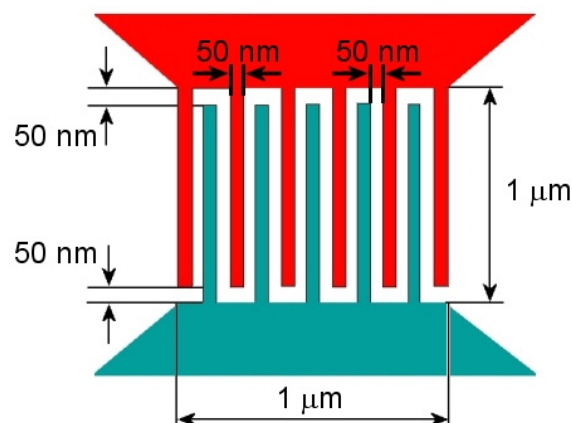


*Figure 2-8: A 50 nm pitch interdigitated electrodes design.*



For this structuring we used the following procedure and processes<sup>3</sup>:

#### a) Beam adjustment

For the fabrication of nanostructures the beam diameter and quality (astigmatism and focus) is of crucial importance, no matter if it is an electron or ion beam. In order to have a small beam diameter and reasonably short milling durations the FIBgam experiments have been carried out with an ion acceleration voltage  $U_i = 30$  kV and current set to  $I_i = 10$  pA, respectively, which results in a nominal beam diameter  $d_b$  of 12 nm (full width at half maximum, FWHM)(given by FEI).

To achieve the requested beam quality we adjusted the focus and astigmatism very carefully. Subsequent to a rough adjustment on an adapted surface feature, nano-holes and -squares with a diameter of a few hundreds of nanometers have been milled into the substrate in order to check the proper adjustment of focus and astigmatism. Analysing the milled test-structures thoroughly, slight distortions were observed due to surface charging, although the Ti-structures and the underlying Si-substrate were well grounded using a Cu-tape covered with conducting glue. An efficient charge neutralisation can be obtained by using additionally the e-beam whilst milling the nanostructures. An electron current, which is generated by the e-beam and on the order of 10 times higher than the ion current, leads in our experience to a good discharging of the substrate and solved this problem (e-beam acceleration voltage  $U_e = 10$  kV, current  $I_e = 130$  pA, dwell time  $t_d$  1  $\mu$ s).

The e-beam current  $I_e$  used for charge neutralisation was varied in the range of  $I_e = 33$  pA and  $I_e = 540$  pA in order to examine its influence on the milling process. The results revealed that the etching by the electron beam can be neglected compared to the ion induced etching. Therefore, we used for our experiments the e-beam for charge neutralisation in combination with ion induced chemical etching.

### b.) FIB XeF<sub>2</sub> milling

As mentioned in chapter 1.3., pixel controlled patterning is used in ion or electron beam structuring to fabricate complex designs. This allows the pattern to be defined in different ways, such as direct drawing of the patterns composed of a given set of basic patterns, individual control of pixels (stream files), or bitmap files (bmp). In our experiments the patterns have been defined using bitmap files. The patterning proceeds in a pixel-by-pixel movement, where for black and white pixels the ion beam is either blanked and not, respectively. For this a fast beam blanker (decay/rise time 1 ns) is used.

Knowing the overlap (50 %), the number of passes (360), the dwell time (500 ns), the total area of the milled pattern ( $0.53 \mu\text{m}^2$ ), the number of pixels ( $14.6 \times 10^3$ ), the depth  $d_s = 40 \text{ nm}$  of the structure, we can calculate the pixel density  $\rho_p = 167 \text{ pixel } \mu\text{m}^{-1}$ , the dose  $D = 5 \text{ mC cm}^{-2}$  and the sputtering rate  $R = 0.8 \mu\text{m}^3 \text{ nC}^{-1}$  using equations 1-7 to 1-9. The electrodes fabricated using these parameters are shown in figure 2-9 and 2-10. They are the first fabricated 50 nm pitch electrodes in Ti using Fibgam.

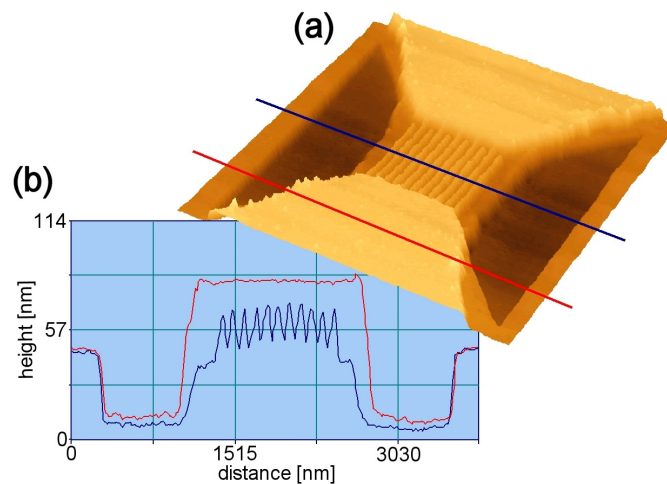


*Figure 2-9: (a) 3D reconstruction of an AFM contact scan of 50 nm pitch electrodes. (b) Two line scans taken from (a) at the indicated positions.*

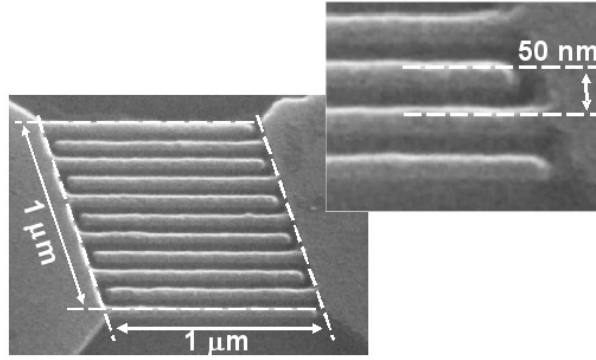


*Figure 2-10: SEM image of interdigitated nanoelectrodes of 50 nm width, 50 nm gap, and 40 nm thickness. The electrodes have been fabricated using gas enhanced etching with  $\text{XeF}_2$ . The parameters are  $I_i = 10 \text{ pA}$ ,  $U_i = 30 \text{ kV}$ ,  $t_d = 500 \text{ ns}$ , and  $p = 360 \text{ passes}$ . The sample is tilted to  $46^\circ$ .*

In order to determine the optimal refresh time ( $t_r$ ) and dwell time ( $t_d$ ) for the Ti/ $\text{XeF}_2$  system, the sputtering rate  $R$  was measured as a function of  $t_r$  and  $t_d$ , all other parameters are kept constant. This is done by milling square structures of  $1 \mu\text{m}$  length and  $500 \text{ nm}$  width into a Ti block and subsequent measurement of the removed volume by SEM (accuracy  $\pm 10 \%$ ). The  $t_r$  is composed of the scanning time  $t_s$  of one pass and the waiting time  $t_w$  for which the beam is blanked after each pass. The  $t_r$  was varied by adapting  $t_w$ , whereas  $t_s$  was kept constant.

The result of the measurements is shown in figure 2-11, the measured values are represented by dots<sup>3</sup>. The sputtering rate increases until approximately  $0.8 \mu\text{m}^3 \text{ nC}^{-1}$  for a refresh time  $t_r > 50 \text{ ms}$ . The opposite is the case for the sputtering rate versus dwell time  $t_d$ . The sputtering rate decreases rapidly with increasing dwell time.

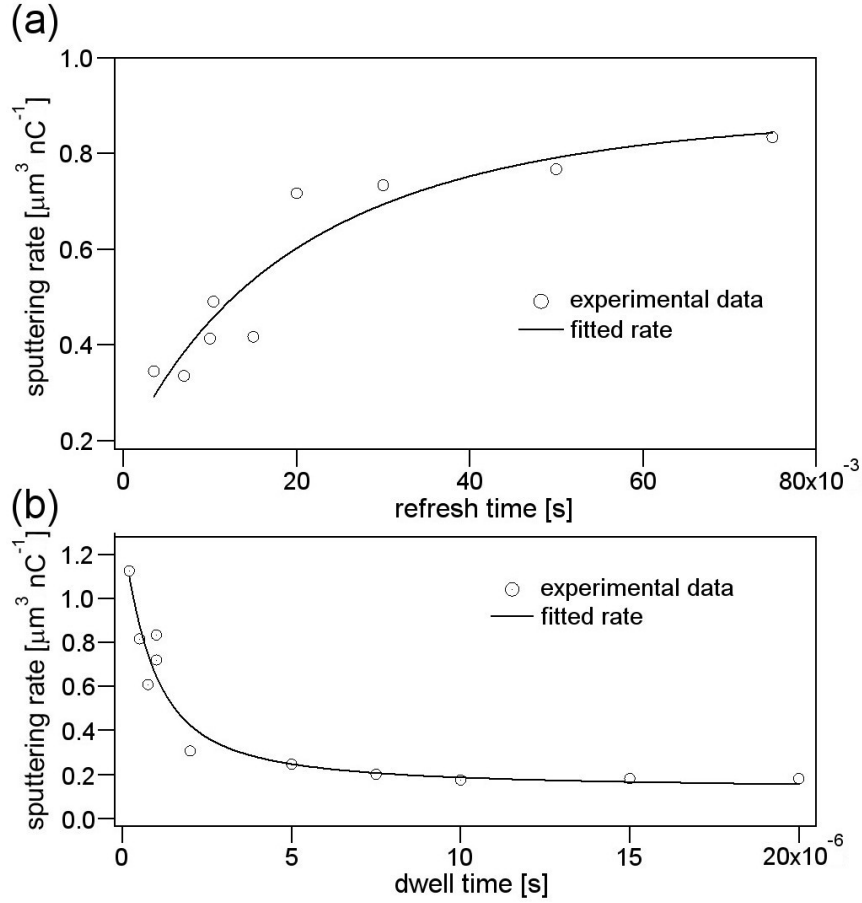


Figure 2-11: Sputtering rate  $R$  of the Ti in presence of  $\text{XeF}_2$  as a function of (a) refresh time  $t_r$  and (b) dwell time  $t_d$ . (a) Ion current  $I_i = 10 \text{ pA}$  and dwell time  $t_d = 500 \text{ ns}$  are constant and the gas flow is  $1.3 \times 10^{20} \text{ molecule cm}^{-2} \text{ s}^{-1}$ . (b) Ion current  $I_i = 10 \text{ pA}$  and refresh time  $t_r = 150 \text{ ms}$  are constant and the gas flow is  $1.3 \times 10^{20} \text{ molecule cm}^{-2} \text{ s}^{-1}$ .<sup>3</sup>

The measurements reveal that adsorption is slow compared to the surface depletion in the presence of the ion current. Consequently,  $t_d$  should be as short and  $t_r$  as long as possible. Therefore, the optimal conditions for chemical enhanced milling for Ti using  $\text{XeF}_2$  are refresh time  $t_r$  longer than 30 ms and a dwell time  $t_d$  shorter than 500 ns. For  $t_d \rightarrow \infty$  the sputtering rate tends to  $R = 0.12 \mu\text{m}^3 \text{nC}^{-1}$ , which corresponds to the physical sputtering rate. For  $t_r \rightarrow \infty$  the sputtering rate tends to the maximal sputtering rate  $R = 0.88 \mu\text{m}^3 \text{nC}^{-1}$ .

### c.) Nanoelectrodes with pitches larger than 50 nm on fused silica substrates

All 50 nm pitch electrodes are fabricated on doped Si-wafers with a SiO<sub>2</sub> layer on top, because this enables one to ground the doped Si. This helps to avoid charging of the substrate due to the ion beam. However, this creates parasitic capacitances between the metallic structures (contact pads, wires, electrodes) and the doped Si-wafer.

For nanoelectrodes with 500 nm and 200 nm pitch we used fused silica wafers instead of doped Si wafers with an SiO<sub>2</sub> layer<sup>4</sup>. This avoids the parasitic capacities between substrate and metallic structures. The disadvantage of using fused silica wafers is their charging during FIB. Therefore, fused silica substrates do not permit fabrication of very small structures. The smallest pitch size we were able to produce on fused silica substrates was 200 nm.

For the fabrication we used prestructured samples prepared as described before, prior to a FIBgam process using the following parameters: number of passes  $p = 800$ , dwell time  $t_d = 1 \mu\text{s}$ , magnification  $M = 3500$ , ion current  $I_i = 10 \text{ pA}$ , acceleration voltage  $U_i = 30 \text{ kV}$ , no i-beam spot overlap. The theoretical ion beam diameter (given by FEI) for these conditions is 12 nm. The parameters for the e-beam used for charge neutralization were: electron current  $I_e = 210 \text{ pA}$  and acceleration voltage  $U_e = 2 \text{ kV}$ . Examples of these electrodes are shown at figure 2-12.

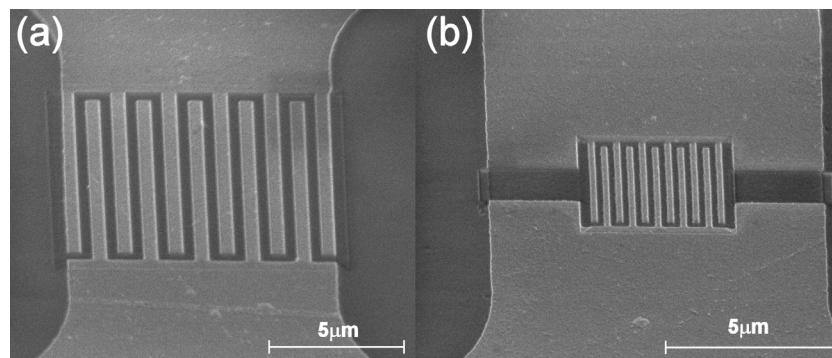


*Figure 2-12: Tilted (52°) secondary electron microscope (SEM) image of the (a) 500 nm and (b) 200 nm pitch interdigitated Ti nanoelectrodes, on fused silica substrates.*

#### d.) Electrode Coverage and Electrical Measurements

After fabrication, all electrodes are covered with a SiO<sub>2</sub> layer using RF sputtering with an O<sub>2</sub> (1 sccm) and Ar (15 sccm) gas mixture. The SiO<sub>2</sub> films obtained with this method have been investigated and compared with thermally grown SiO<sub>2</sub> films using XPS (=X-Ray photoelectron spectroscopy) and Auger spectroscopy. The Si to O ratio of a dry thermally grown film is 1 : 1.92. The ratio of the sputtered film is 1 : 1.89. Despite the discrepancy of these ratios the electrical resistance of our sputtered films was good.

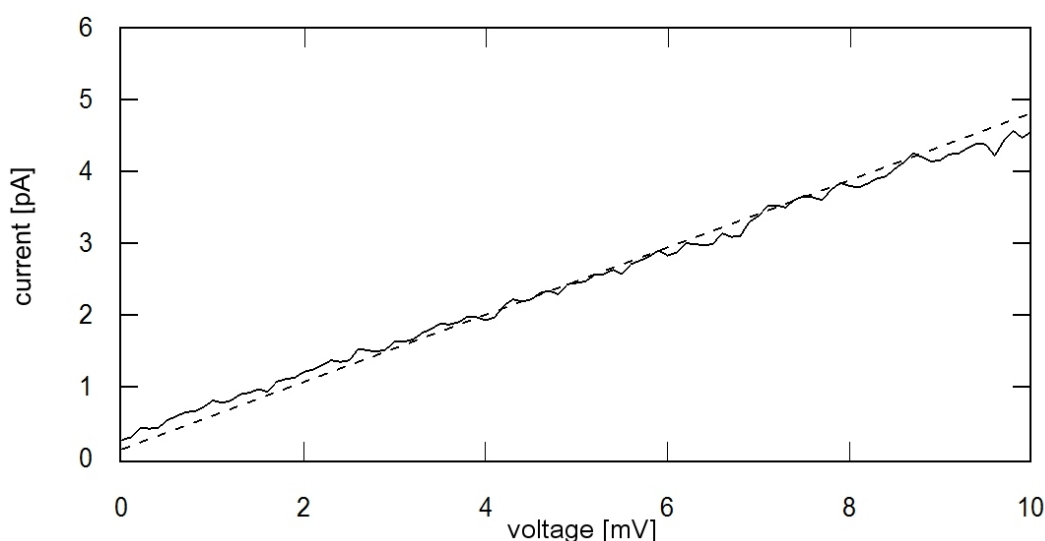


*Figure 2-13: V-I diagram for a two-point electrical measurement of 50 nm pitch interdigitated electrodes, after covering the electrodes with a protective SiO<sub>2</sub> layer. The resistance determined from this graph is  $2 \pm 1 \text{ G}\Omega$  <sup>3</sup>.*

The electrical resistance of the fabricated 50 nm, 200 nm and 500 nm pitch interdigitated electrodes was measured. The contact pads of the electrodes are connected using a manual wafer prober (Karl & Süss PM5). Voltage – Current (V-I) diagrams are taken with a precision semiconductor parameter analyser (Hewlett Packard 4156A). After SiO<sub>2</sub> coverage the 50 nm pitch electrodes showed a resistance of  $2 \pm 0.5 \text{ G}\Omega$  (Figure 2-13). The 200 and 500 nm pitch electrodes had a resistance of about  $14.8 \pm 5 \text{ T}\Omega$ , after the SiO<sub>2</sub> deposition (figure 2-14). The resistance of the 200 and 500 nm is one order of magnitude higher, but the resistance of all electrodes is high enough to

enable good EFM measurements.

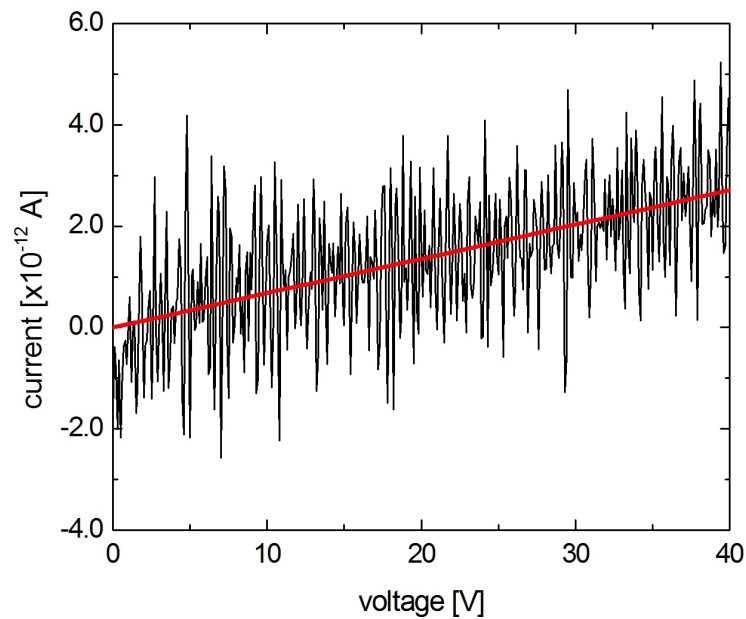


*Figure 2-14: V-I diagram for a two-point electrical measurement of 500 nm pitch interdigitated electrodes. The electrodes are covered with a 60 nm thick protective SiO<sub>2</sub> layer. The resistance of this electrode is  $14.8 \pm 10 \text{ T}\Omega$ .*

## 2.3) Bibliography of Chapter 2

1. Giannuzzi, L.A., *Introduction to Focused Ion Beam*. 2005, Berlin: Springer. 375.
2. Saifullah, M.S.M., K.R.V. Subramanian, et al., *Sub-10 nm Electron Beam Nanolithography Using Spin-Coatable TiO<sub>2</sub> Resists*. NANO LETTERS, 2003. **3**(11): p. 1587 - 1591.
3. Santschi, C., M. Jenke, et al., *Interdigitated 50 nm Ti electrode arrays fabricated using XeF<sub>2</sub> enhanced focused ion beam etching*. Nanotechnology, 2006. **17**(11): p. 2722-2729.
4. Jenke, M.G., C. Santschi, et al., *Characterization of Electrical Fields of Buried Interdigitated Nanoscale Ti-Electrode Arrays by a Novel Atomic Force Microscopy Measurement Procedure and Their Fabrication by FIB Milling*. NSTI-Nanotech2007, 2007. **4**: p. 97-100.





## Experimental AFM Setup

In this chapter an overview on the AFM setup used for our experiments and its calibration is presented. This is important for an estimation on the precision of the performed EFM measurements.

### 3.1) General Overview

Pictures and a sketch of the experimental AFM setup are shown in figure 3-1. The setup consists essentially of an AFM (Topometrix, Explorer) with linearised x, y, z piezoelectric actuators (see chapter 1.2.2. ) and a glove box with controllable environment. Temperature (T), relative humidity (Rh), and pressure (P), are monitored using a Rotronic HygoPalm3 with calibrated HygroClip SC05.

The relative humidity can additionally be controlled by adjusting the inflowing gas mixture of dry N<sub>2</sub> and humid air. The humid air is generated by using several stages of bubbler's and droplet filters. This allows one to vary the humidity between approximately 1 %rh and 75 %rh, the latter being the maximum allowed humidity for the AFM according to the manufacturer. The temperature is controlled by the air conditioning of the laboratory (21±2 °C). The pressure in the box is always about 867±5 hPa.

During the measurement, the angle between the cantilever and the x-axis,  $\Theta$ , is kept between 10° to 12°, as indicated in figure 3-1 (b). Voltages between ±25 V<sub>DC</sub> are applied using a HP E3631A power supply (Hewlett Packard, USA) and bonded Al wires. The cantilever is always grounded during the measurements using the same power supply.

Finally, the setup (AFM, Rotronic and power source) is controlled by a home made visual basic program running on a PC.

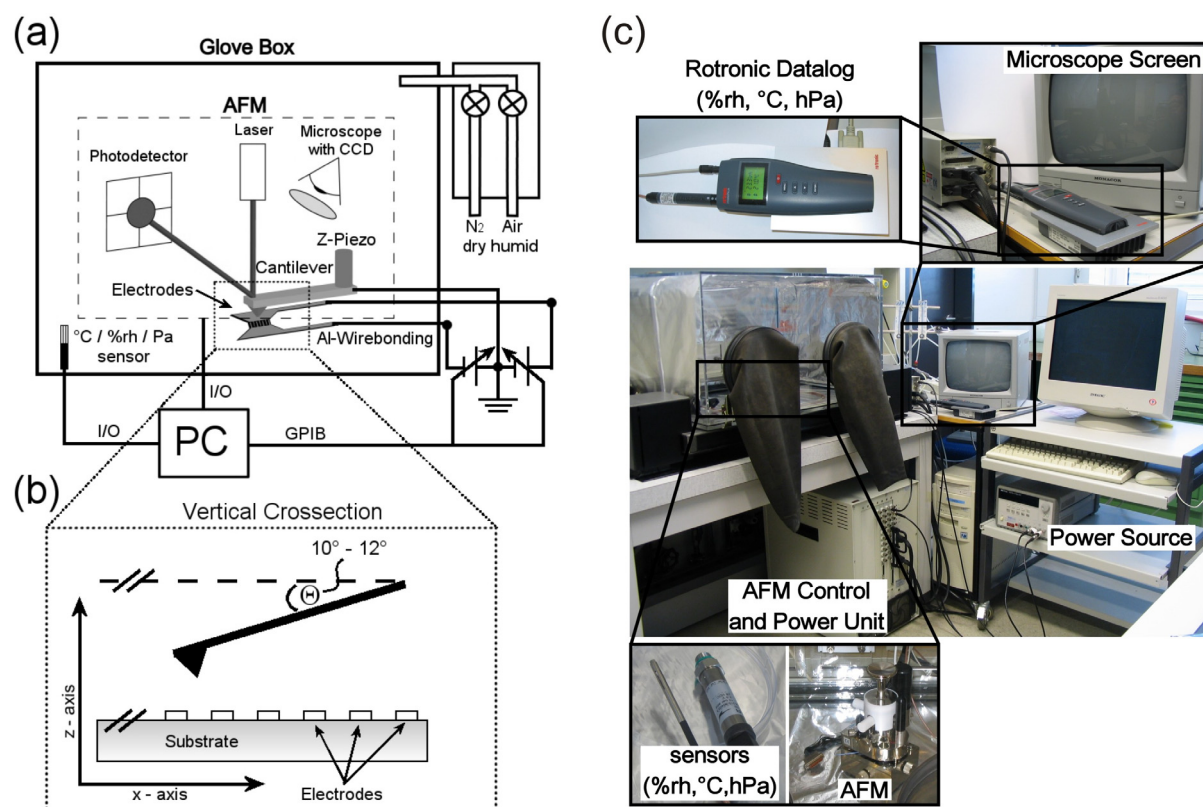


Figure 3-1: Sketches (a)(b) and pictures (c) of the experimental AFM setup. The setup was constructed during this PhD work to allow AFM measurements in a controlled manner under different environmental conditions.

### 3.2) Humidity Measurement and Control

Today, many different methods to measure humidity<sup>1-6</sup> exist. We decided to use a sensor that combines a capacitive method with a highly hygroscopic polymer (Rotronic, HW3, Hygroclip SC05, Switzerland), because it allows fast measurements within 1.5 %rh and 100 %rh with an accuracy of  $\pm 1.5$  %rh and has a low drift. Regular measurements of 10 and 50 %rh commercial calibration standards revealed no drift of the sensor over the whole time of usage. The disadvantage of this sensor is its detection limit of 1.5 %rh due to its accuracy. Therefore, we have to use another humidity sensor to determine

the humidity inside the environmental box after many hours (up to several days) of N<sub>2</sub> flushing.

This sensor does not need to be constantly mounted in our setup, because once we have “calibrated” our setup, we can observe with the HW3 the progression of the humidity down to 1.5 %rh. Afterwards, we wait for the determined time to reach a specific humidity.

We used for this a Xentaur XTR-100 Al<sub>2</sub>O<sub>3</sub> thin film capacitance dew-point sensor. The sensor has a dew-point measurement range of +20 °C to -100 °C with an accuracy of ±3 °C. This corresponds to a measurement range of 0 %rh to 100 %rh with an accuracy of about ±0.0004 %rh for low relative humidities and about ±17 %rh for high relative humidities, due to the exponential relationship between dewpoint and relative humidity<sup>7, 8</sup>:

$$\%rh = 100 * e^{5417.12 * \left\{ \left( \frac{1}{[273.15 + T(^{\circ}C)]} \right) - \left( \frac{1}{[273.15 + DP(^{\circ}C)]} \right) \right\}} \quad \text{Eq. 3-1}$$

where DP(°C) is the dewpoint in °C and T(°C) is the room temperature in °C.

Figure 3-2 shows the changing of the relative humidity with time during the flushing of the environmental box with N<sub>2</sub>, recorded with both humidity sensors at the same time.

For the higher relative humidity the HW3 delivers the more accurate results for the lower relative humidity the accuracy of the Xentaur is higher. Therefore, figure 3-2 can be interpreted as followed: The humidity in the environmental box decreases fast within the first hour from 61 %rh to 2.93 %rh, after 24h the humidity is around 2.71 %rh and decreases slowly until 0.94 %rh after 69 h. Therefore, the environmental box is flushed for at least 24 h prior to all force measurements conducted in N<sub>2</sub> atmosphere. This should results always in 2 to 3 % relative humidity.

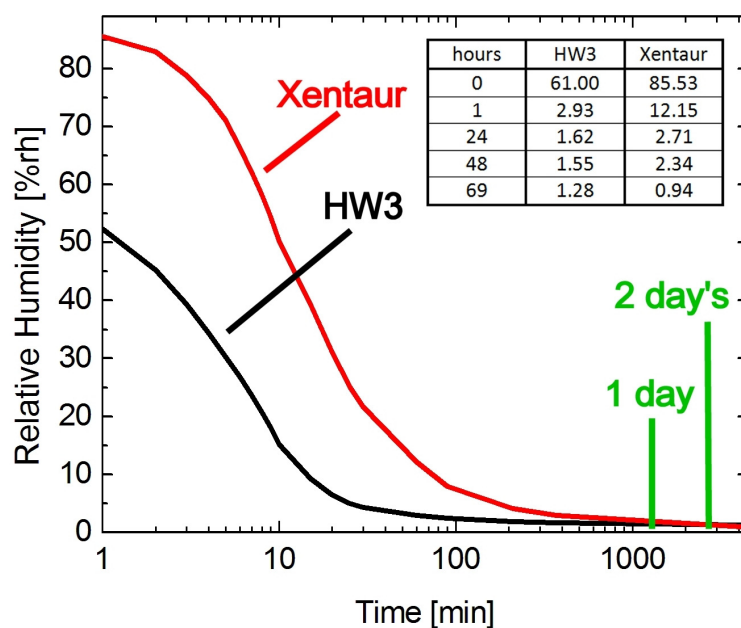


Figure 3-2: Humidity vs time graph for  $N_2$  flushing of the environmental box with 10 lpm. The changing of the humidity is recorded with two humidity sensors. The HW3 has a good accuracy down to 3 %rh, and the Xentaur has a good accuracy below it.

### 3.3) AFM

All AFM measurements within this thesis are performed using a Topometrix (now Veeco) Explorer AFM. A detailed view of the AFM system is shown in figure 3-3. The advantages of this AFM are its high flexibility. Almost all AFM signals can be connected to external instruments, nearly all measurement parameters can be changed and custom routines can be integrated using Visual Basic. This is why, this AFM model is, despite its age (produced 1996), a good choice for developing new AFM modes.

As already mentioned in the chapters 3.1.1 and 1.2.2 the x, y and z-piezo's of the AFM are linearised<sup>9</sup>. As for every AFM, this linearisation has to be checked and recalibrated from time to time. The calibration is done using silicon samples with precisely fabricated Si-structures on top. The structures are usually lines or rectangular blocks with a defined width, length and height.

The calibration samples are scanned using contact mode and the measured dimensions are compared with the reference values. Finally, the linearisation parameters of the AFM are adjusted accordingly.

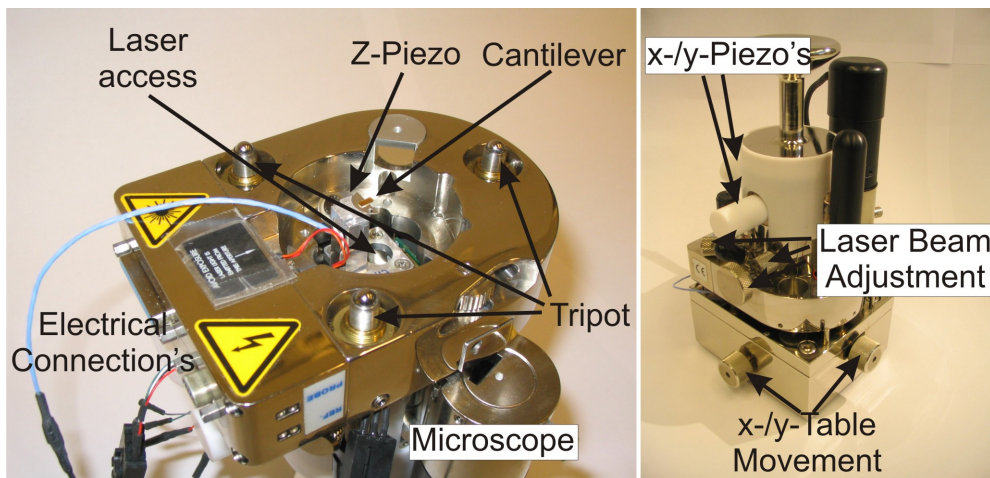


*Figure 3-3: Images of the AFM (Topometrix / Veeco Explorer) used for this thesis. Left: Bottom view of the AFM, with a mounted cantilever. Right: Tilted view of the AFM mounted on a X-Y table. The X-Y table is used to position our samples.*

The calibration procedure is performed several times with different calibrations samples of different dimensions in order to minimize the error within the entire scan range of interest. Table 3-1 shows the resulting errors at different heights after the z-piezo calibration.

Expected height [nm]	Measured height [nm]	Error [%]
19	18.15	4.47
104	107.94	3.79
540	552.34	2.29

*Table 3-1: Z-piezo calibration with different calibration samples. The error between expected and measured height is always below  $\pm 5$  %.*

The piezos have been calibrated regularly during this PhD. In general, the error of the z-piezo is kept below  $\pm 5$  % and the errors for x and y piezos are kept below  $\pm 6$  %.

### 3.4) Bibliography of Chapter 3

1. Rittersma, Z.M., *Recent achievements in miniaturised humidity sensors-- a review of transduction techniques*. Sensors and Actuators A: Physical, 2002. **96**(2-3): p. 196-210.
2. Chachulski, B., G. Jasinski, et al., *Properties of humidity sensors with porous Al<sub>2</sub>O<sub>3</sub> as a dielectric layer*. Proceedings of SPIE - The International Society for Optical Engineering, 2004. **5505**: p. 95-100.
3. Jachowicz, R.S. and S.D. Senturia, *A thin-film capacitance humidity sensor*. Sensors and Actuators, 1981. **2**: p. 171-186.
4. Khanna, V.K. and R.K. Nahar, *Effect of moisture on the dielectric properties of porous alumina films*. Sensors and Actuators, 1984. **5**(3): p. 187-198.
5. Reverter, F. and O. Casas, *Direct interface circuit for capacitive humidity sensors*. Sensors and Actuators, A: Physical, 2008. **143**(2): p. 315-322.
6. Varghese, O.K. and C.A. Grimes, *Metal oxide nanoarchitectures for environmental sensing*. Journal of Nanoscience and Nanotechnology, 2003. **3**(4): p. 277-293.
7. Kuemmel, B. *The Temp, Humidity & Dew Point (Often Needed Answers)*. 1997; <http://www.faqs.org/faqs/meteorology/temp-dewpoint/>.
8. Riegel, C.A. and A.F.C. Bridger, *Fundamentals of Atmospheric Dynamics and Thermodynamics*. 1989: World Scientific Publishing Co Pte Ltd. 340.
9. IPC Systems Ltd. *THE STRAIN GAUGE*. 2008; <http://www.sensorland.com/HowPage002a.html>.

---

## Coating of Cantilevers

Commonly, cantilevers with a metallic tip or coating (Ti/Au) are used for EFM. Cantilevers with dielectrics can be used as well, but the production of these tips is often complicated and the tip-surface interaction of dielectric tips is orders of magnitude weaker in comparison with metals<sup>1</sup>. Metallic tips disturb the electrical field, therefore, the tips have to be taken into account in the final analysis.

We bought Ti / Au coated tips from two producers (Veeco, Novascan) and conducted several EFM tests with these tips. During those tests we began to observe a degradation of the tip quality after only a few measurements. After 100 to 800 force distance curves these tips are broken or deformed, and therefore, no accurate measurements can be performed any more with these tips. In addition, the continuous deformation of the tip has an uncontrollable influence on the measured values, since the tip shape influences the measurements. Therefore, these tips cannot be used for quantitative measurements. Figure 4-1 (a) and (c) shows damaged and deformed tips.

Hence, we decided to coat our own tips. Important features of a tip coating material are its electrical conductivity, hardness at room temperature, adhesion on silicon (Si) (we use Si-cantilevers), diffusion rate in Si, harmlessness (e.g. not radioactive), availability (must be easily available for us), and we must be able to sputter it, because a good coverage is needed. Most metals can be sputtered and all metals are conductive, but some metals oxidise (e.g. Al), are too soft (e.g. Au or Ag) or diffuse in Si (e.g. Cu).

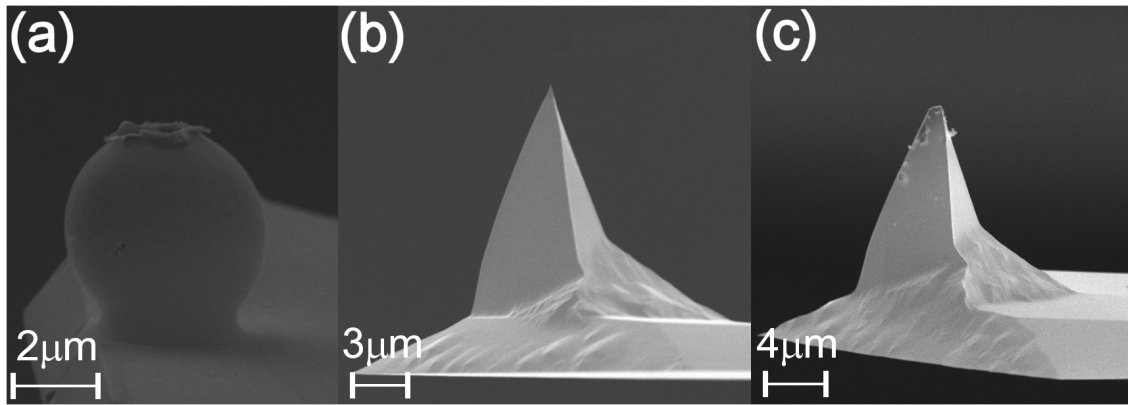


*Figure 4-1: Two commercially available EFM tips. (a) A Gold coated cantilever with sphere, after 100 to 800 FDC. A Ti / Au coated cantilever with tip, (b) before and (c) after several FDC.*

As a result of these considerations we decided to use platinum (Pt) as a coating material. It is available for us as a sputtering target, hard, has low electrical resistivity, does not oxidise and its adhesion to silicon is good.

	Pt	Ta
Density of Solid [kg/m <sup>3</sup> ]	21090	16650
Youngs Modulus [GPa]	168	186
Rigidity Modulus [GPa]	61	69
Bulk Modulus [GPa]	230	200
Mineral Hardness	3.5	6.5
Brinell Hardness [MN/m <sup>2</sup> ]	392	800
Vickers Hardness [MN/m <sup>2</sup> ]	549	873
Electrical Resitivity [mOhm*cm]	10.6	13

*Table 4-1: Material properties of Pt and Ta. Both materials can be used to coat AFM tips, in order to obtain stable EFM tips.*

There exist better coating materials for EFM as Pt, for example Tantalum (Ta), which was not available in the sputtering machine at the beginning of this thesis. By the end of this thesis, Ta became available in the cleanroom and it is possible to use it in future experiments (Table 4-1). However, it is not mandatory to change the material. As long as the chosen material fulfils the above mentioned criteria, it does not matter, which material one uses. The



measured electrostatic force field values will not be affected. This changes if one uses semiconductors with low or no doping. Highly doped semiconductors are considered as metals in EFM<sup>2-4</sup>.

## 4.1) Cantilever with Tips

We performed several sputtering and process flow tests. The sputtering energy was varied between 400 and 1000 Watt. The deposition rate was measured as described in the following: Pt is sputtered for 1 min. on a Si-wafer with kepton tape stripes on top. After removing the tape the sputtered thickness is measured at five different positions on the wafer using an alpha step 500 (TENCOR). After averaging these five values, the sputtering speed is calculated.

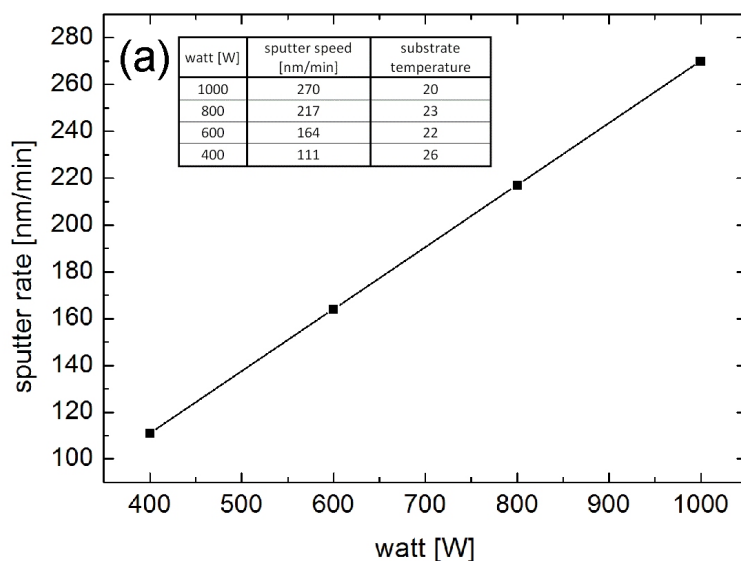


*Figure 4-2: Sputter rate versus sputter energy. Each point is obtained as described in the text. The measured values follow the linear equation:  $\text{sputter rate} = 0.265 * \text{watt} + 5$ .*

Figure 4-2 shows the results of these tests. There is obviously a linear relationship between sputter rate and energy. For the sputtering on the cantilevers a sputter rate of about 110 nm/min. is reasonable. This rate

theoretically enables one to control the sputtered thickness with a precision of about 1.8 nm.

However, we observed that the sputtering rate at 400 Watts changes every day and varies between 120 and 100 nm/min. Therefore, it is necessary to measure the sputter rate each day in order to enable good process control.

The following process flow gave the best reproducible results and was therefore used for the fabrication of several cantilevers:

The cantilevers (Veeco, Model: 1950-00, USA) were cleaned using O<sub>2</sub> plasma. The sputtering speed of the Pt sputtering (26°C; DC; 400W; 432V; 0.9A) (Spider, Pfeifer Vacuum, Switzerland) was measured as described before. Afterwards, the cantilevers were mounted with the tip oriented upwards (cantilever front side up) on a Si-wafer using kepton tape. The wanted thickness of Pt was sputtered using the measured sputtering speed and calculating the sputtering time. After the sputtering was finished the cantilevers are unmounted, and turned, in order to coat the backsides of the cantilevers. The cantilevers were mounted on a special distance holder, mounted on a Si-wafer, to prevent the tip from touching the Si test wafer. The same Pt thickness as on the front was then deposited. The complete setup (Si-wafer with distance holder and mounted cantilever) was placed under an optical microscope, which enables one to measure height differences. The bending of each cantilever, which is caused by the internal stress in the Pt layer, is measured by measuring the height difference between both cantilever ends. Depending on the measured bending additional Pt is sputtered on each cantilever individually until the cantilevers were straight.

Cantilevers with different radii were produced using this procedure. Figure 4-3 shows the obtained tip radius (R) versus sputtered thickness (T) of 14 cantilevers:

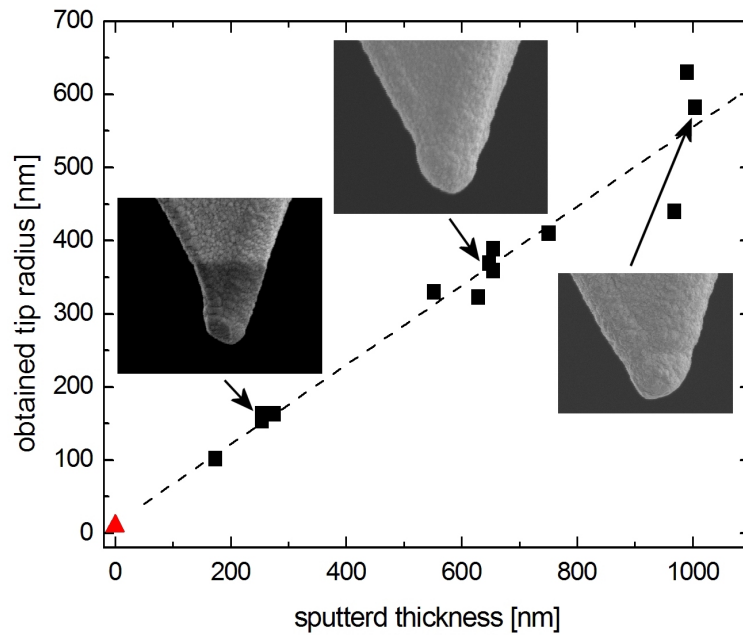


*Figure 4-3: Tip radius vs. sputtered Pt thickness. The red triangle marks the initial nominal tip radius given by the producer. A linear fit that follows equation 4-1 is shown as dashed line. Three SEM pictures of tips with three different radii are shown as well.*

There is an evident linear relationship between the obtained tip radius ( $R$ ) and the sputtered thickness ( $T$ ). The linear fit shown in figure 4-3 (dashed line) follows the equation:

$$R = 0.542 * T + 13 \quad \text{Eq. 4-1}$$

The factor 13 in the equation is close to the nominal tip radius (10 nm) and is likely the real tip radius. The factor 0.542 results probably from different geometrical and physical parameters. The thickness  $T$  of a film obtained by sputter deposition is influenced, by<sup>5, 6</sup>:

- The geometry and temperature of the sputtering chamber.
- The geometry, position and temperature of the sample.
- The sputtering material and its properties.
- The sample material and its properties.

The growth rate of a sputtered film at each point of a sample is determined mainly (if no resputtering occurs) by the “visible” area of the sputter target<sup>7-10</sup>. Therefore, we can approximate roughly the sputtering process on our tip as follows:

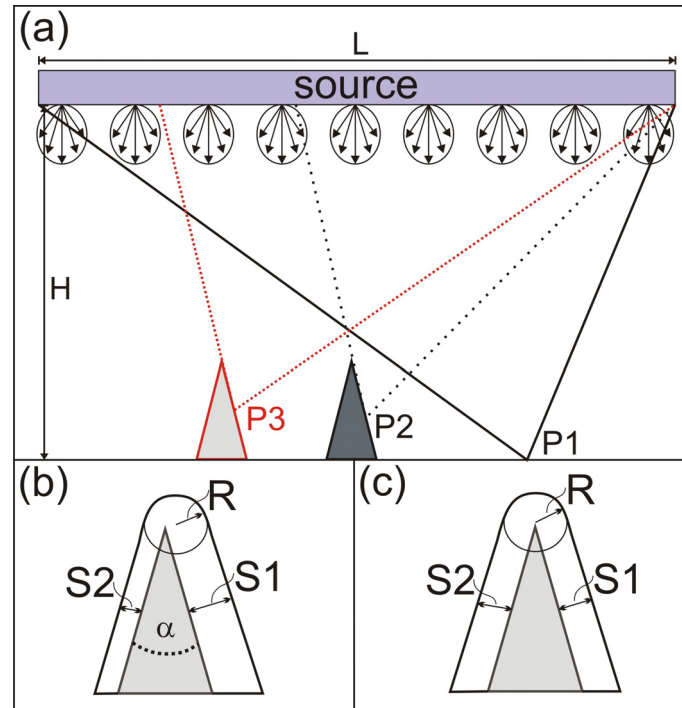


*Figure 4-4: (a) Schematic drawing of a sputter deposition chamber with two tips, source diameter  $L$  and sample to source distance  $H$ . A magnified cross-section through the tip with position  $P2$  and  $P3$  is shown in (c) and (b), respectively. (a), (b) and (c) show that the resulting tip radius depends on the tip and chamber geometry but not on the position of the tip in the chamber.*

Figure 4-4 (a) shows a two dimensional schematic drawing of the sputter deposition chamber with two tips. At the position  $P1$  the sample is flat and  $P1$  is visible from all points of the sputter source (black line). Therefore, every point of the sputter source contributes to the sputtered thickness at point  $P1$ . At point  $P2$  a part of the sputter source is hidden by the tip geometry (black large spaced dotted line). Hence, only a part of the sputter source contributes to the sputtered thickness. The area of the sputter source that contributes to the sputtered thickness of the tip side walls, depends on the

position of the tip (red small spaced dotted line). For example, the thickness at position P3 will be higher as at position P2, because more area of the sputter source can contribute to the film growth.

Figure 4-4 (b and c) presents a cross-section through the two tips illustrated in (a). Figure 4-4 (c) shows the tip in the middle of the sputter chamber (right tip). Both tip side walls have the same sputtered film thickness, because the area of the sputter source that contributes to the film thickness on both tip side walls is the same. The tip radius is equal to the sputtered film thickness at one side. Figure 4-4 (b) shows the tip on the left of (a). The sputtered film thickness on the right wall is higher than on the left wall, because the area of the sputter source that contributes to the film thickness on the left wall is less than on the right wall. However, in total one has sputtered the same thickness onto the tip. Therefore, the radius of the tip will be the same as before for the right tip. This effect can be as well seen in SEM pictures in figure 4-3.

In our case we use a round sputter source with a diameter ( $L$ ) of about 20 cm. The distance between sample and source ( $H$ ) is about 4 cm. The chosen cantilever tips have a nominal apex angle ( $\alpha$ ) of 30°. With this geometric information, we can calculate, using simple triangular equations, how much of the area contributes to the sputtered thickness on one tip wall. In our case this is 11.07 cm. Normalized to the diameter of the sputter source we get a factor of 0.554. This factor is very close to the factor 0.542, which we get from our linear fit. This indicates that the assumptions we made and our model are correct and this factor results mainly from the geometry of the tip and chamber.

Furthermore, figure 4-3 presents the limits of our fabrication method. The distribution of the obtained tip radii for each sputtered thickness increases with the sputtered thickness. The fabrication of tips with a tip radius above 600 nm is therefore not advisable. However, a tip radius of 600 nm equals a tip diameter of 1.2  $\mu\text{m}$ , which is already close to the diameter of the smallest commercial available spheres (2  $\mu\text{m}$ ) glued on cantilevers.

During the FDC measurements (chapter 6) all produced tips did not change

their radius for several thousand's of FDC measurements<sup>11</sup>. Figure 4-5 shows an example of a tip before and after several thousands of FDCs.

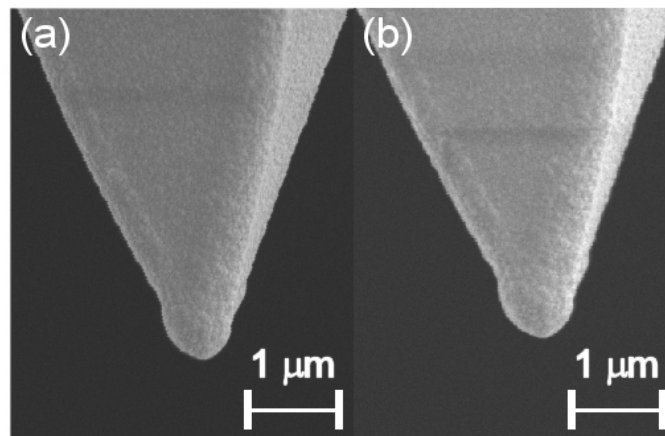


*Figure 4-5: Two SEM pictures of an EFM tip produced as described in the text. (a) shows the tip before and (b) after several thousand's of FDC curves. The tip did not change its shape during the measurements.*

This process is a small but significant step forward for the EFM measurement community, because it offers metallic tips with stable tip shape and adjustable tip radius that can be produced using a simple fabrication process. In addition, the fabricated tips close the gap between conventional tips with small tip radius and cantilevers with glued spheres.

## **4.2) Cantilever with Spheres**

Cantilevers with glued spheres instead of tips are often used for the determination of surface forces (e.g. Van der Waals). The advantages of using spheres instead of tips are: 1.) Since several decades very good analytical equations for the theoretical calculation of the surface energy and other parameters between a sphere and flat surface are available. 2.) Due to a larger interaction surface in comparison with a small tip, the measurement signal is enhanced, resulting in a higher signal to noise ratio.

At the same time the larger interaction surface is as well the main disadvantage of using spheres, because the measured surface forces are an average over the whole interaction surface. However, when big sample surfaces are used, cantilevers with spheres are preferable.

Cantilevers with spheres are usually fabricated by gluing a metallic or dielectric sphere on a cantilever without tip using a micro-manipulator. In our case we bought cantilevers with glued SiO<sub>2</sub> spheres (Novascan, USA) and sputtered about 50 nm Ti and 80 nm Pt using the same sputtering equipment and process as described in chapter 4.1. The Ti layer is deposited to enhance the adhesion between the SiO<sub>2</sub> (sphere) and the Pt layer.

The O<sub>2</sub> plasma cleaning step turned out to be very important for cantilevers with spheres. Due to the gluing of the spheres by eye invisible glue and/or solvent residues remain on the cantilever and sphere. These residues need to be removed with the O<sub>2</sub>-plasma cleaning before sputtering, because they cause topographic irregularities on the coated cantilever surface (figure 4-6 (a)). On the other hand, if the duration of the O<sub>2</sub>-plasma process is too long the sphere detaches from the cantilever. Two test series with six cantilevers were carried out to find the optimal process time. As optimal process time we found 2 min. 30 sec. It enables both, cleaning of the surface, and no detachment of the sphere. Figure 4-6 (b) shows a coated sphere with cantilever after coating and after several measurements.

test	time [min:sec]	watt [W]	remarks
1:1	2:00	50	ok
1:2	4:00	50	some removed
1:3	6:00	50	all removed
2:1	2:00	50	ok
2:2	2:30	50	ok
2:3	3:00	50	one removed

*Table4 2: The oxygen plasma time, plasma RF power and remarks (about sphere detachment) of two test series conducted with six cantilevers with glued sphere. The maximal process time that didn't lead to a detachment of the sphere is 2 min. 30 sec..(0.4 mbar)*

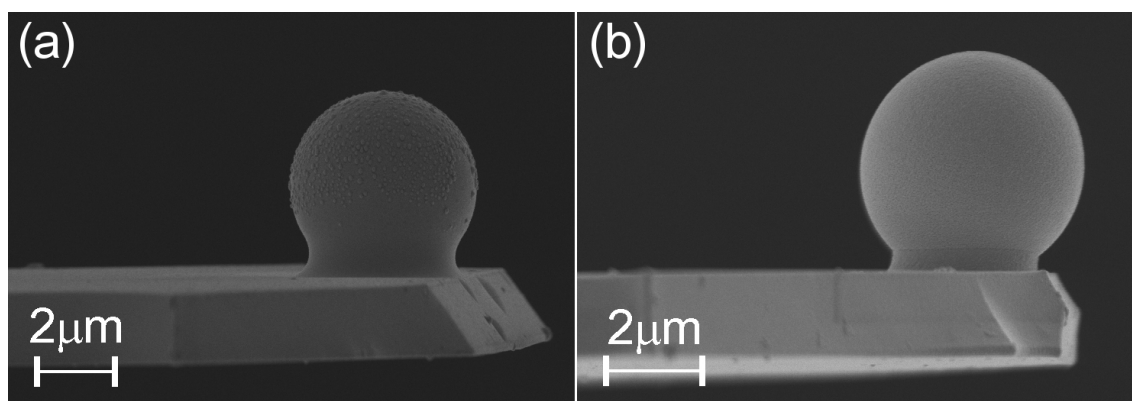


*Figure 4-6: Two cantilevers with spheres after Ti / Pt coating. (a) shows a cantilever without and (b) with proper O<sub>2</sub>-plasma cleaning. In (a) we clearly see dots on the sphere, which result from glue and/or solvent residues.*

### 4.3) Bibliography of Chapter 4

1. Frohe, H., *Elektrische und magnetische Felder*. 1994: Teubner Verlag. 482.
2. Hudlet, S., M.S. Jean, et al., *Electrostatic forces between metallic tip and semiconductor surfaces*. *Journal of Applied Physics*, 1995. **77**(7): p. 3308-3314.
3. Hudlet, S., M. Saint Jean, et al., *Evaluation of the capacitive force between an atomic force microscopy tip and a metallic surface*. *The European Physical Journal B - Condensed Matter and Complex Systems*, 1998. **2**(1): p. 5-10.
4. Kopanski, J.J., J.F. Marchiando, et al., *Scanning capacitance microscopy measurements and modeling: Progress towards dopant profiling of silicon*. *Journal of Vacuum Science & Technology B*, 1996. **14**(1): p. 242-247.
5. Nafarizal, N. and K. Sasaki, *Sticking probability of Ti atoms in magnetron sputtering deposition evaluated from the spatial distribution of Ti atom density*. *Journal of Vacuum Science & Technology A: Vacuum, Surfaces, and Films*, 2007. **25**(2): p. 308-311.
6. Buldum, A., I. Busuladzic, et al., *Multiscale modeling, simulations, and experiments of coating growth on nanofibers. Part I. Sputtering*. *Journal of Applied Physics*, 2005. **98**(4): p. 044303-10.



7. O'Sullivan, P.L., F.H. Baumann, et al. *Numerical Simulations of Sputter Deposition and Etching in Trenches Using the Level Set Technique*. in *Technical Proceedings of the 1999 International Conference on Modeling and Simulation of Microsystems*. 1999: NSTI.
8. Bär, E., J. Lorenz, et al., *Simulation of the influence of via side wall tapering on step coverage of sputter-deposited barrier layers*. *Microelectronic Engineering*, 2002. 64(1-4): p. 321-328.
9. Kwon, O., H. Jung, et al., *Level-Set Modeling of Sputter Deposition*. *Journal of the Korean Physical Society*, 2002. 40(1): p. 72-76.
10. Scheckler, E.W., E.W. Scheckler, et al., *Models and algorithms for three-dimensional topography simulation with SAMPLE-3D*. *Computer-Aided Design of Integrated Circuits and Systems*, IEEE Transactions on, 1994. 13(2): p. 219-230.
11. Jenke, M.G., C. Santschi, et al., *Two-dimensional electrostatic force field measurements with simultaneous topography measurement on embedded interdigitated nanoelectrodes using a force distance curve based method*. *Applied Physics Letters*, 2008. **92**(6): p. 063113-3.



## Cantilever Calibration

Atomic force microscopy and its variants are used in a wide variety of force measurement applications. With AFMs physicists and material scientists measure electrostatic and magnetic fields<sup>1-3</sup>, and structural properties of materials<sup>4,5</sup>. Biologists study molecular binding forces<sup>6-11</sup> and intra-molecular folding forces<sup>12-14</sup>. All these techniques rely on the accurate determination of the cantilever spring constant  $k$  in order to get quantitative results. The cantilever deflection can be measured today with high accuracy. Converting these measurements into force via Hooks law:

$$F = -k \cdot x \quad \text{Eq. 5-1}$$

requires that one determines accurately the spring constant for each cantilever. Even today this is still a challenging task, because the applied methods are very sensitive (to thermal fluctuations, laser deflection changes...), therefore, the obtained  $k$ 's can vary widely.

Numerous methods have been proposed to measure AFM cantilever spring constants: **Dimensional methods** require precise knowledge of the cantilever dimensions and material<sup>15</sup>. **Static experimental methods** employ deflection by calibrated standards<sup>16-21</sup>, glass fibres<sup>22,23</sup> or added masses<sup>24</sup>. **Dynamic experimental methods** detect the shift in resonance frequency caused by an added mass<sup>25</sup>, utilize thermal vibration noise<sup>26-34</sup>, employ knowledge of cantilever mass and resonance frequency<sup>35</sup>, or are derived from fluid dynamics theory<sup>36,37</sup>. Today, dimensional methods are commonly used for a rough approximation of the spring constant ( $k$ ) and resonance frequency ( $f$ ). After these rough approximation dynamical methods are used to determine the exact values for  $k$ ,  $f$  and the quality factor  $Q$ .

The fabrication process discussed in chapter 4 involves the coating of the cantilevers with a thick metal (Pt) film. Not many calibration methods are adapted for cantilevers with thick metal coatings. In the following we will present a few dimensional and dynamical experimental methods for cantilevers with thick metal coatings.

## 5.1) Dimensional Methods

The most used and basic equation for a simple rectangular beam, derived from the Euler-Bernoulli beam theory<sup>38</sup>, is given by:

$$k = \frac{Ewt^3}{4l^3} \quad \text{Eq. 5-2}$$

where  $E$  is the elastic modulus of the cantilever material ( $E_{Si} = 98 \text{ GP}$ ;  $E_{Pt} = 170 \text{ GP}$ ),  $w$  the width of the cantilever,  $t$  its thickness, and  $l$  its length. The resonance frequency  $f$  of a rectangular beam can be calculated using<sup>2</sup>:

$$f = 0.162 \frac{t}{l^2} \sqrt{\frac{E}{\rho}} \quad \text{Eq. 5-3}$$

where  $\rho$  is the density of the cantilever material ( $\rho_{Si} = 2.2 \times 10^3 \text{ kg/m}^3$ ;  $\rho_{Pt} = 21.4 \times 10^3 \text{ kg/m}^3$ ). However, in the present form both equations are not usable for cantilevers with thick metallic coating. Therefore, we have extended the rectangular beam equation 5-2.

Equation 5-2 is deduced from basic mechanical equations. The inertia  $I$  of a rectangular beam cross section can be calculated, with respect to the x-axis (figure 5-2 (a)), using:

$$I = \int y^2 dA = \int_{-t/2}^{t/2} y^2 w dy = \frac{wt^3}{12} \quad \text{Eq. 5-4}$$

The deflection of a beam with a fixed end A and a free end B, with a concentrated load  $F$  on B can be calculated using a second moment-area

theorem. Whereas, the first moment is equal to the deflection  $\delta_B$ , which results in (figure 5-1):

$$\delta_B = \frac{Fl^3}{3EI} \quad \text{Eq. 5-5}$$

Inserting equation 5-4 in 5-5 and using 5-1 (with  $-x = \delta_B$ ) results in equation 5-2.

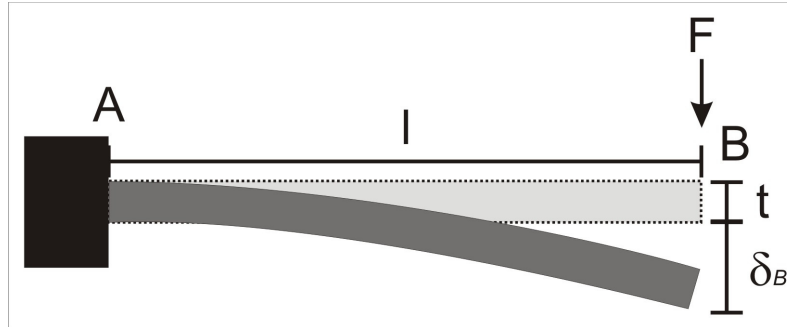


*Figure 5-1: Schematic drawing of the deflection  $\delta_B$  of a beam with a fixed end A, a free end B, an applied concentrated load F at B and the length l.*

If one wants to extend equation 5-2 to a Si-beam with Pt sputtered on both sides of the cantilever, one is confronted with the problem that two materials are used. There exist several methods to extend mechanical models to two or more material models. We have chosen the transformed section method<sup>39</sup>, together with three simplifications:

- 1.) For most cantilevers  $t$  is much smaller than  $w$ , therefore we neglect the cantilever edges.
- 2.) Pt sputtering on the front side of the cantilever causes internal stress in the cantilever. To counter balance for this internal stress the same Pt thickness as on the front of the cantilever is sputtered on the backside of the cantilever (see chapter 4). Therefore, the Pt thickness on each sides of the cantilever can be calculated by subtracting the initial thickness of the cantilever from the thickness after the sputtering and dividing the resulting thickness by two.
- 3.) The Pt thickness is homogeneous over the whole cantilever after the coating. At least, we observed no thickness difference between both ends of

the cantilever after the coating by Secondary Electron Microscopy (SEM). Applying these simplifications, our new cantilever cross section can be schematically drawn as shown in figure 5-2 (b).

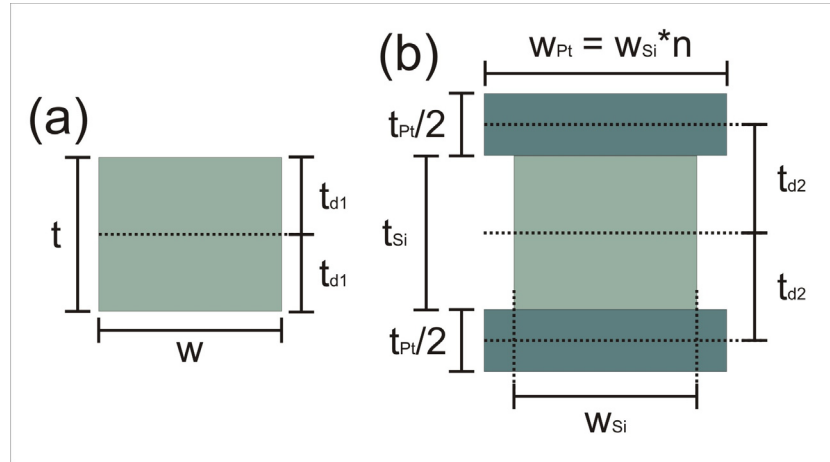


Figure 5-2: Cross section through a cantilever used for (a) equation 5-2 and (b) equation 5-10. ( $t_{d1}$  = distance between neutral axis and top of cantilever;  $t_{d2}$  = distance between neutral axis of Si and neutral axis of Pt). (a) represents a standard Si cantilever and (b) a Si cantilever with a thick Pt coating on both sides.

The neutral axis of the cross section of a composited beam of two materials is obtained by:

$$E_1 \int_1 y dA + E_2 \int_2 y dA = 0 \quad \text{Eq. 5-6}$$

introducing a modular ratio of the form:

$$n = \frac{E_2}{E_1} \quad \text{with } E_2 > E_1 \quad \text{Eq. 5-7}$$

equation 5-6 can then be rewritten to:

$$\int_1 y dA + \int_2 n y dA = 0 \quad \text{Eq. 5-8}$$

This shows that the neutral axis is unchanged if each element of area  $dA$  in material 2 is multiplied by the factor  $n$ , provided that the  $y$  coordinates for

each element stay the same. In other words, we can change the width of both Pt layers by  $n$  and calculate the new inertia using the “parallel axis theorem”<sup>39</sup>. The total inertia of figure 5-2 (b) is then:

$$I = w_{Si} \left\{ n \left( \frac{(t_{Pt})^3}{48} + 2t_{Pt} \left( \frac{t_{Pt}}{2} + \frac{t_{Si}}{2} \right)^2 \right) + \frac{(t_{Si})^3}{12} \right\} \quad \text{Eq. 5-9}$$

Inserting equation 5-9 in 5-5 and using 5-1 (with  $-x = \delta_B$ ) results in the following equation for  $k$ :

$$k = \frac{3E_{Si}w_{Si}}{l^3} \left\{ n \left( \frac{(t_{Pt})^3}{48} + 2t_{Pt} \left( \frac{t_{Pt}}{2} + \frac{t_{Si}}{2} \right)^2 \right) + \frac{(t_{Si})^3}{12} \right\} \quad \text{Eq. 5-10}$$

## 5.2) Dynamic Experimental Methods

Dynamical calibration methods are accurate but as well sensitive methods for cantilever calibration. Due to the fact that most AFM applications use standard Si or silicon nitride (SiN) cantilevers most dynamical calibration methods are only investigated for such cantilevers. The only method which is investigated for cantilevers with thick coating and provides accurate  $k$  values is the method of Sader<sup>35,36</sup>. Therefore, we will concentrate in the following on this method.

The “Sader Method” is one of the three most used and most accurate calibration methods. Other methods are the “Thermal Noise Method”<sup>27</sup> and “Cleveland method”<sup>25</sup>. All three methods are commonly used and well described, but only the thermal noise method is often integrated in AFMs. Therefore, we developed our own calibration setup including software, based on Saders method.

The first step in implementing the Sader method is to record the thermal free vibrations of the cantilever. This signal is captured by positioning the cantilever far away from the sample surface and recording the photodetector voltage

variations as function of time,  $V(t)$ . Fourier transformation is performed on the obtained  $V(t)$  signal to get the detector-voltage spectral power density,  $P_v$ . In our case  $P_v$  is obtained using a 1 GHz digital oscilloscope (LeCroy, LC564A, Switzerland), which is directly connected to the four quadrant photo-diode of the AFM.  $P_v$  can be converted into the deflection spectral power density ( $P_d$ ) by the following relation:

$$P_d = P_v \frac{1}{S^2} \frac{1}{\cos^2 \alpha} \chi^2 \quad \text{Eq. 5-11}$$

where  $\alpha$  is the inclination of the non deflected cantilever with respect to the laser beam. This angle is usually given by the AFM producer and is in our case  $12^\circ$ . Factor  $\chi$  compensates for an  $S$  acquired with an end-loaded cantilever (see next paragraph), whereas  $P_v$  is acquired with the freely oscillating cantilever. According to references<sup>27,32,34</sup>  $\chi$  is 1.09 in our experiments.

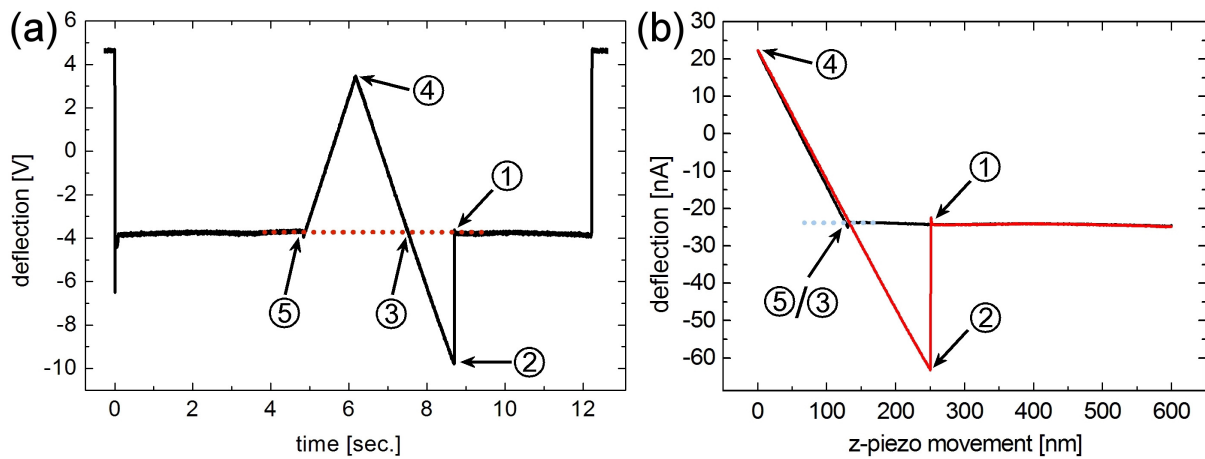


*Figure 5-3: FDC curve obtained with (a) a 1 GHz digital oscilloscope (b) with the AFM. Points 1 to 5 represent respectively: (1) deflection of the free non influenced cantilever; (2) snap out (adhesion force); (3) sample surface point; (4) highest force / reverse of movement; (5) snap in (attraction force).*

The conversion factor or sensitivity  $S$  converts the detector voltage into cantilever deflection.  $S$  is equal to the gradient of the FDCs in figure 5-3 in between points 3 and 4 or 5 and 4. We acquired the same FDC with our 1 GHz digital oscilloscope (figure 5-3 (a)) and AFM (figure 5-3 (b)). From the



obtained  $V(t)$  (figure 5-3 (a)) and deflection [nA] versus distance [nm] (figure 5-3 (b)) graphs, we calculated the sensitivity  $S$  (nA/nm) of this cantilever for both instruments. We calculated a factor  $C$  (0.155951 nV/nA) for converting the  $S$  of the AFM into the  $S$  of the oscilloscope. This will enable us to convert in the future all  $S$  obtained with the AFM to the  $S$  for the oscilloscope without further measurements.

Figure 5-4 shows the  $P_d$  plot of a cantilever at its first resonance peak. The plot is the average of 700 spectra (Sampling rate: 500 kHz; total acquisition time: 100 ms).

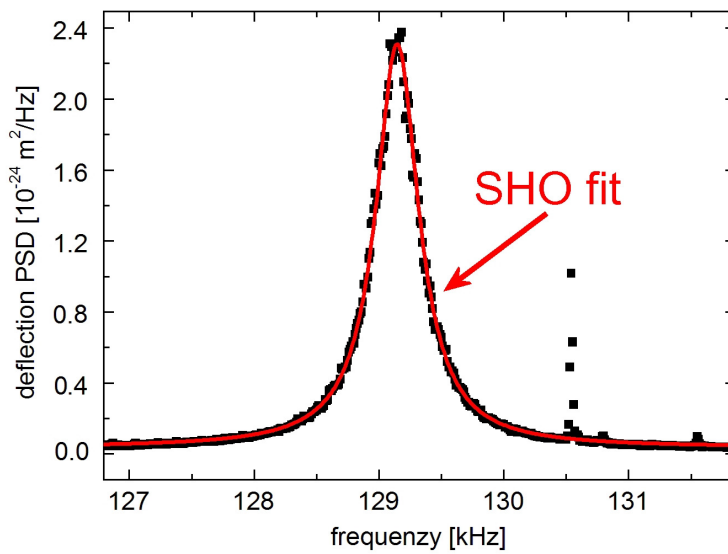


*Figure 5-4: Power spectral density ( $P_d$ ) plot of thermal fluctuations in the output of the cantilever deflection detector. The resonance peak is fitted with a single harmonic oscillator (SHO) model to obtain  $k$ ,  $f$  and  $Q$ .*

In order to extract the resonance frequency ( $\omega$ ) and quality factor ( $Q$ ) the  $P_d$  curve is fitted using a single harmonic oscillator (SHO) model:

$$A = A_{white} + \frac{A_1 \omega_1^4}{(\omega - \omega_1^2) + \left(\frac{\omega \omega_0}{Q}\right)^2} \quad \text{Eq. 5-12}$$

where  $A_{white}$  is a white noise fit baseline<sup>33,37</sup> and  $A_1$  the amplitude of the first resonance frequency. The fitting curve is shown in Figure 5-4. The SHO model fits well the deflection PSD signal.

The Sader method is based on the theory of a driven cantilever response in a fluid of known density and viscosity<sup>33,37</sup>. In air the cantilever response can be calculated using:

$$k = 0.1906 \rho w^2 l \Gamma_i(\omega_R) \omega_R^2 Q \quad \text{Eq. 5-13}$$

where  $l$  is the length,  $w$  the width of the cantilever,  $\rho$  the density of air,  $Q$  the quality factor,  $\omega_R$  the resonance frequency in polar notation and  $\Gamma_i(\omega_R)$  the imaginary part of the hydrodynamic function derived by Sader<sup>35</sup>.

### 5.3) Measurements and Comparison of Methods

We calibrated several cantilevers using the above mentioned methods. The cantilevers were with or without spheres and with or without Pt coating. The cantilevers with sphere were additionally calibrated by the company (Novascan, USA) using the "Cleveland method". Our calibration of these cantilevers is done after a thin Ti/Pt coating as described in chapter 3.2.2. The calibration results using the Sader method together with the values of the company are presented in table 5-1.

The measured  $k$  values differ by 6 to 16 % from those given by the company. The frequencies differ by 2 to 23 %. This is due to the facts that we removed some mass from the cantilevers during  $O_2$  cleaning, added some mass during Ti/Pt deposition and that the Cleveland and Sader method have an error margin of about 30 % and 4 %, respectively<sup>40</sup>. The errors in  $k$  and  $\omega$  are within the expected margin. This shows that our calibration setup works and gives meaningful  $k$  values.

dimensions				company		sader method		
w [ $\mu\text{m}$ ]	l [ $\mu\text{m}$ ]	t [ $\mu\text{m}$ ]	sphere diameter [ $\mu\text{m}$ ]	k [N/m]	$\omega$ [kHz]	k [N/m]	$\omega$ [kHz]	Q factor
36.30	88.29	1.81	4.96	15.74	215.84	14.63	264.43	403.03
35.05	129.00	1.96	4.85	6.65	126.59	5.55	129.01	310.91
37.64	133.20	1.62	4.88	4.44	105.91	3.81	137.64	176.37

*Table 5-1: Geometrical dimensions (determined with SEM),  $k$ ,  $\omega$  and  $Q$  of three calibrated cantilever with sphere and Pt coating.*

We did not use the dimensional methods, which we discussed and further developed in chapter 3.3.2 for the cantilevers with sphere, because the sphere represents a non negligible load to the cantilever. The discussed methods are not applicable for this kind of cantilevers. However, for the following cantilevers with tip they can be used.

Tables 5-2 and 5-3 present the geometrical dimensions measured by SEM and calibration values of several cantilevers with a tip. All cantilever dimensions are measured before and after the coating, abbreviated in the tables by b and a, respectively. This enables us to calculate the theoretical shift of  $k$  and  $\omega$  due to the coating and to compare them to actual measurements. The value for  $\omega$  has to be calculated twice, once with the young modulus and density of silicon and once with the young modulus and density of platinum, because we have no equation for a mixed structure (equation 5-3).

The  $\omega_{\text{sader}}$  measured with the Sader method is within the range of the two calculated  $\omega$  ( $\omega_{\text{Si}}$ ,  $\omega_{\text{Pt}}$ ). The measured  $\omega_{\text{sader}}$  is always between 1 to 4 kHz higher than  $\omega_{\text{Pt}}$ . Hence, we assume  $\omega_{\text{sader}} \cong \omega_{\text{Pt}} + 2 \text{ kHz}$ . The measured  $\omega_{\text{sader}}$  is in fact lower than the original theoretical  $\omega$  before the coating. These results from the high density of Pt which leads to a lower resonance frequency according to equation 5-3.

For 6 out of 8  $k$  values, the developed dimensional model for cantilevers with thick double-side Pt coating ( $k_{\text{mix}}$ ) (equation 5-10), delivers  $k$  values that differ up to 40 % from  $k_{\text{sader}}$ . For 3 out of 8  $k$  values, the conventional Young equation ( $k_{\text{Young}}$ ) (equation 5-2), determines as well  $k$  values within this range. The

measured  $k_{\text{Sader}}$  values of these 3 cantilevers are lower than  $k_{\text{mix}}$ . One possible reason for this is that the Young's modulus of these cantilevers differ from the estimated one. According to Bhushan, B. et al.<sup>41</sup>, the Young's modulus of p-doped (100) silicon varies between 62 and 203 GPa, depending on the measurement methods and doping levels.

To conclude, our developed dimensional model for cantilevers with thick double side coating delivers in most cases better  $k$  values in comparison with the conventional Young equation. The value for  $\omega$  can be approximately calculated by adding 2 kHz to  $\omega_{\text{Pt}}$ . The Sader method delivers accurate values of  $k$ ,  $\omega$  and  $Q$  for cantilevers with thick double side coating.

	w [ $\mu\text{m}$ ]	l [ $\mu\text{m}$ ]	t [ $\mu\text{m}$ ]	tip diameter [nm]	t-Si [ $\mu\text{m}$ ]	(t/2)-Pt [ $\mu\text{m}$ ]	Q factor
1(b)	54.60	471.00	1.49				
1(a)	54.60	471.00	4.01	645	2.75	0.63	242.73
2(b)	48.70	449.70	1.68				
2(a)	48.70	449.70	4.30	777	2.99	0.65	284.20
3(b)	55.80	458.50	1.55				
3(a)	55.80	458.50	4.17	717	2.86	0.65	604.27
4(b)	51.26	448.40	2.46				
4(a)	53.60	454.30	4.44	1260	2.46	0.99	387.48
5(b)	51.06	458.20	2.43				
5(a)	54.30	463.20	4.44	1164	2.43	1.00	590.53
6(b)	50.04	454.20	2.25				
6(a)	51.16	455.20	3.75	819	2.25	0.75	128.01
7(b)	49.35	454.10	2.21				
7(a)	53.47	468.70	3.51	737	2.21	0.65	237.80
8(b)	52.99	455.80	2.56				
8(a)	53.15	458.50	4.50	879	2.56	0.97	112.18

*Table 5-2: Geometrical dimensions (by SEM) and  $Q$  values (by SHO fit) measured (b) before and (a) after Pt sputtering of eight cantilevers with tip.*

	geometry ( $E_{Si} = 98$ Gpa)		geometry ( $E_{Pt} = 170$ Gpa)	geometry ( $E = \text{mix (Si,Pt)}$ )	sader method	
	k [N/m]	$\omega$ [kHz]	$\omega$ [kHz]	k [N/m]	k [N/m]	$\omega$ [kHz]
1(b)	0.26	13.43	5.67			
1(a)	0.82	19.56	8.26	1.24	0.77	11.86
2(b)	0.35	15.99	6.75			
2(a)	1.04	22.99	9.71	1.55	0.79	11.84
3(b)	0.33	14.72	6.22			
3(a)	1.03	21.46	9.06	1.54	1.92	11.99
4(b)	0.20	13.23	5.59			
4(a)	1.22	23.27	9.83	1.98	1.28	12.65
5(b)	0.19	12.53	5.29			
5(a)	1.17	22.39	9.45	1.89	2.88	12.22
6(b)	0.15	11.80	4.98			
6(a)	0.70	19.58	8.27	1.11	0.25	8.92
7(b)	0.14	11.61	4.90			
7(a)	0.55	17.28	7.29	0.81	0.59	10.06
8(b)	0.23	13.36	5.64			
8(a)	1.24	23.18	9.79	1.98	0.32	11.46

Table 5-3: Calculated and measured  $k$  and  $\omega$  of the same cantilevers with tip as in table 5-2.

## 5.4) Bibliography of Chapter 5

1. Butt, H.J., *Electrostatic Interaction in Atomic Force Microscopy*. Biophysical Journal, 1991. **60**(4): p. 777-785.
2. Butt, H.-J., B. Cappella, et al., *Force measurements with the atomic force microscope: Technique, interpretation and applications*. Surface Science Reports, 2005. **59**(1-6): p. 1-152.
3. Gomez-Monivas, S., L.S. Froufe-Perez, et al., *Electrostatic forces between sharp tips and metallic and dielectric samples*. Applied Physics Letters, 2001. **79**(24): p. 4048-4050.
4. Lang, K.M., D.A. Hite, et al., *Conducting atomic force microscopy for nanoscale tunnel barrier characterization*. Review of Scientific Instruments, 2004. **75**(8): p. 2726-2731.
5. Lantz, M.A., S.J. Shea, et al., *Simultaneous force and conduction measurements in atomic force microscopy*. Physical Review B, 1997. **56**(23): p. 15345.
6. Dammer, U., O. Popescu, et al., *Binding strength between cell adhesion proteoglycans measured by atomic force microscopy*. Science, 1995. **267**(5201): p. 1173-1175.

7. Florin, E.L., V.T. Moy, et al., *Adhesion forces between individual ligand-receptor pairs*. Science, 1994. **264**(5157): p. 415-417.
8. Grandbois, M., M. Beyer, et al., *How Strong Is a Covalent Bond?* Science, 1999. **283**(5408): p. 1727-1730.
9. Hinterdorfer, P., W. Baumgartner, et al., *Detection and localization of individual antibody-antigen recognition events by atomic force microscopy*. Proceedings of the National Academy of Sciences, 1996. **93**(8): p. 3477-3481.
10. Lee, G.U., D.A. Kidwell, et al., *Sensing Discrete Streptavidin-Biotin Interactions with Atomic Force Microscopy*. Langmuir, 1994. **10**(2): p. 354-357.
11. Moy, V.T., E.L. Florin, et al., *Intermolecular forces and energies between ligands and receptors*. Science, 1994. **266**(5183): p. 257-259.
12. Lee, G.U., L.A. Chrisey, et al., *Direct measurement of the forces between complementary strands of DNA*. Science, 1994. **266**(5186): p. 771-773.
13. Rief, M., M. Gautel, et al., *Reversible Unfolding of Individual Titin Immunoglobulin Domains by AFM*. Science, 1997. **276**(5315): p. 1109-1112.
14. Rief, M., F. Oesterhelt, et al., *Single Molecule Force Spectroscopy on Polysaccharides by Atomic Force Microscopy*. Science, 1997. **275**(5304): p. 1295-1297.
15. Clifford, C.A. and M.P. Seah, *The determination of atomic force microscope cantilever spring constants via dimensional methods for nanomechanical analysis*. Nanotechnology, 2005. **16**(9): p. 1666-1680.
16. Ruan, J.A. and B. Bhushan, *Atomic-Scale Friction Measurements Using Friction Force Microscopy .1. General-Principles and New Measurement Techniques*. Journal of Tribology-Transactions of the Asme, 1994. **116**(2): p. 378-388.
17. Torii, A., M. Sasaki, et al., *A method for determining the spring constant of cantilevers for atomic force microscopy*. Measurement Science and Technology, 1996. **7**(2): p. 179-184.
18. Tortonese, M. and M. Kirk, *Characterization of application specific probes for SPMs*. Micromachining and Imaging (Proceedings of the Society of Photo-Optical Instrumentation Engineers (SPIE)), 1997. **3009**: p. 53-60.
19. Cumpson, P.J., J. Hedley, et al., *Accurate force measurement in the atomic force microscope: a microfabricated array of reference springs for easy cantilever calibration*. Nanotechnology, 2003. **14**(8): p. 918-924.
20. Gibson, C.T., G.S. Watson, et al., *Determination of the spring constants of probes for force microscopy/spectroscopy*. Nanotechnology, 1996. **7**(3): p. 259-262.

21. Jericho, S.K. and M.H. Jericho, *Device for the determination of spring constants of atomic force microscope cantilevers and micromachined springs*. Review of Scientific Instruments, 2002. **73**(6): p. 2483-2485.
22. Li, Y.Q., N.J. Tao, et al., *Direct measurement of interaction forces between colloidal particles using the scanning force microscope*. Langmuir, 1993. **9**(3): p. 637-641.
23. Rabinovich, Y.I. and R.H. Yoon, *Use of Atomic Force Microscope for the Measurements of Hydrophobic Forces between Silanated Silica Plate and Glass Sphere*. Langmuir, 1994. **10**(6): p. 1903-1909.
24. Senden, T. and W. Ducker, *Experimental Determination of Spring Constants in Atomic Force Microscopy*. Langmuir, 1994. **10**(4): p. 1003-1004.
25. Cleveland, J.P., S. Manne, et al., *A nondestructive method for determining the spring constant of cantilevers for scanning force microscopy*. Review of Scientific Instruments, 1993. **64**(2): p. 403-405.
26. Burnham, N.A., X. Chen, et al., *Comparison of calibration methods for atomic-force microscopy cantilevers*. Nanotechnology, 2003. **14**(1): p. 1-6.
27. Butt, H.J. and M. Jaschke, *Calculation of thermal noise in atomic force microscopy*. Nanotechnology, 1995. **6**(1): p. 1-7.
28. Heim, L.O., M. Kappl, et al., *Tilt of Atomic Force Microscope Cantilevers: Effect on Spring Constant and Adhesion Measurements*. Langmuir, 2004. **20**(7): p. 2760-2764.
29. Hutter, J.L., *Comment on Tilt of Atomic Force Microscope Cantilevers: Effect on Spring Constant and Adhesion Measurements*. Langmuir, 2005. **21**(6): p. 2630-2632.
30. Hutter, J.L. and J. Bechhoefer, *Calibration of atomic-force microscope tips*. Review of Scientific Instruments, 1993. **64**(7): p. 1868-1873.
31. Levy, R. and M. Maaloum, *Measuring the spring constant of atomic force microscope cantilevers: thermal fluctuations and other methods*. Nanotechnology, 2002. **13**(1): p. 33-37.
32. Proksch, R., Sch, et al., *Finite optical spot size and position corrections in thermal spring constant calibration*. Nanotechnology, 2004. **15**(9): p. 1344-1350.
33. Schäffer, T.E., *Calculation of thermal noise in an atomic force microscope with a finite optical spot size*. Nanotechnology, 2005. **16**(6): p. 664-670.
34. Walters, D.A., J.P. Cleveland, et al., *Short cantilevers for atomic force microscopy*. Review of Scientific Instruments, 1996. **67**(10): p. 3583-3590.

35. Sader, J.E., I. Larson, et al., *Method for the calibration of atomic force microscope cantilevers*. Review of Scientific Instruments, 1995. **66**(7): p. 3789-3798.
36. Sader, J.E., J.W.M. Chon, et al., *Calibration of rectangular atomic force microscope cantilevers*. Review of Scientific Instruments, 1999. **70**(10): p. 3967-3969.
37. Sader, J.E., J. Pacifico, et al., *General scaling law for stiffness measurement of small bodies with applications to the atomic force microscope*. Journal of Applied Physics, 2005. **97**(12): p. 124903-7.
38. Young, W.C. and R. Budynas, *Roark's Formulas for Stress and Strain*. 2001.
39. Gere, J.M. and S.P. Timoshenko, *Mechanics of Materials*. 1997, Boston: PWS Publishing Company. 912.
40. Ohler, B., "Practical Advice on the Determination of Cantilver Spring Constants" by Veeco Instruments Inc. 2007. p. 12.
41. Bhushan, B. and L. Xiaodong, *Micromechanical and tribological characterization of doped single-crystal silicon and polysilicon films for microelectromechanical systems devices*. Journal of Materials Research, 1997. **12**(1): p. 54.



---

## New EFM Method

### 6.1) Introduction

We presented in chapter 1.2.4. different methods for the measurement of electrostatic force fields. Some of them use two passes and dynamic techniques, others one pass and static techniques. Each of these techniques has its advantages and disadvantages. Some methods (like LI) provide inaccurate force measurements but are easily implemented, other very advanced methods like PFM provide high precision force and topography measurements, but need extensive and expensive hardware and software changes.

We will present in this chapter in detail a new static force distance curve (FDC) based method that can be easily implemented in existing AFM systems. The method allows high precision measurements of the electrostatic force field in three dimensions, the surface topography and the attraction and adhesion force, simultaneously.

Static FDCs are already roughly described in chapter 1.2.4. and 3.3.2. In the following we describe in detail how static FDCs are influenced by electric fields. We describe as well a treatment of the recorded static FDCs, which enables one to distinguish between tip-electric field and tip-surface interactions.

## 6.2) Static FDC Basics / Balance of Forces

Many different interaction forces between cantilever tip and sample contribute to the total force variation with the tip to sample distance in a FDC (figure 5-3 (b)), namely Van der Waals, contact, capillary and electrostatic forces<sup>1</sup>. Varying the relative distance between a cantilever (represented by the plate and spring in figure 6-1) and a sample surface changes the vertical position ( $d$ ) of the tip and the acting tip-sample interaction forces.

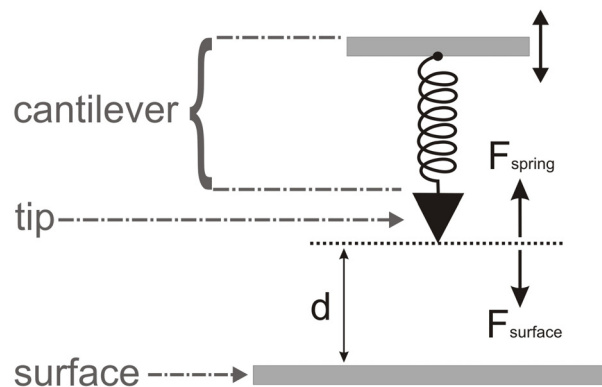


*Figure 6-1: Simple model for the cantilever – sample system.*

The balance between the acting surface forces and the spring force of the cantilever determines the elongation of the spring (or the deflection of the cantilever). In other words, the tip position depends on the acting surface forces and vice versa. The acting surface forces and the spring force of the cantilever are at every distance in equilibrium. Typically, the surface forces increase non-linearly with the distance from the sample. Therefore, the elongation of the spring is non-linear as well, with distance. For example the Van der Waals force between a sphere and a flat surface, and a cone and flat surface can be approximated using Equation 6-1. The latter is used often for the approximation of the Van der Waals force between an AFM tip and a flat surface.

$$F_{sphere-flat} = \frac{HR}{6d}; \quad F_{cone-flat} = \frac{H \tan^2 \Theta}{6d} \quad \text{Eq. 6-1}$$

where H is the Van der Waals constant, d the sphere-/cone-flat surface distance, R the radius of the sphere and  $\Theta$  the tip angle of the cone.

A special situation occurs when the tip is very close to the surface. There the tip-sample interaction force increases strongly. Due to this increase no equilibrium between the acting surface forces and the spring force of the cantilever can be reached. Hence, the elongation of the spring continuous until the tip touches the surface. This position is called the snap-in point in the FDC (figure 5-3). The distance at which this snap-in occurs depends on the tip and sample properties (e.g. surface energy, k...), and the environmental conditions. For example, in humid air the snap-in occurs earlier, because tip and sample are covered with a water film. When these water films touch each other, they form a liquid bridge between tip and sample. In this case strong capillary forces attract the tip and drag it to the surface until they touch. Moving the cantilever away from the surface one has to overcome the acting contact forces between the tip and sample surface. This happens when the spring force is equal to the adhesion force. At this point the tip jumps out of contact. In the FDC this position is called the snap-out point (figure 5-3).

### 6.3) Static FDCs in Electric Fields

As explained earlier, electrostatic fields (e.g. the one above interdigitated electrodes) contribute to the total acting interaction force between tip and surface, which varies with the tip to sample distance in a FDC. An electrical field for example attracts already the cantilever tip at a distance far away from the surface (Figure 6-2). Many other forces (e.g. Van der Waals) attract the cantilever tip only at a much shorter distance from the surface. Therefore, many EFM methods neglect the contribution of the short range forces. This

assumption is correct as long as we have no other long range forces, like other electrostatic forces generated by charge injection into oxides, caused by strong electric fields. In nanoelectronic applications these strong electric fields are often reached due to the small distances. To exclude as well these kinds of surface forces we developed a differential measurement procedure. We take, at every measurement point along a line or in an area, two successive FDCs, one with and one without applied potentials on the underlying structures (in our case interdigitated electrodes). The FDC performed with applied potentials on the interdigitated electrodes result of a sum of several interaction forces including the electrostatic force between the tip and sample due to the underlying structures. The FDC without applied potentials result of about the same sum, differing only in the electrostatic force between the tip and sample due to the underlying structures. This double-FDC method has the additional advantage that it cancels out systematic errors, such as signal variations from laser beam interferences and therefore increases the signal-to-noise ratio (see figure 9-3). Afterwards, each individual FDC is corrected using developed voluminous data treatment algorithms that are based on suggestions of Cappella<sup>2</sup> and Butt<sup>3</sup>. In brief, the data treatment consists of:

- (1) Separation of the approach and retraction parts.
- (2) Multiplication of vertical deflection with  $k$  and  $S$  (see chapter 5) provides the acting force in nN.
- (3) Automatic surface point and snap-in /-out point recognition.
- (4) Real tip – sample height and offset corrections.
- (5) Subtraction of the two treated FDCs to obtain the electrostatic force field.

Automatic FDC recognition and data treatment is not easy and often unstable due to random fluctuations (see figure 9-3), especially point 3 is difficult to achieve. Due to the iterative algorithm we use, the recognition yield of our program is very high. If the shape of the obtained FDC is close to

the “standard” shape of a FDC, which means at least the points 1,2 and 4 in figure 5-4 are present, a recognition yield close to 100% can be obtained. The complete program is attached in the appendix.

Figure 6-2 shows how the measured FDC attraction parts evolve with each data treatment step: (a) the measured FDC attraction parts after step 2, (b) after offset corrections, (c) after step 4 and (d) after step 5.

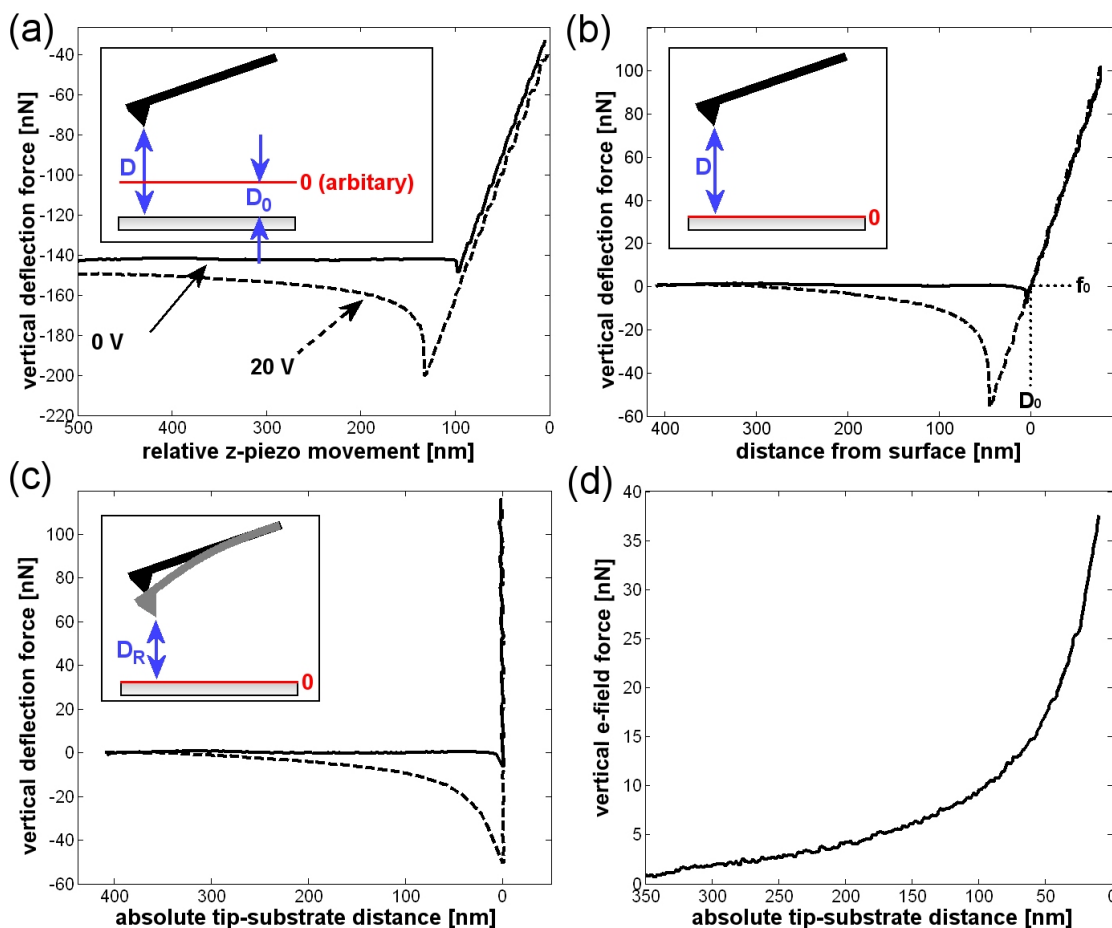
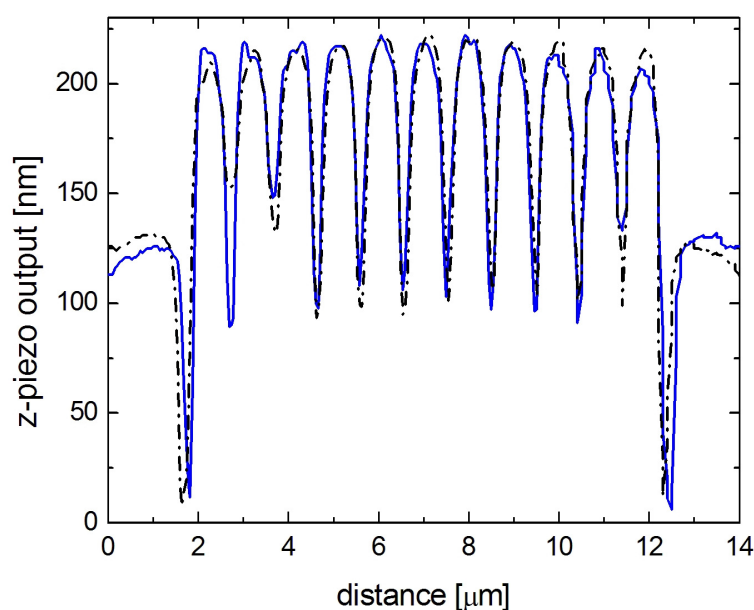


Figure 6-2: (a) The two measured FDCs. (b) Both FDCs after surface point recognition and offset correction. (c) The FDCs after real tip sample height correction. (d) The resulting measured vertical electrostatic force as function of the distance.

## 6.4) Topography

To obtain simultaneously the surface topography and the electrostatic force, we added a step between the consecutive FDC measurements. There the

cantilever tip is in contact with the sample surface and we are able to adjust the voltage on the z-piezo such that the cantilever applies always the same force on the sample. The z-piezo voltage, necessary to obtain this force(/deflection), changes with the position of the cantilever tip on the surface and reflects therefore the topography of the sample. The topography variation can now be obtained from the applied z-piezo voltage changes by multiplication with  $S$  (in nm/nV). This combination allows obtaining simultaneously the surface topography as well as the electrostatic force at any given point.



*Figure 6-3: Comparison between a standard AFM contact scan (black dash-dotted line) and a contact scan performed as described in the text (blue line) made with the same cantilever on the same 500 nm pitch electrodes at approximately the same position and nearly the same orientation between cantilever and electrodes.*

Figure 6-3 shows a comparison of the obtained contact scan and a normal AFM contact scan at about the same position. The scans are very similar. This proves that we get with our method the same results as with a normal contact AFM scan.

## 6.5) Vertical Electrostatic Force Field

The methods introduced above, are used to determine the vertical electrostatic field above 500 nm pitch electrodes with high resolution<sup>4,5</sup>. The scan is carried out perpendicular to the electrode orientation in a glove box with the following controlled environmental conditions:  $21 \pm 1$  °C;  $60 \pm 5$  %rh;  $867 \pm 5$  hPa. The 500 nm pitch interdigitated Ti nanoelectrodes were fabricated on quartz substrates as explained in chapter 2.2 and covered with 30 nm of SiO<sub>2</sub>.

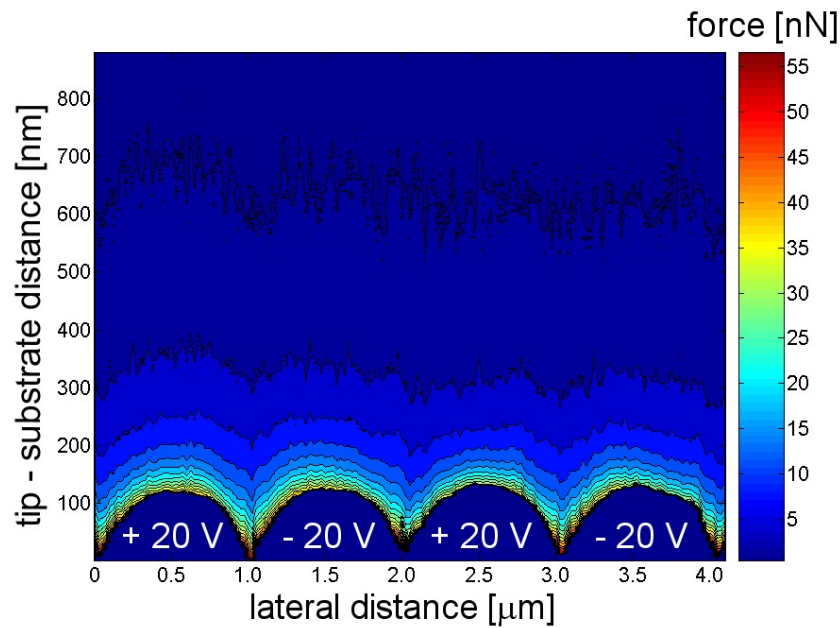


*Figure 6-4: Measured force field and topography of 500 nm pitch electrodes with  $\pm 20$  V applied, alternately. A cantilever with a tip of 380 nm in radius and a spring constant of 0.79 N/m is used to perform the measurements.*

The Si cantilever with Pt coating utilized for the measurement had a tip radius of approximately 380 nm, a spring constant of  $k = 0.79$  N/m, a quality factor of  $Q = 284$ , a resonant frequency of  $\omega_R = 1.844$  kHz and a conversion factor of  $S = 0.12$  nA/nm. All values are determined as described in chapter 5. During the measurement, the angle between the cantilever and the y-axis,  $\theta$ , is kept between  $10^\circ$  and  $12^\circ$ , as shown in figure 3-1 (a). Voltages of -20 VDC and

+20 VDC are applied to the interdigitated nanoelectrodes via bonded Al wires. The cantilever is grounded during the measurement.

In the vertical plane perpendicular to the orientation of the nanoelectrode array, an area of  $4.5\ \mu\text{m}$  in width and 450 nm in height was scanned by the cantilever with a lateral sampling rate of 25 nm and a vertical sampling rate of 2 nm. Figure 6-4 shows the obtained force field distribution above the arrays of interdigitated nanoelectrodes with topography. The shape of the topography shown in figure 6-4 is a convolution of the real topography (500 nm pitch electrodes) and the shape of the AFM tip<sup>6</sup>. It can be seen from the same figure that each equi-force line below  $z = 150\ \text{nm}$  reaches its local height minima at an  $x$  position right in between two adjacent electrodes. There the tip passes its lowest point above the surface and is subjected to strongest attraction by the two nearest electrodes. The electrostatic force decreases rapidly with increasing distance from the electrode surface. At a distance of 800 nm from the surface, the electrostatic force becomes too small to be detected ( $< 1\ \text{nN}$ ).

## 6.6) Bibliography of Chapter 6

1. Israelachvili, J., *Intermolecular & Surface Forces*. Vol. 2. 1992.
2. Cappella, B. and G. Dietler, *Force-distance curves by atomic force microscopy*. Surface Science Reports, 1999. 34(1-3): p. 1-+.
3. Butt, H.-J., B. Cappella, et al., *Force measurements with the atomic force microscope: Technique, interpretation and applications*. Surface Science Reports, 2005. 59(1-6): p. 1-152.
4. Jenke, M.G., C. Santschi, et al., *Two-dimensional electrostatic force field measurements with simultaneous topography measurement on embedded interdigitated nanoelectrodes using a force distance curve based method*. Applied Physics Letters, 2008. 92(6): p. 063113-3.
5. Jenke, M.G., C. Santschi, et al., *Characterization of Electrical Fields of Buried Interdigitated Nanoscale Ti-Electrode Arrays by a Novel Atomic Force Microscopy Measurement Procedure and Their Fabrication by FIB Milling*. NSTI-Nanotech2007, 2007. 4: p. 97-100.
6. Bhushan, B., *Scanning Probe Microscopy, in Handbook of Nanotechnology*. 2004, Springer: Berlin Heidelberg. p. 374.



## Numerical Simulation of the new Method

### 7.1) Introduction

The theory of tip-sample interactions has been extensively discussed in the literature<sup>1,2</sup>. Beside Van der Waals forces<sup>1-4</sup>, electrostatic interaction forces are the most discussed surface forces<sup>5-7</sup>. However, many of the theoretical publications focus on a conductive tip / cantilever over an unlimited expanding plane<sup>3,8-14</sup>. Only few publications discuss interactions of conductive tips with structured samples<sup>15-17</sup>. Several analytical models exist for the unlimited expanding plane case but only a few for the tips with structured samples case, which are limited to specific geometries. These models try to reduce the complexity of the geometry by making several assumptions (e.g. sharp knife instead of tip) and using 2D models as done by Böhm et al.<sup>15</sup>. They obtained a electrical force  $F$  per effective area  $A$ , which is expressed as follows:

$$\left| \frac{F}{A} \right| \mathbf{e}_y = \frac{4(U_s U_P)^2 \epsilon_0}{\pi} \frac{1}{x^2 + h^2} \mathbf{e}_y \quad \text{Eq. 7-1}$$

where,  $h$  is the tip-sample distance,  $U_P$  the applied voltage on the sample,  $U_s$  the applied voltage on the tip,  $\epsilon_0$  the dielectric constant and  $x$  the position of the tip. This model delivers a very rough estimation for the force of a metallic tip over interdigitated electrodes. Gómez-Moñivas et al.<sup>16</sup> developed a model, which delivers a more accurate estimation for the force of a metallic tip over interdigitated electrodes. The model uses analytical equations in connection with numerical methods. The sample and tip geometry is given in a 3D model together with the boundary conditions. With the analytical

equations one calculates the force between tip and sample for all distances and positions on the 3D surface model.

## **7.2) Our Numerical Model**

Based on the mentioned difficulties to develop good analytical “tips with structured samples” models we decided to develop a numerical model of our measurement method. With this model one can compare the measurements with theoretical calculations and study more in detail the developed EFM method, and EFM in general.

The model is developed in three major steps:

### **A.) Identification and Reduction**

To save calculation time we reduced the model to the absolutely necessary geometries, physical parameters and movements. In detail, for pitches below 1  $\mu\text{m}$  we include in our model only a part of the tip (up to a height of 6  $\mu\text{m}$ ) and only the number of electrodes that are necessary (figure 7-1 (a)). Cantilever and other geometry influences can be neglected because the range of the electric field for pitches below 1  $\mu\text{m}$  is in the order of a few 100 nm (figure 7-1 (b)). Assuming the tip moves slowly enough during the measurement to fulfil the condition:  $F_{\text{Spring}} = F_{\text{surface}}$  at all points before the snap-in and after the snap-out. One can replace the constant movement of the tip by a sequential movement and use static conditions for the calculation of the force on the cantilever at each tip position. At each of these tip positions the full 3D electrical field has to be calculated, which can be extremely time intensive. To reduce the calculation time the movement of the tip is often limited to a vertical plane perpendicular to the orientation of the nanoelectrodes array (chapter 6).

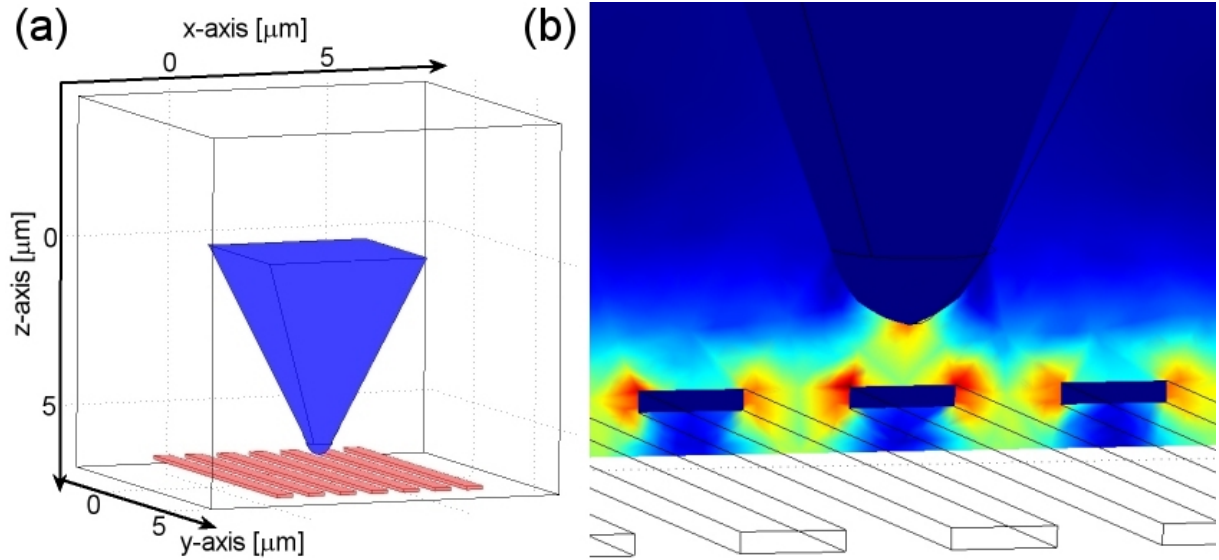


Figure 7-1: (a) Simulated geometry. (b) Norm E-field at the position of the tip, calculated with the geometry shown in (a). One can see that the E-field doesn't exceed the first few 100 nm.

## B.) Physical background

The coulomb force on a point charge ( $Q_p$ ) in an electrical field ( $E$ ) is given by electrostatic field physics<sup>18</sup>:

$$\vec{F} = Q_p \vec{E} \quad \text{Eq. 7-2}$$

This equation can be only used for point charges or a discrete number of charges. For charges with a spatial extension, one needs to calculate a force density ( $f$ ) using:

$$\vec{f} = \frac{d\vec{F}}{dV} = \rho \vec{E} \quad \text{Eq. 7-3}$$

where  $\rho$  is the spatial charge density. This spatial charge density can be located in free space (not attached to a body), on a deformable or non-deformable body. In the later case, it is possible to calculate the total force ( $F$ ) on this body by integration over the total volume of the body:

$$\vec{F} = \int_V \vec{f} dV = \int_V \rho \vec{E} dV \quad \text{Eq. 7-4}$$

For the special case of a metallic body the spatial charge density can be replaced by the surface charge density  $\sigma$ , which is localized at the surface of the metallic body. To obtain the surface charge density  $\sigma$  one has to integrate the spatial charge density over the thickness  $\delta$  (figure 7-2) at every point of the surface of the metallic body:

$$\sigma_{(x,y)} = \int_{\delta} \rho_{(x,y,\delta)} d\delta \quad \text{Eq. 7-5}$$

The E-field varies with the charge density over the total thickness  $\delta$  of the first atomic layers of the metallic body. Using equations 7-4 and 7-5, one can derive an equation for the total force per area of the metallic body caused by the electric field and surface charge:

$$\frac{d\vec{F}}{dA} = \int_{\delta} \sigma \vec{E} d\delta \quad \text{Eq. 7-6}$$

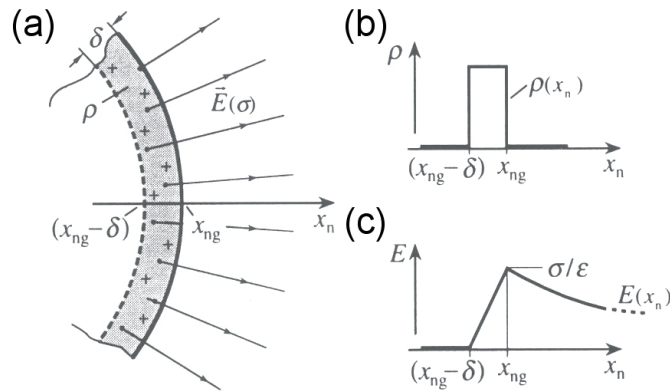


Figure 7-2: (a), (b) and (c) show the development of the spatial charge density  $\rho$  and electric field  $E$  on the surface of a metallic body.<sup>18</sup>

Independent of the progression of  $\sigma$  and  $E$  along  $\delta$ , the integral always results in:

$$\frac{d\vec{F}}{dA} = \frac{\sigma\vec{E}}{2} \quad \text{Eq. 7-7}$$

where  $E$  is always parallel to the surface normal. Using equation 7-7 we can calculate the total electrostatic force on a metallic body by

$$\vec{F} = \int_A \frac{\sigma\vec{E}}{2} dA \quad \text{Eq. 7-8}$$

### C.) Programming

3D numerical calculations are very time consuming, therefore professional numerical solvers are needed in order to carry out the simulations within a reasonable time frame using a commercial PC. We have chosen to use the commercial simulation software Comsol together with Matlab and Solid Works. This enables designing the AFM tips as accurately as possible, importing the model in a powerful numerical solver, and to carry out post data treatment routines for calculating the total electrostatic force on the tip. For the latter, one has to take into account the before performed numerical calculations of the simulation software. In our case equation 7-8 can be reduced and rewritten to:

$$F_{X,Y,Z} = \int_A (\sigma E_{X,Y,Z}) d\vec{A} \quad \text{Eq. 7-9}$$

where,  $X,Y,Z$  represents the integration in  $X$ ,  $Y$  and  $Z$  direction over all tip boundaries.

As already mentioned, in order to simulate our new measurement method we have to move the tip in our model in discrete steps and calculate at each position the  $E$ -field and the total force on the tip. This can be expressed by extending Equation 7-9 to:

$$\left( F_{X,Y,Z} \right)_{x,y,z} = \left( \int_A \left( \sigma E_{X,Y,Z} \right) d\vec{A} \right)_{x,y,z} \quad \text{Eq. 7-10}$$

were the Z is the vertical compound of the force field, which corresponds to the deflection of the cantilever<sup>19</sup>, and x, y,z is the position of the tip. (The complete Matlab code is shown in the appendix.)

Performing the numerical calculation with the same geometries as used for the measurement in chapter 6 results in the vertical force field shown in figure 7-3 (b).

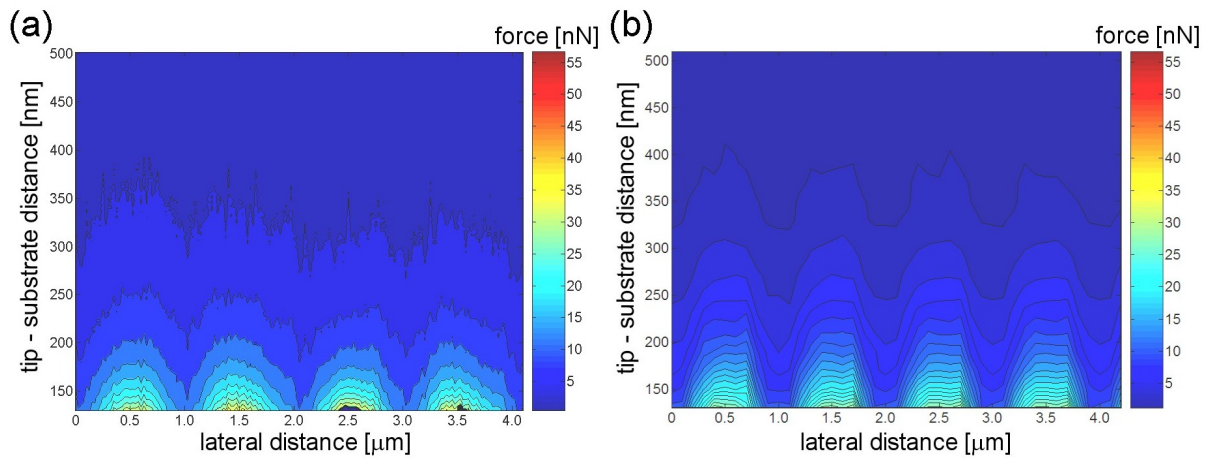


*Figure 7-3: Vertical force field of interdigitated electrodes with 500 nm pitch. (a) shows the measured and (b) the simulated force field.*

Figure 7-4 shows a detailed comparison of the simulated vertical force field (figure 7-3 (b)) with the measured vertical force field (figure 7-3 (a)). The electrostatic force between the nanoelectrode arrays and the cantilever tip is plotted as function of the vertical distance at two places on the surface, one on top of an electrode and one between two interdigitated electrodes, corresponding to the x positions 0.5 μm and 1 μm in figure 7-3 (a) and (b), respectively. The calculated values fit well with the measured ones. Only differences in the shape of the curve are observed. These force differences result probably from slight tip shape differences between simulation and experiment. These slight tip shape differences cannot be fully included in the 3D model, but influence the force curve. However, in our case the force

discrepancies are very small (1 to 2 nN) and we can therefore conclude that the simulation confirms the eligibility of our vertical electrostatic force field measurements. The influence of tip shape discrepancies will be discussed in more detail in chapter 8.1.

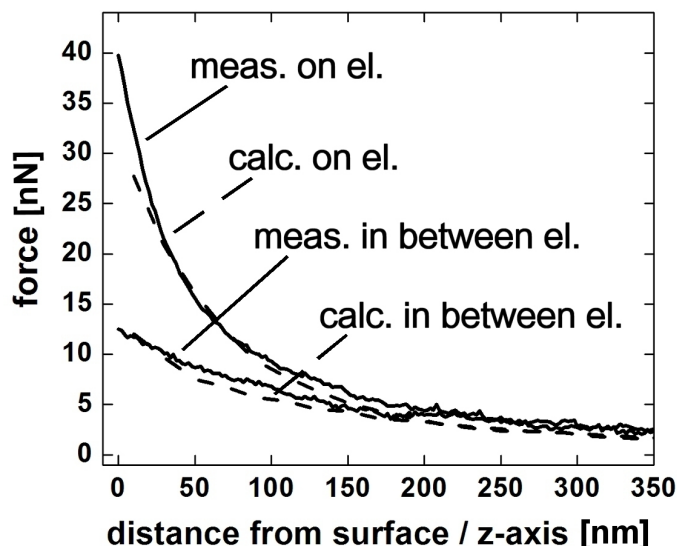


Figure 7-4: Direct comparison of measured (meas.) and simulated (calc.) vertical force field. Obtained on the electrodes (on el.) and in between two electrodes (in between el.).

### 7.3) Bibliography of Chapter 7

1. Butt, H.-J., B. Cappella, et al., *Force measurements with the atomic force microscope: Technique, interpretation and applications*. Surface Science Reports, 2005. **59**(1-6): p. 1-152.
2. Cappella, B. and G. Dietler, *Force-distance curves by atomic force microscopy*. Surface Science Reports, 1999. **34**(1-3): p. 1-+.
3. Jean, M.S., S. Hudlet, et al., *Van der Waals and capacitive forces in atomic force microscopies*. Journal of Applied Physics, 1999. **86**(9): p. 5245-5248.
4. Ohnesorge, F. and G. Binnig, *True Atomic Resolution by Atomic Force Microscopy Through Repulsive and Attractive Forces*. Science, 1993. **260**(5113): p. 1451-1456.
5. Butt, H.J., *Electrostatic Interaction in Atomic Force Microscopy*. Biophysical Journal, 1991. **60**(4): p. 777-785.

6. Enikov, E.T., L.L. Minkov, et al., *Microassembly experiments with transparent electrostatic gripper under optical and vision-based control*. Ieee Transactions on Industrial Electronics, 2005. **52**(4): p. 1005-1012.
7. Jacobs, H.O. and A. Stemmer, *Measuring and modifying the electric surface potential distribution on a nanometre scale: A powerful tool in science and technology*. Surface and Interface Analysis, 1999. **27**(5-6): p. 361-367.
8. Belaidi, S., P. Girard, et al., *Electrostatic forces acting on the tip in atomic force microscopy: Modelization and comparison with analytic expressions*. Journal of Applied Physics, 1997. **81**(3): p. 1023-1030.
9. Colchero, J., A. Gil, et al., *Resolution enhancement and improved data interpretation in electrostatic force microscopy*. Physical Review B, 2001. **64**(24): p. 245403.
10. Gomez-Monivas, S., L.S. Froufe-Perez, et al., *Electrostatic forces between sharp tips and metallic and dielectric samples*. Applied Physics Letters, 2001. **79**(24): p. 4048-4050.
11. Hao, H.W., A.M. Baro, et al. *Electrostatic and contact forces in force microscopy*. in *Proceedings of the Fifth International Conference on Scanning Tunneling Microscopy/Spectroscopy*. 1991. Baltimore, Massachusetts (USA): AVS.
12. Hudlet, S., M. Saint Jean, et al., *Evaluation of the capacitive force between an atomic force microscopy tip and a metallic surface*. The European Physical Journal B - Condensed Matter and Complex Systems, 1998. **2**(1): p. 5-10.
13. Sacha, G.M. and J.J. Saenz, *Cantilever effects on electrostatic force gradient microscopy*. Applied Physics Letters, 2004. **85**(13): p. 2610-2612.
14. Sacha, G.M., A. Verdaguer, et al., *Effective tip radius in electrostatic force microscopy*. Applied Physics Letters, 2005. **86**(12): p. 123101-3.
15. Bohm, C., C. Roths, et al., *Electrical characterization of integrated circuits by scanning force microscopy*. Materials Science and Engineering B, 1994. **24**(1-3): p. 218-222.
16. Gomez-Monivas, S., L.S. Froufe, et al., *Tip-shape effects on electrostatic force microscopy resolution*. Nanotechnology, 2001. **12**(4): p. 496-499.
17. Gomez-Monivas, S., J.J. Saenz, et al., *Theory of electrostatic probe microscopy: A simple perturbative approach*. Applied Physics Letters, 2000. **76**(20): p. 2955-2957.
18. Frohne, H., *Elektrische und magnetische Felder*. 1994, Stuttgart: B. G. Teubner Stuttgart.
19. Jenke, M.G., C. Santschi, et al., *Two-dimensional electrostatic force field measurements with simultaneous topography measurement on embedded interdigitated nanoelectrodes using a force distance curve based method*. Applied Physics Letters, 2008. **92**(6): p. 063113-3.



---

## **EFM Results: Characterisation**

This chapter is dedicated to the characterization of the new Electrostatic Force Microscopy (EFM) method introduced in chapter 7 and EFM in general. It will answer the questions: How does the tip shape and environment influence the measurement? Which tip diameter should be used for which pitch? Where are the limits of the new EFM method? Moreover, we will present an analytical equation, which enables us to calculate the vertical electrical force field without performing numerical simulations.

### **8.1) Influence of Tip Shape Discrepancies**

As mentioned at the end of chapter 7 slight tip shape differences influence the measured force. To proof this and to investigate in more detail the influence of the tip shape we performed simulations with two modified tips and compared them with the simulations of a non-modified tip (tip radius: 300 nm). Figure 8-2 (a) and 8-3 (c) show the two modified tips, one has a half sphere (diameter: 100 nm) on the upper part of the tip (modtip1) and the other further down (modtip2). Figure 8-1 shows the simulated vertical force field of the non-modified tip and modtip1.

The force field with modtip1 decreases differently by moving from one electrode to the next one. The maximal force of the modified tip is much higher, about 25 nN, in comparison with the non-modified tip.

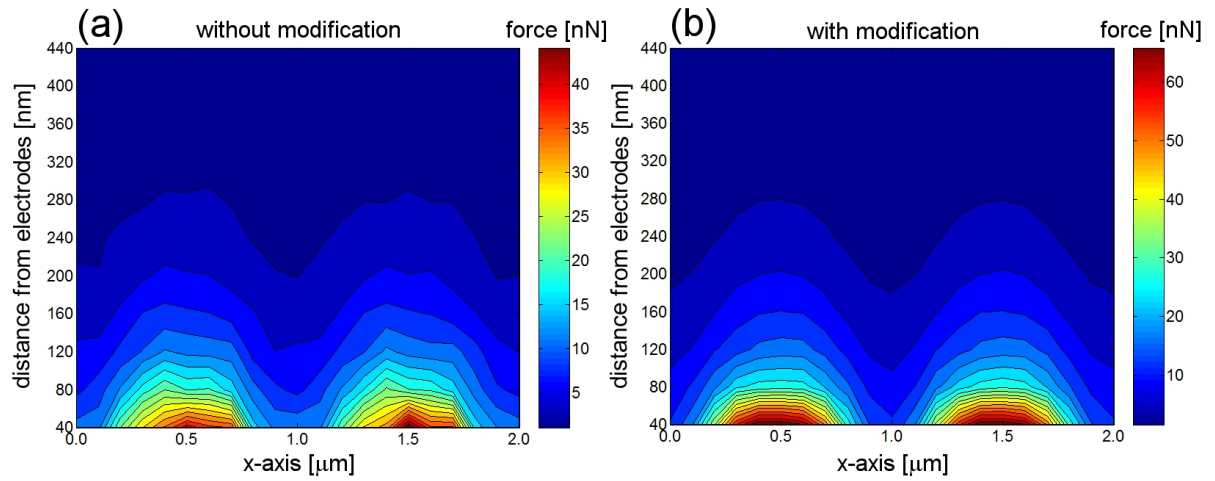


Figure 8-1: Simulated force fields of 500 nm pitch electrodes. Obtained with (a) a tip of 300 nm tip radius and (b) a tip of 300 nm tip radius with an added half sphere (as shown in figure 8-2). On the electrodes +20 V and -20 V were applied, alternately. The added half sphere changed the shape of the obtained field and it's maximal force.

Figure 8-2 presents the two force fields as a function of the vertical distance from the electrodes at two places on the surface, one in the center of an electrode and one between two interdigitated electrodes, corresponding to the x positions 0.5  $\mu\text{m}$  and 1  $\mu\text{m}$  in figure 8-1 (a) and (b), respectively.

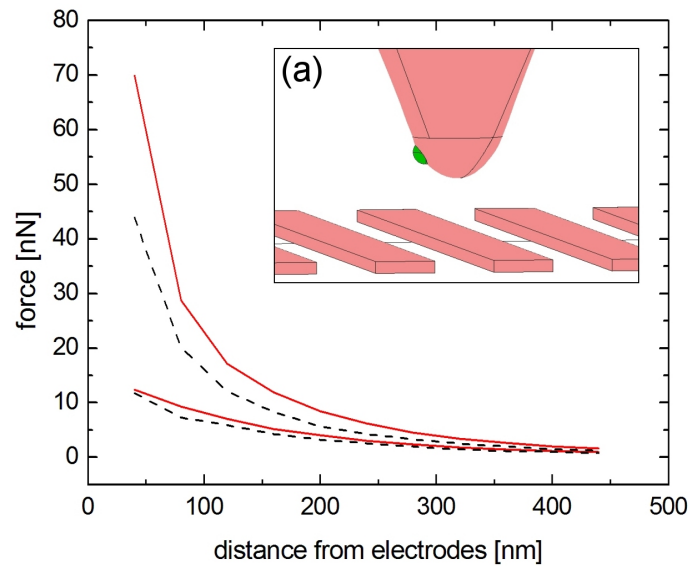
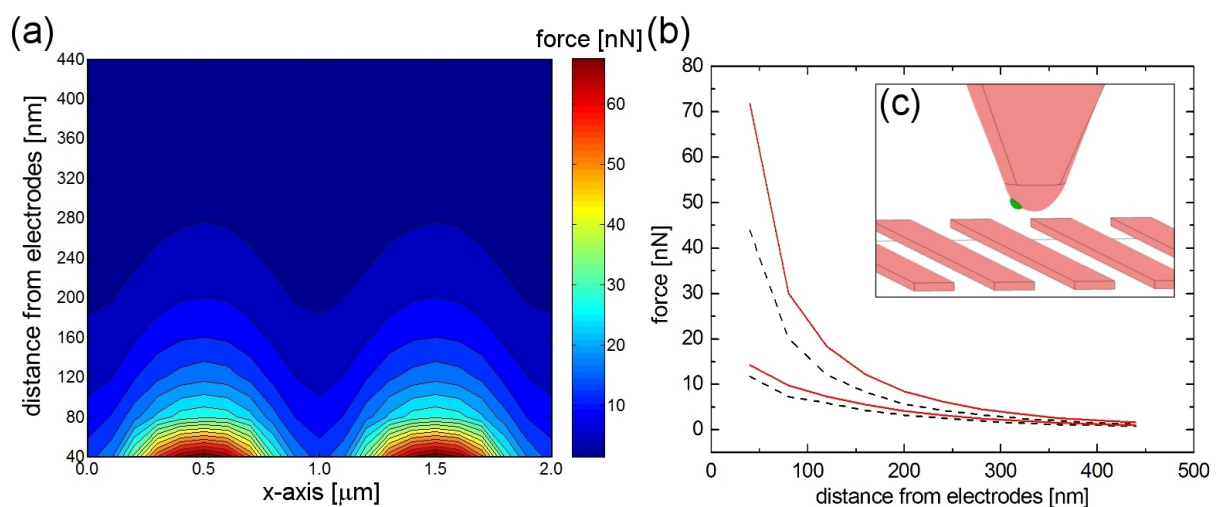


Figure 8-2: Force vs. distance from surface graph obtained in the center of an electrode and in between two interdigitated electrodes. Simulated with the modified tip shown in (a) (solid lines) and a not modified tip (dashed lines).

The maximal attraction of modtip1 above the electrodes is about 45 % higher as the one with no modification. This is a high force increase for a surface increase of only about  $0.01 \mu\text{m}^2$ . The force difference between modtip1 and the non-modified tip decreases fast increasing distance. In contrast, the attraction force of modtip1 between the electrodes is at all distances only slightly higher as the attraction force of the non-modified tip.

What happens if the half sphere is positioned even closer to the electrode surface? Figure 8-3 (a) and (b) show this situation (modtip2).



*Figure 8-3: Force field (a) and force vs. distance graph (b) of a second modified tip (red solid line), presented in (c). The shape of the force field didn't change in comparison with modtip1. The attraction force on and between the neighbouring electrodes increased by 3 nN. (black dashed line: Force vs. distance graph of the unmodified tip.)*

The maximal force above the electrodes increased once more, but only by about 3 nN, from 70 to 73 nN (figure 8-3 (b)). The force between the electrodes increases by about the same value. Therefore, the effect of the moving of the half sphere seems to be negligible.

To conclude, tip shape differences that result in total area changes of only  $0.01 \mu\text{m}^2$  change the maximal force by about 45 % and the shape of the total force field. However, their influence decreases fast with increasing distance. The position of the tip shape discrepancies seems to have a negligible

influence. This means, EFM measurements are extremely sensitive to any kind of surface changes, including shape and roughness changes.

All these conclusions can be applied, only in the case that the tip shape discrepancies are within the E-field and not closer to the surface than the main tip. When they are outside of the E-field, their influence on the force is negligible. If the tip shape discrepancies are closer to the surface than the tip they have an influence on the tip-sample distance, which have to be taken into account.

## 8.2) Resolution of EFM

In order to determine the resolution of our force field measurements we need first to define the term resolution. Typically when one talks about resolution one means the spatial resolution. The spatial resolution is the minimum distance between two individual objects that can be distinguished with the used measurement method. This distance is often defined by a ratio between the maxima and the minima of the measured signals as shown in figure 8-4.

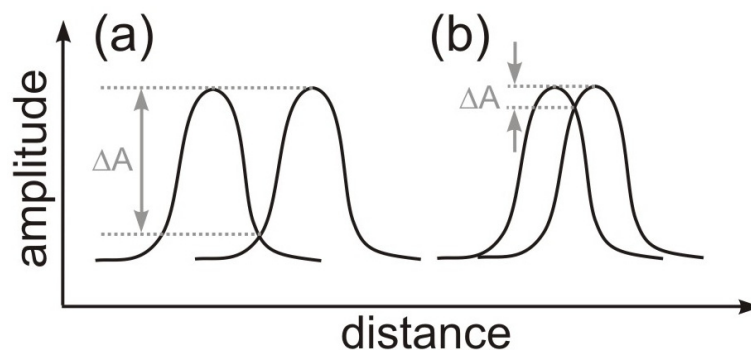


*Figure 8-4: Schematic drawing of two amplitudes obtained from two separate objects at two different distances: (a) The two amplitudes are well spaced and the difference ( $\Delta A$ ) between curve maxima and minima is high. The two objects are well resolved. (b) The two amplitudes are very close together. The difference ( $\Delta A$ ) between curve maxima and minima is therefore low and the two objects are hardly distinguishable.*

Based on this definition we define the resolution as the difference between the maximal force ( $F_{\max}$ ) and minimal force ( $F_{\min}$ ) divided by  $F_{\max}$ . To determine this force ratio we averaged the force values at 4 different x-axis positions and at several tip-sample distances (figure 8-5, pos1 to pos4).

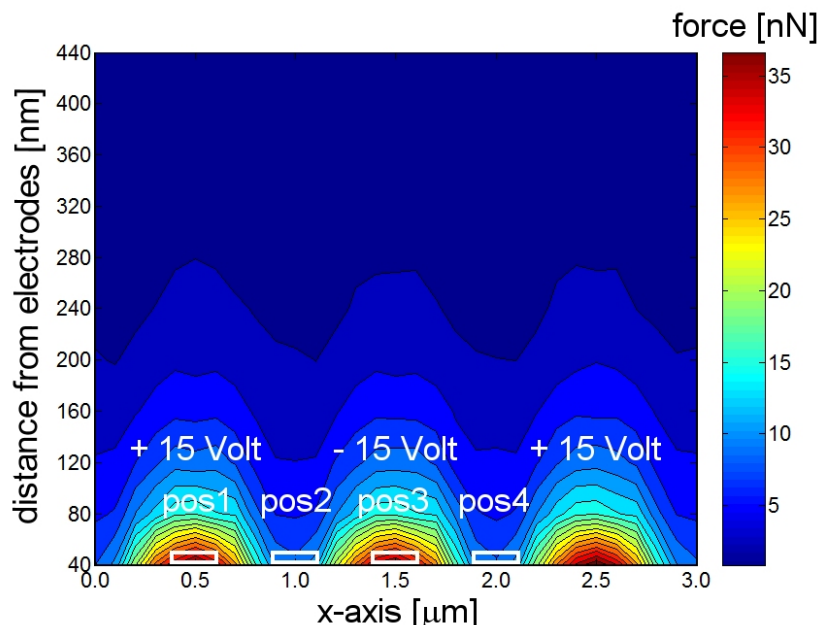


*Figure 8-5: Position of the force field values taken, to determine the difference and ratio between  $F_{\max}$  and  $F_{\min}$ .*

Afterwards, we calculated the force differences ( $F_{\max} - F_{\min}$ ) and the force ratios  $((F_{\max} - F_{\min}) / F_{\max})$  between these positions in function of the tip-surface distance. This results in four force differences and ratios for each tip-surface distance, which we averaged to get one force difference and force ratio value per distance (figure 8-5).

These calculations are performed on several simulated force fields. We simulated the force field above 63, 125, 250, 500 and 1000 nm pitch electrodes with +15 and -15 Volts applied (figure 8-5), determined with tip radii of 50, 100, 200, 300, 400, 500, 600 and 700 nm. Moreover, the force field above the 300 nm pitch electrodes was determined for applied voltages between 5 and 30 Volts in steps of 5 Volts using a tip with a tip radius of 300 nm. We performed as well measurements with three different tip radii on

500 nm pitch electrodes with +15 and -15 Volts applied on the electrodes and for a tip radius of 300 nm, with +20 and -20 Volts applied. However, one has to be aware, that we always simulated tips with the same “main body” geometries (as shown in figure 8-6). Only the radius of the tip changed during the calculation.

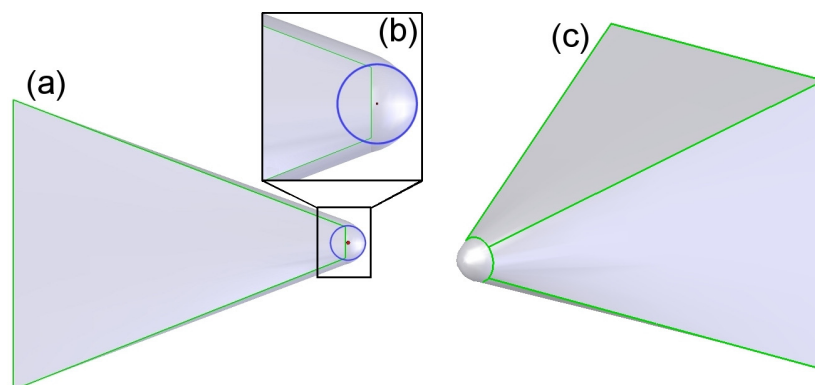


*Figure 8-6: 3D model of a tip with 300 nm tip radius. (a) Side view: The tip is about 6  $\mu\text{m}$  high and has a maximal width of about 2.5  $\mu\text{m}$ . (b) Zoom on the tip area of (a). The (blue) circle represents the tip radius of 300 nm. The centre of this circle is about 50 nm away from the vertical (green) line, which represents the beginning of the tip curvature. All tip models in this sub chapter have these dimensions. Only the tip radii are changing. (c) shows a perspective view on the tip.*

This is done in order to be able to compare better the influences of the tip radius. Tips that are fabricated with the method presented in chapter 4 or others can have a shape that differs from the simulated shape. The tip shape differences have a huge influence on the measurements as shown before, therefore, the simulated values can differ from the measurements.

Figure 8-7 presents the simulation results of the 63 nm pitch electrodes. The force field above the electrodes decreases rapidly in the first 100 nm. The force ratio to distance curves are very irregular, but it seems that the force ratio curves of the 100, 200 and 300 nm tip radius decreases in average with distance in a similar manner. The best resolution is, therefore, given by a 100 nm, 200 nm or 300 nm tip. This corresponds to a pitch to tip radius ratio  $R_{TR}$  between 1.6 and 4.8.

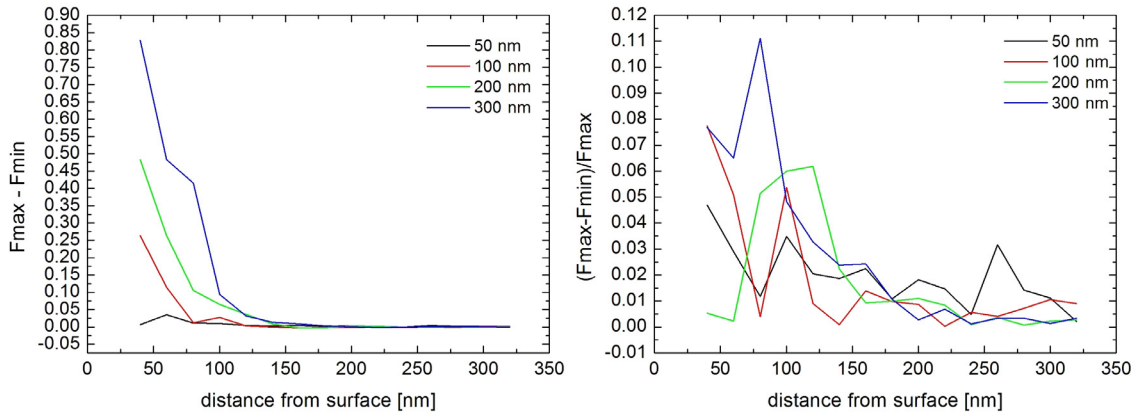


Figure 8-7: Simulated difference and ratio between  $F_{max}$  and  $F_{min}$  above 63 nm pitch electrodes.

Figure 8-8 shows the results obtained for the 125 nm pitch electrodes. The force difference decreases rapidly with increasing distance and becomes nearly 0 at a distance of about 250 nm from the electrode surface. The force ratio  $(F_{max}-F_{min})/F_{max}$  decreases rapidly as well until a distance of about 300 nm and is then nearly constant. It is remarkable that a tip with a radius (500 nm) or 4 times the pitch (125 nm) still delivers a high resolution. The best resolution with distance is obtained with a tip radius of 300 nm, because it has the highest force ratio with distance. This corresponds to an  $R_{TR}$  of 2.4. The highest force difference is obtained with a 500 nm tip.

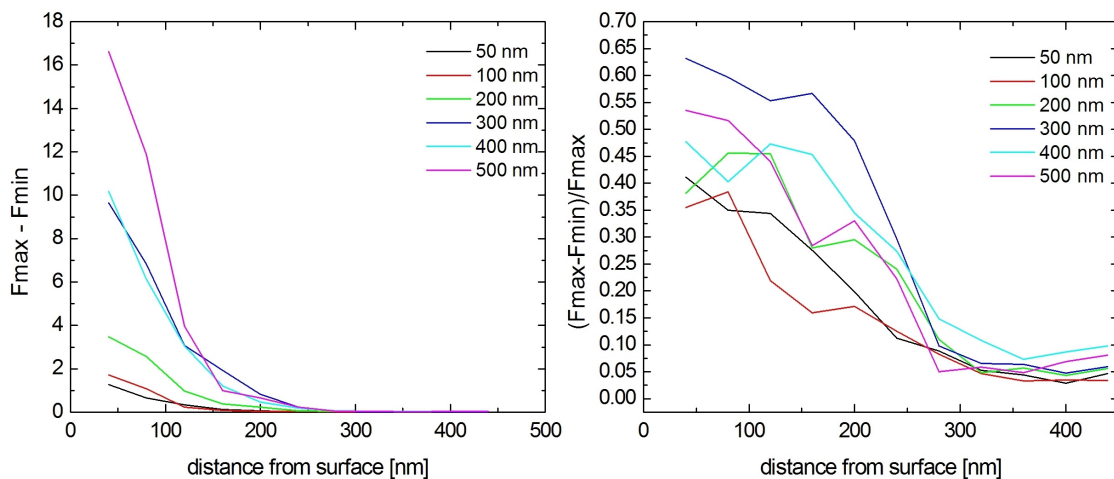
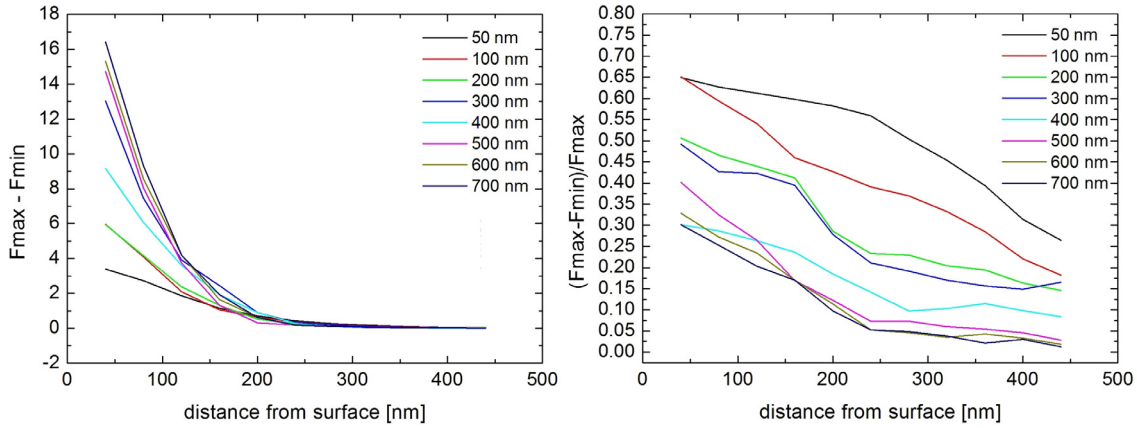


Figure 8-8: Simulated difference and ratio between  $F_{max}$  and  $F_{min}$  above 125 nm pitch electrodes.



The electrodes with 250 nm pitch (Figure 8-9) shows a similar behaviour. The best resolution with distance is given with tip radii of 50, 100 and 500 nm, this corresponds to an  $R_{TR}$  of 0.2, 0.4 and 2. The highest force difference is obtained with a 700 nm tip, whereas the force difference increases more slowly for tip radii bigger than 500 nm.



*Figure 8-9: Simulated difference and ratio between  $F_{max}$  and  $F_{min}$  above 250 nm pitch electrodes.*

It seems, that an  $R_{TR}$  of 2 to 2.5 delivers a good resolution for all presented pitches. In the case of the following electrodes with 500 nm pitch this would be equal to a tip radius of 1000 nm to 1250 nm. These large tip radii are, however, not realisable with our fabrication method (chapter 4). Therefore, we have chosen to use spheres instead of tips. This is a radical change in geometry and influences strongly the results, but is closer to reality. Furthermore, the change in geometry enables to test if a  $R_{TR}$  of 2 to 2.5 delivers the best resolution as well for cantilevers with attached spheres.

Figure 8-10 and 8-11 presents the simulation results of the 500 nm and 1  $\mu\text{m}$  pitch electrodes, respectively. The best force ratio above the 500 nm pitch electrodes is obtained with a sphere of 1  $\mu\text{m}$  radius, and above the 1  $\mu\text{m}$  pitch electrodes with a sphere of 2  $\mu\text{m}$  radius, which corresponds to an  $R_{TR}$  of 2 in both cases. These results confirm our before made observations that the best force resolution on interdigitated electrodes is obtained with a pitch to tip/sphere radius ratio of 2 to 2.5. The highest force difference on both



electrodes is obtained with the largest sphere, whereas the force difference increases more slowly for radii bigger than  $R_{TR} = 2$ .

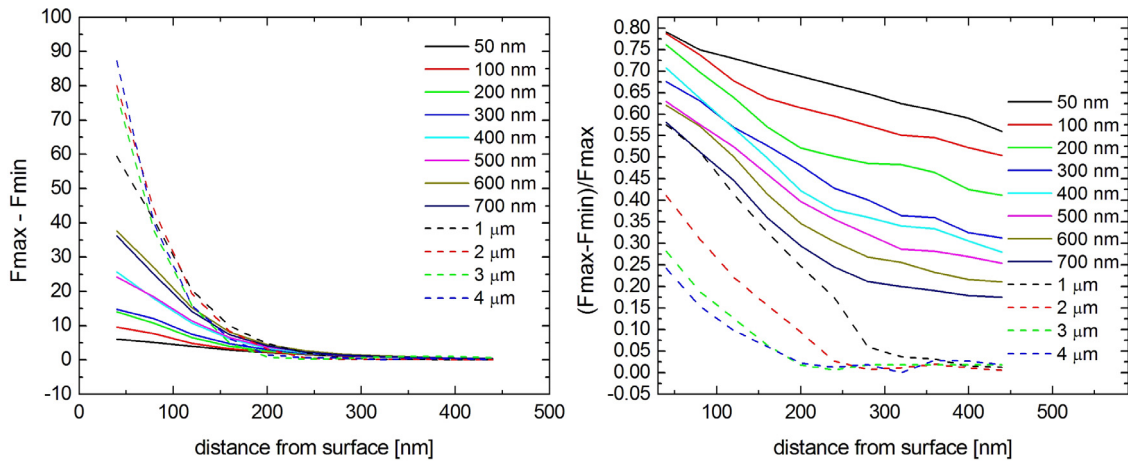


Figure 8-10: Simulated difference and ratio between  $F_{max}$  and  $F_{min}$  above 500 nm pitch electrodes.

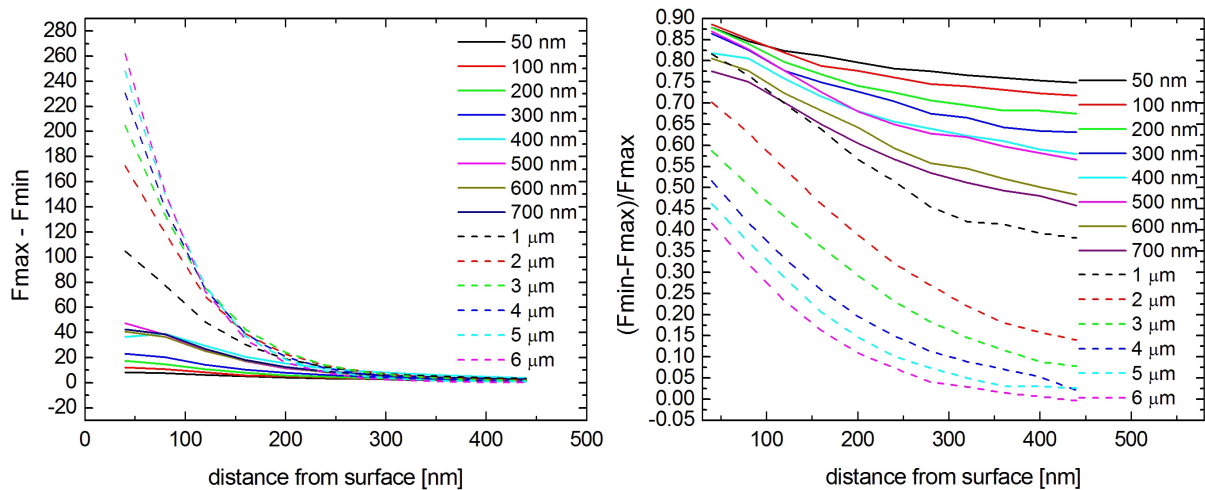
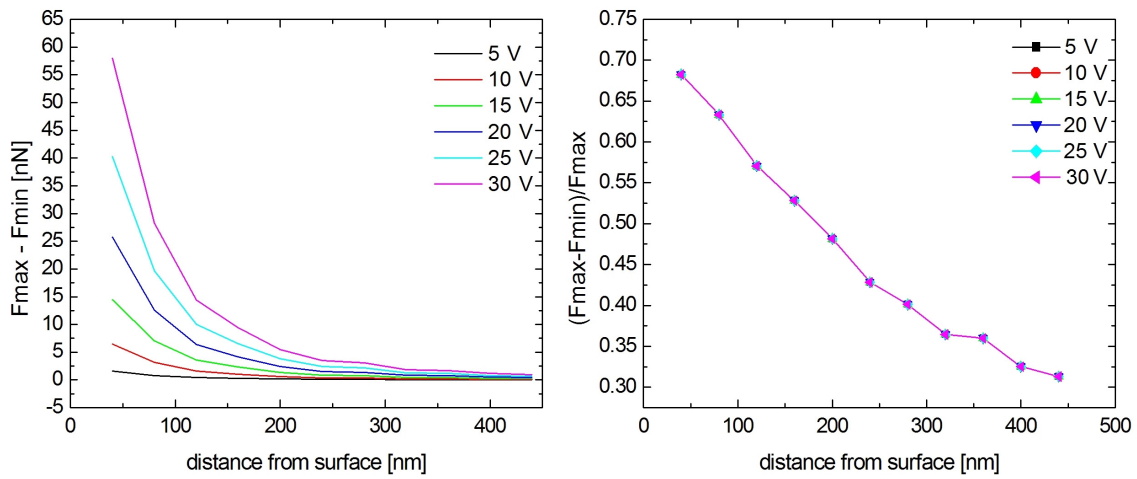


Figure 8-11: Simulated difference and ratio between  $F_{max}$  and  $F_{min}$  above 1000 nm pitch electrodes.

How does the force field develop with applied voltage?

We simulated the force field above 500 nm pitch interdigitated electrodes with  $\pm 5$ ,  $\pm 10$ ,  $\pm 15$ ,  $\pm 20$ ,  $\pm 25$  and  $\pm 30$  Volt applied, alternately, and obtained with a tip radius of 300 nm. Figure 8-12 shows the force differences and ratios as a function of applied voltage.



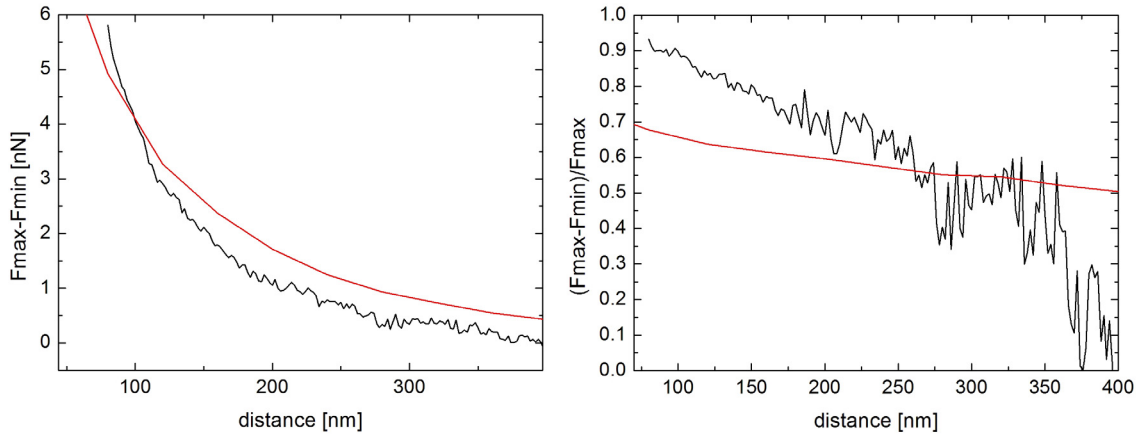
*Figure 8-12: Force difference and ratio between  $F_{\max}$  and  $F_{\min}$  for different Voltages above 500 nm pitch electrode simulated with a tip with a radius of 300 nm. The force ratio is independent of the applied voltage (all curves coincide).*

We can clearly see that the force ratio is independent of the applied voltage (all curves coincide) and depend therefore only on the used geometries (tip and electrodes). The force difference and range increases with the applied voltage. Whereas the shape of the curve is always the same only the obtained maximal forces increase with applied voltage.

How well do these simulations fit the measurements?

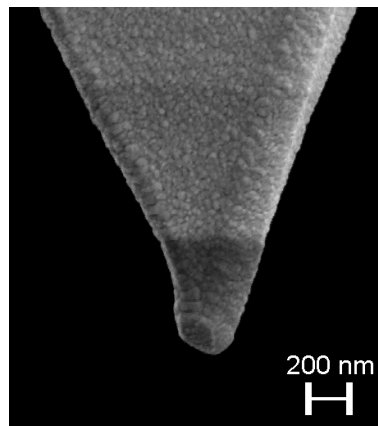
To answer this question we measured the force field above 500 nm pitch electrodes with tips of 100 nm, 300 nm and 1000 nm radius with +15 and -15 Volts and for a tip radius of 300 nm as well with +20 and -20 Volts applied on the electrodes, alternately.

Figure 8-13 shows the results of the measurements, performed with a tip radius of 100 nm. The force difference curve of the measurement decreases faster with the distance than the force differences curve of the simulation. The difference between these two curves is always about  $\pm 1$  nN. The measured force ratio curve doesn't fit well with the force ratio curve of the simulation.



*Figure 8-13: Comparison of measured and simulated force difference and ratio between  $F_{max}$  and  $F_{min}$  above 500 nm pitch electrodes. Obtained with a tip with a radius of 100 nm and an voltage of  $\pm 15$  Volt applied on the electrodes, alternating.*

The simulated force ratio curve is about 0.2 lower at a distance of 100 nm and about 0.4 higher at a distance of 400 nm than the measured force ratio curve. This indicates that the differences between the measured and simulated curves may result from tip shape differences. Indeed, the tip shape of the simulated tip differs from the real tip. As shown in figure 8-14, the real tip is at its end longer as the simulated tip.



*Figure 8-14: Real tip with 100 nm radius.*

Figure 8-15 presents the measurement results with the 300 nm tip radius. The

measured and simulated force difference curves fit perfect. The simulated force ratio curve doesn't fit well again with the measured force ratio curve, at a distance of 100 nm. The measured force ratio is about 0.2 higher than simulated. This difference decreases with the distance.

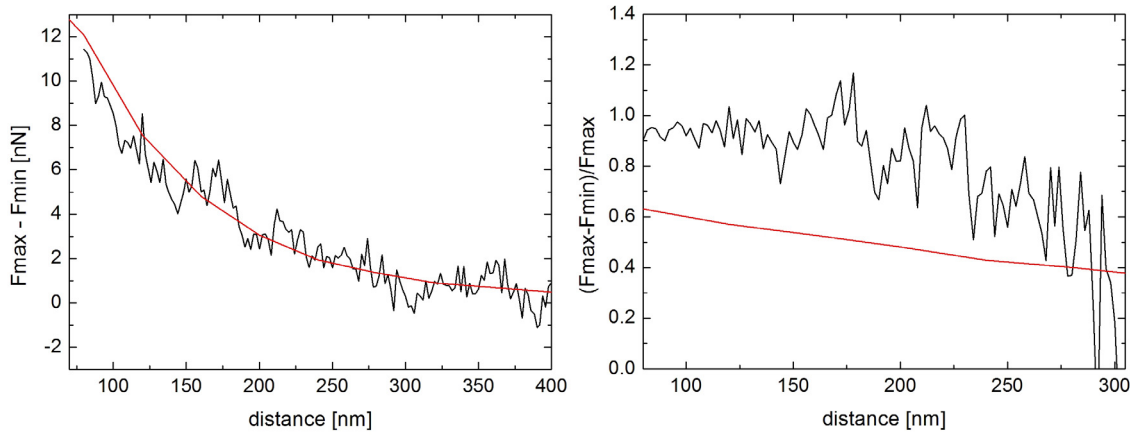


*Figure 8-15: Comparison of measured and simulated difference and ratio between  $F_{\max}$  and  $F_{\min}$  above 500 nm pitch electrodes, obtained with a tip with a radius of 300 nm and a voltage of  $\pm 15$  V applied on the electrodes, alternately.*

The same behaviour appears for the tip with 500 nm radius. The results of these measurements are presented together with the simulations in figure 8-16.

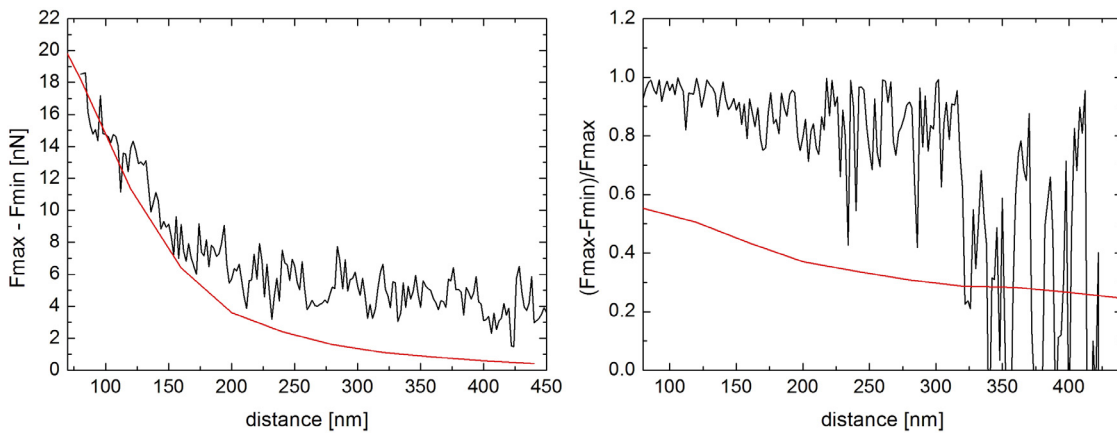


*Figure 8-16: Comparison of measured and simulated difference and ratio between  $F_{\max}$  and  $F_{\min}$  above 500 nm pitch electrodes, obtained with a tip with a radius of 500 nm and a voltage of  $\pm 15$  V applied on the electrodes, alternately.*

The measurement with  $\pm 20$  V is presented in figure 8-17. The results are once more similar to the previous results. The force difference curve of the simulation and measurement fits well, whereas the force ratio curves differ by about 0.2 to 0.4.

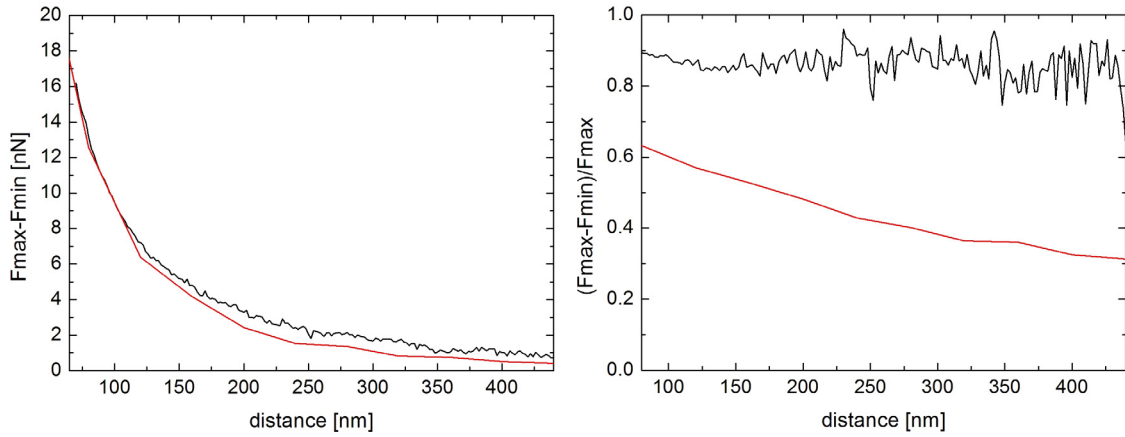


*Figure 8-17: Comparison of measured and simulated difference and ratio between  $F_{\max}$  and  $F_{\min}$  above 500 nm pitch electrodes. Obtained with a tip with a radius of 300 nm and  $\pm 20$  Volt applied.*

To conclude, the force difference ( $F_{\max} - F_{\min}$ ) curves of the simulations and measurements fit well. On the other hand, the force ratios curves always differ by about 0.2 to 0.4. Probably, this results from small tip shape differences between the 3D model and the real tip, because the force ratio is much more sensitive to tip shape differences than the force difference.

The noise in the force ratio measurements increases with increasing distance. The maximum shown distance in the force ratio graphs, is the distance at which the force ratio starts to fluctuate over the whole y-axis range. This is the case at a distance of 400 nm for a tip radius of 100 nm, at a distance of 300 nm for the tip radius of 300 nm and at a distance of 350 nm for a tip radius of 500 nm. When we increase the applied voltage to  $\pm 20$  V the distance increases to 475 nm for a tip with a radius of 300 nm. This indicates that a higher applied voltage improves the signal to noise ratio. In addition, the results of the 100 nm tip indicate that it is favourable to use tips with steep side walls.

### 8.3) Resolution Comparison between Force Field and Topography

As discussed, we measure with our new EFM method the force field and the topography of the sample simultaneously. This has the advantage that we can assign to every force measurement a position on the surface and a distance from this surface position. This is an additional advantage compared to other EFM methods.

To do this we measure the topography in a similar manner as a normal AFM contact scan. The major problem of the AFM contact mode is that the measured topography is a convolution of tip and sample geometry. In order to determine the dependence between tip, pitch and resolution we used the following simplified geometry:

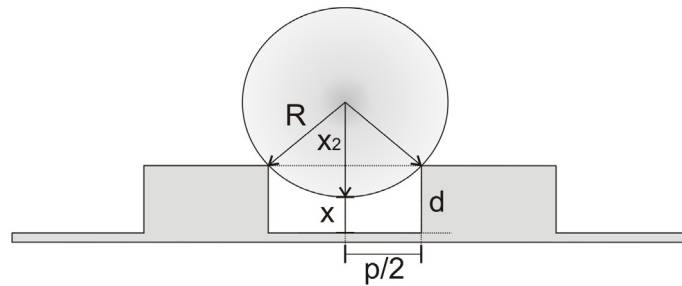


*Figure 8-18: Schematic drawing of the geometrical relationships between tip radius (R) and electrode pitch (p).*

Using geometric relationships we developed the following equation, which allows one to calculate x as function of R, p and d:

$$x = d - \left( R - \sqrt{R^2 - \left( \frac{p}{2} \right)^2} \right) \quad \text{Eq. 8-1}$$

With this equation one can calculate the ratio  $x/d$ , which provides a value for the topographical resolution. The dependence of this ratio on  $R$  and  $p$  is shown in figure 8-19,  $d$  is kept equal to  $p/2$ :

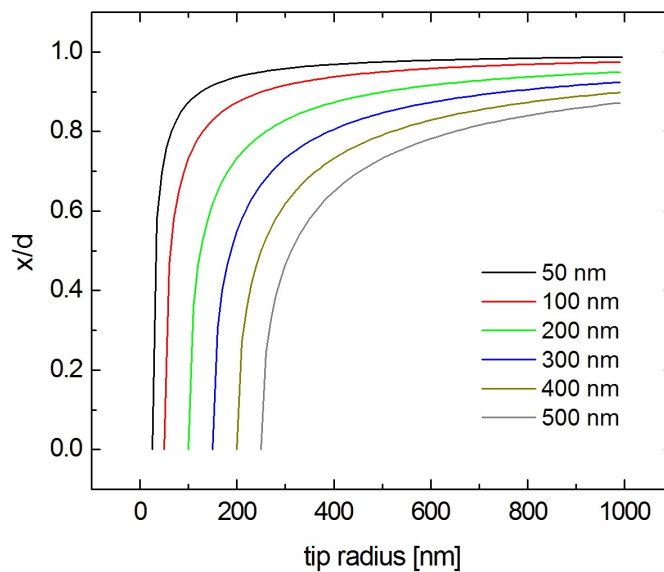


*Figure 8-19: Ratio  $x/d$  vs. tip radius ( $R$ ) for different electrode pitches. The ratio  $x/d$  is a measure for the topographical resolution.*

The figure reveals, a tip with 300 nm radius does not touch the substrate while scanning 500 nm pitch electrodes, if the electrodes are thicker than 120 nm. This calculation does not take into account that a  $\text{SiO}_2$  layer is deposited onto the electrodes for electrical isolation, which reduces the distance between the electrodes. However, for a rough calculation of a  $x/d$  vs. tip radius graph the electrode pitch can be still used.

Combining these calculations with the results of the previous chapters, the ideal tip for force field measurements has the following characteristics:

- To have a sufficient topographical resolution one should choose a value for  $x/d$  that is well below the bending of the  $x/d$  vs. radius graph. For the 500 nm pitch electrodes this is the case with an  $x/d$  ratio of about 0.5. The corresponding tip radius is 300 nm, calculated by the following equation:

$$R = \left( \frac{-1 + (x/d - 1)^2}{2(x/d) - 2} \right) \left( \frac{p}{2} \right) \quad \text{Eq. 8-1}$$

- With a tip radius to pitch ratio between 2 and 2.5, the best measurement results of the force field can be obtained. This is contradictory to the last point. Therefore, one can measure only either the force field or the topography precisely, or make a compromise between the two.
- The height to width ratio of the tip and the applied voltage should be both as high as possible in order to have a good signal to noise ratio. However, the applied voltage should not be too high, because high voltages lead to charge injection into the oxide or damage to the electrodes. These topics will be discussed in chapter 9.

## 8.4) Force Field of 50 nm Pitch Electrodes

In order to show the limits of the new EFM method, but as well how small forces and electrode pitches can be observed with it, we fabricated 50 nm pitch electrodes and measured their force fields. We used a highly doped silicon tip with a nominal tip radius of about 10 nm, a force constant of 0.26 N/m and steep side walls. The tip was checked using SEM before and after the measurement, and did not change visibly.

Figure 8-20 shows the result of the measurement. The surface and the corresponding force field are presented. The topography and force field were recorded every 10 nm. These steps are visible in the graph. The force field is quite fragmented but still well resolved. The fragmentation is so high because we measure force difference of less than 0.1 nN. This high electrostatic force resolution is to our knowledge only possible at the moment with the new developed EFM measurement method. Normal layered imaging methods or single FDC based methods have a too low signal to noise ratio, as



indicated in figure 9-3 (a) and (b), to measure such small electrostatic forces.

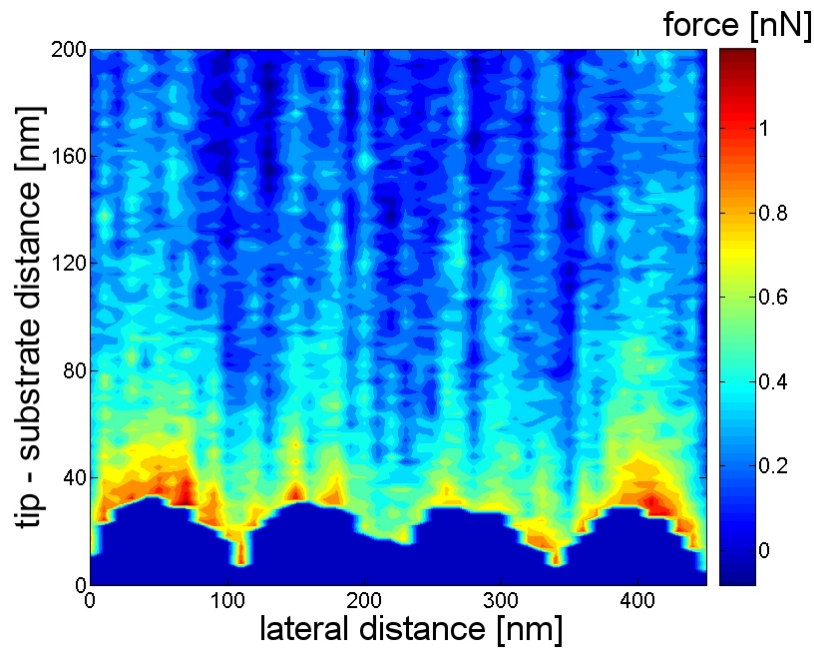


*Figure 8-20: Measured vertical electrostatic force field of 50 nm pitch electrodes. Obtained with a tip with a radius of about 10 nm and  $\pm 5$  V applied on the interdigitated electrodes, alternately.*

## **8.5) Influence of Humidity on the Force Field**

In order to determine the influence of the humidity on the force field, we measured the force field above 500 nm pitch electrodes using a tip with a radius of about 350 nm, at different relative humidities. In detail, we measured the force field at about 0 %rh, 30 %rh and 60 %rh. Figure 8-21 shows the resulting force fields. Roughly comparing figure 8-21 (a) to (c) one can see that the force field becomes more homogeneous and stronger with humidity. An increase of the humidity from 0 %rh to 30 %rh has nearly no influence, further increasing to 60 %rh significantly increases the forces.

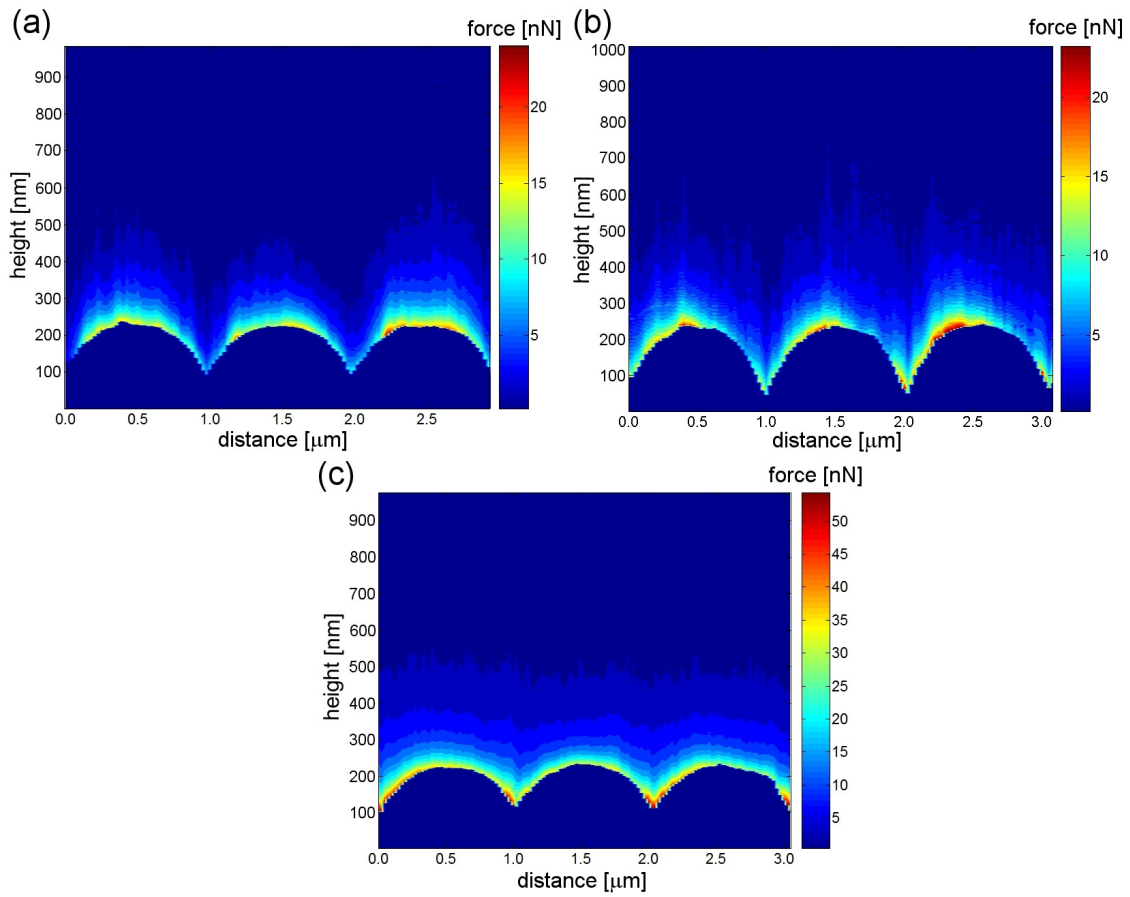
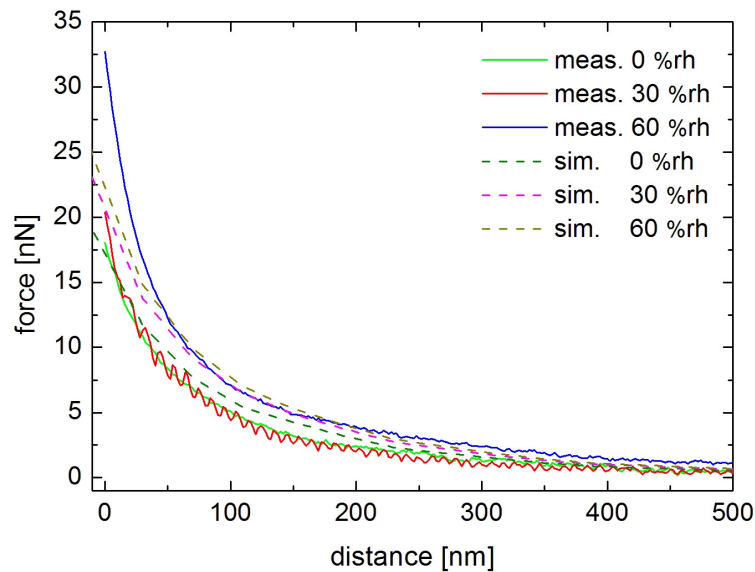


Figure 8-21: Measured vertical force field of 500 nm electrodes, obtained with a tip radius of 300 nm, with  $\pm 20$  Volt applied at (a) 0 %rh, (b) 30 %rh and (c) 60 %rh.

Figure 8-22 shows a detailed comparison of the force progression versus distance above the electrodes. The force at 60 %rh is about 13 nN higher at the first nanometers from the electrodes in comparison with 0 %rh and 30 %rh. This difference decreases with distance. Figure 8-22 shows, as well, a simulation of the force field of a tip with 350 nm tip radius for 0, 30 and 60 %rh. According to Picard et. al.<sup>1</sup> the relative permittivity of air increases with humidity. The relative permittivity is 1,0 for 0 %rh, 1,1485 for 30 %rh and 1.2391 for 60 %rh. We increased for our simulation the relative permittivity in the space between tip and electrodes according to these values. The simulation fits quite well for 0 %rh and for 60 %rh to a distance of about 50 nm, and for 30 %rh until a distance of about 200 nm. The simulated force of 30 %rh is always about 1 to 2 nN too high for distances below 200 nm, and for 60 %rh

up to 15 nN to low for distances below 50 nm.



*Figure 8-22: Detailed comparison of the force field vs. distance above the electrodes shown in figure 8-21 for 0, 30 and 60 %rh. The measured (meas.) and simulated (sim.) force fields are presented.*

Both measurements, at 30 %rh and 60 %rh, show a strong increase close to the surface, 60 %rh much more than 30 %rh. This increase results from the water film on the surface of the electrodes and tip<sup>2</sup>. The water film can influence the electrostatic force close to the surface by two ways:

- 1.) The closer we come to the surface, the more contribute the two water films to the total relative permittivity (water film/air/water film) between tip and surface, similar to the increase of the relative permittivity with the humidity.
- 2.) Or the strong electrical fields between tip and substrate increase the desorption of water molecules from the water film and increase, therefore, the relative permittivity between tip and surface. Due to the fact that the E-field increased with decreasing distance, this effect increases, as well, with decreasing distance. The first layers of a water

film are usually ordered water, which are more strongly bound than the higher (volume) water layers. At 30 %rh one has only ordered water on the surface and the strength of the electric field is most likely not high enough to increase the desorption of water molecules. At 60 %rh one has loosely bound volume water on the top of the water layer, there it is much easier for the electrical field to increase the desorption of water molecules.

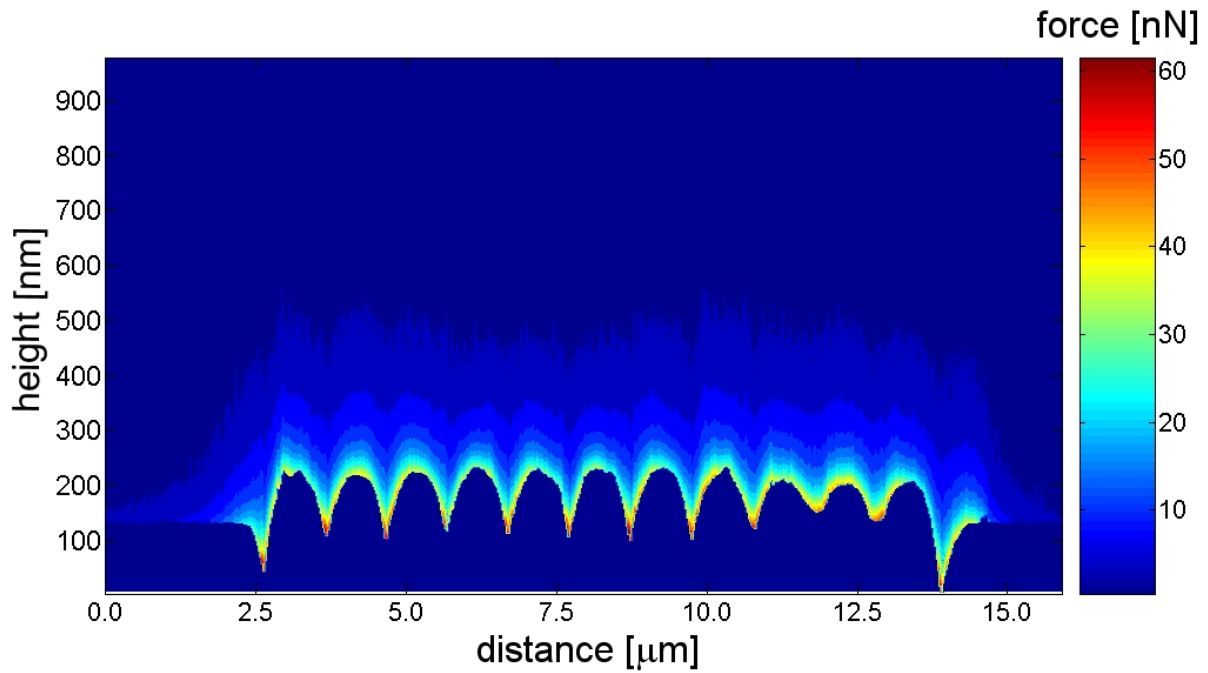


*Figure 8-23: Full scale measurement of the vertical force field of 500 nm electrodes, obtained with a tip radius of 300 nm, with an applied voltage of  $\pm 20$  Volt and at 60 %rh.*

So far, we have presented only measurements over 3 or 4 electrodes. The measurements can as well be done over many more electrodes. To show this we present in figure 8-23 the force field measured along the entire electrode length.

## 8.6) Analytical Force Field Description

Due to the numerical simulations performed in the previous chapters, we are

now able to develop an empirical equation for the force field above 500 nm pitch electrodes, with a tip radius of 300 nm. Similar expressions can be developed for all other cases using the presented approach.

Due to the periodical character of the interdigitated electrodes one can approximate the force variation perpendicular to the interdigitated electrodes by a sinusoidal (figure 8-24) function of the form:

$$F_{(pos)} = A + B \times \sin\left(\pi\left(\frac{x-C}{D}\right)\right) \quad \text{Eq. 8-3}$$

where A and B can be expressed by  $F_{\max}$  and  $F_{\min}$ :

$$A = \frac{F_{\max} - F_{\min}}{2} + F_{\min} \quad \text{Eq. 8-4}$$

$$B = \frac{F_{\max} - F_{\min}}{2} \quad \text{Eq. 8-5}$$

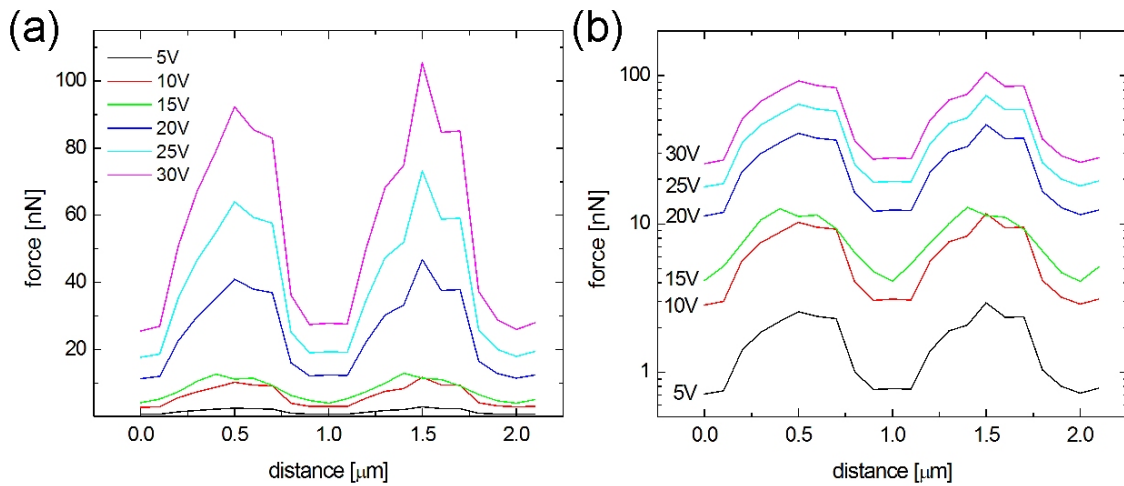


*Figure 8-24: Simulated force at different voltages above 500 nm pitch electrode, obtained at a height of 40 nm from the electrodes with a tip radius of 300 nm.*

Figure 8-25 (b) shows that the ratio of  $F_{\min}/F_{\max}$  changes with the square root of

the distance independently of the applied voltage. This graph can be approximated by:

$$\frac{F_{\min}}{F_{\max}} = A + B\sqrt{z} \quad \text{Eq. 8-6}$$

where  $z$  is the distance from the surface.

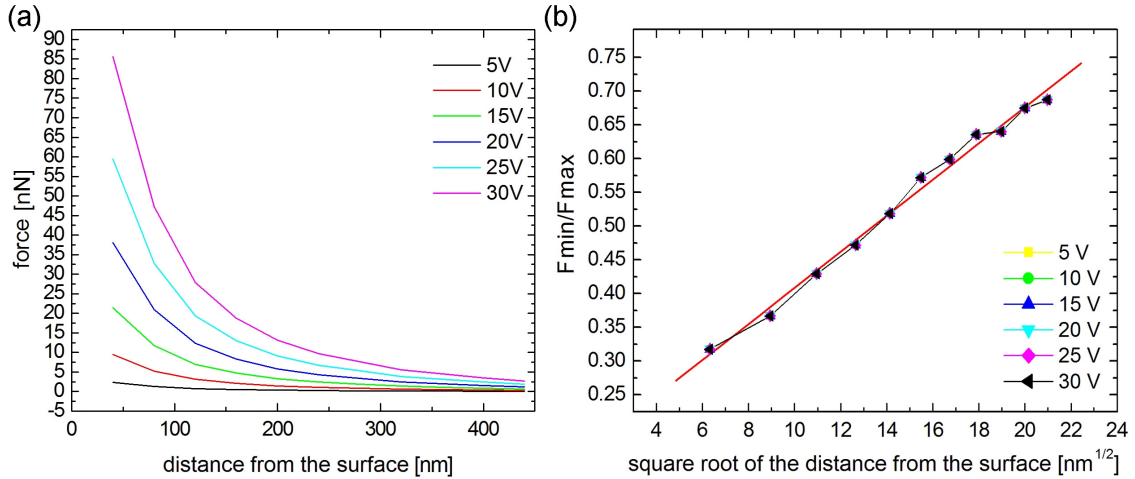


Figure 8-25: (a) Simulated force and (b) ratio between  $F_{\max}$  and  $F_{\min}$  vs. distance from electrodes.

The square root dependence of  $z$  results from the  $1/z^2$  dependence of the force from the distance. The maximal force variation with distance and applied voltage is presented in figure 8-25 (a).

These variations of the maximal force can be expressed by:

$$F_{\max} = BV^2 \quad \text{Eq. 8-7}$$

where  $V$  is the applied voltage on the electrodes.  $F_{\max}$  depends quadratic on  $V$  because of:

$$\vec{F} = \int_A \frac{\sigma \vec{E}}{2} dA \quad \text{with} \quad \sigma = \epsilon_0 \epsilon_r |\vec{E}_{\perp}| \quad \text{results in} \quad \vec{F} = \epsilon_0 \epsilon_r \int_A \left( \frac{|\vec{E}_{\perp}|^2}{2} \right) dA \quad \text{Eq. 8-8}$$

Using equation 8-6 and 8-7 we can express  $F_{\min}$  using  $F_{\max}$  and calculate  $F_{\max}$  by knowing the applied voltage and tip-electrode distance. Combining this

with equations 8-3 to 8-5 enables one to obtain an equation that allows to calculate the force above the electrodes for all positions of the tip and for all applied voltages.

$$F_{(x,z,V)} = C_1 V^2 \cdot \left( C_2 + 3\sqrt{z} + (10 - \sqrt{z}) \cdot \sin \left( \pi \left( \frac{x - C_3}{C_4} \right) \right) \right) \quad \text{Eq. 8-9}$$

where  $C_1$  to  $C_4$  are constants:  $C_1 = 0.00134$ ,  $C_2 = 65$ ,  $C_3 = 0.2$ ,  $C_4 = 0.54$ .

## 8.7) Bibliography of Chapter 8

1. Picard, A. and H. Fang, *Methods to determine water vapour adsorption on mass standards*. Metrologia, 2004. **41**(4): p. 333-339.
2. Opitz, A., *Nanotribologische Untersuchungen von ultradünnen Wasserfilmen auf hydrophoben und hydrophilen Siliziumoberflächen*, in *Mathematik und Naturwissenschaften*. 2003, Technische Universität Ilmenau: Ilmenau. p. 110.





## **EFM Results: Hints and Interesting Aspects**

We presented and characterized in the previous chapters a new Electrostatic Force Microscopy (EFM) method. On the way to these results we encountered several problems and found interesting aspects of EFM on nanoelectrodes. In this chapter we present a few of these problems and aspects, which are either very important for future EFM measurements or will enable new applications. We will give, as well, some practical advice for doing EFM measurements.

### **9.1) Cantilever Influence**

One often discussed topic concerning EFM is the influence of the cantilever on the measurements, which was neglected in the early times of EFM. Sacha et al<sup>1</sup> have shown that this is not correct, and that the cantilever must be taken into account. This holds for microelectrodes, but not for nanoelectrodes. The simulations in the last chapters have shown, that the cantilever has no influence on EFM measurements of nanoelectrodes, due to the confinement of the field near the surface. It is sufficient to simulate the first few  $\mu\text{m}$  of the cantilever tip to obtain simulation results that fit well with the measurements. This simulations show as well that the tip apex contributes most to the total measured force (figure 7-1). Therefore,  $z_3$ , the tip apex to sample distance was chosen as the distance of the measured force from the surface (figure 6-2 and 9-1 (a)).

However, we agree with Sacha et al<sup>1</sup> that the influence of the cantilever can't

be neglected when microelectrodes are used. The attraction of the cantilever can be even higher than the attraction of the tip. This combined attraction of tip and cantilever makes the positioning of the force difficult. Many other distance definitions as  $z_3$  could be used, as shown in figure 9-1 (a).

To avoid this positioning problem, to measure the influence of the cantilever and to show that it is possible to use only the cantilever for the force measurements, we made measurements with a Si-cantilever with a  $2\ \mu\text{m}$  diameter  $\text{SiO}_2$  sphere glued at its end (Novascan Technologies Inc., Ames, USA). The real spring constant of the cantilever is  $k = 6.41\ \text{N/m}$ . It is determined by the supplier using the Cleveland method<sup>2</sup>. The attached  $\text{SiO}_2$  sphere acts only as a spacer to the electrode surface, because the attraction of dielectrics in an inhomogeneous electrostatic field is several orders of magnitude smaller compared to metals or doped semiconductors<sup>3-6</sup>. The acting forces are, therefore, dominated by the doped silicon cantilever and not by the sphere. All distance values are, therefore, related to the cantilever's front edge to sample distance ( $z_{\text{Sp}}$  in figure 9-1 (b)).

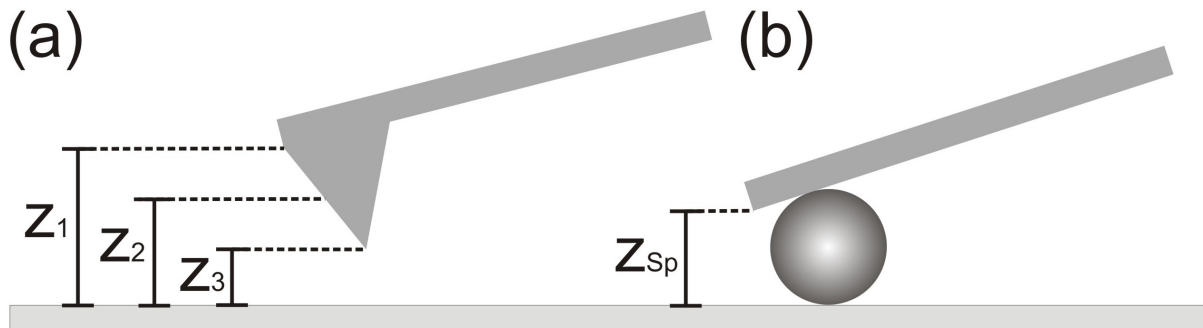


*Figure 9-1: (a) distances from surface, which are possible to take for the distance of the measured force from the surface, above microelectrodes. (b) A cantilever with  $\text{SiO}_2$  sphere avoids this problem. One takes as distance from the surface the distance between cantilever front edge and sample  $z_{\text{Sp}}$ .*

Figure 9-2 shows vertical force field measurements performed on  $10\ \mu\text{m}$  pitch interdigitated electrodes. The force field is measured at 0 %rh using the new measurement method as presented above. The cantilever and one of the two interdigitated electrodes are grounded during the measurement. On the

second electrode a potential of +25 V is applied. An equidistant grid having an interval of 2  $\mu\text{m}$  is placed on the 50 x 50  $\mu\text{m}^2$  scan field. This results in a 3 dimensional matrix. A horizontal cross-section through the vertical force field matrix at  $z = 2200$  nm is shown in figure 9-2 (b).

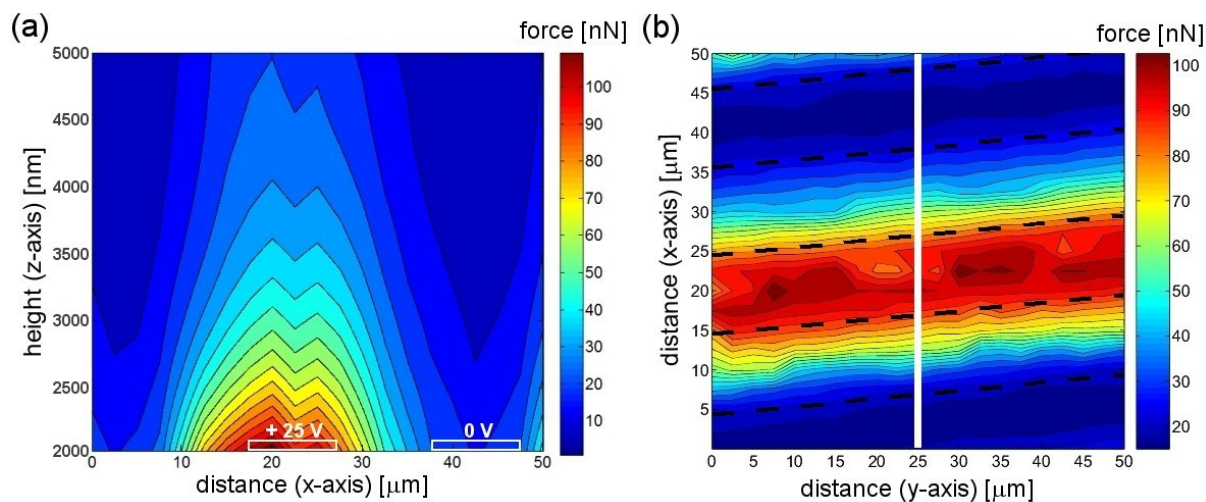


*Figure 9-2: Measured vertical force field of 10  $\mu\text{m}$  electrodes, obtained with a grounded cantilever with a  $\text{SiO}_2$  sphere and with 0 V and +25 V applied on the electrodes, alternately.*

At this distance from the surface the maximum electrostatic attraction force is 100 nN. A vertical cut, schematically indicated by a white line in figure 9-2 (b), through the vertical force field matrix at  $y = 25$   $\mu\text{m}$  is shown together with the approximate position of the electrodes (indicated by black dotted lines) in figure 9-2 (a). The force field extending several micrometers from the surface, has its minimum above the electrodes of identical potential and its maximum above the electrodes at +25 V.

We measured, as well, the force field for several voltages. The horizontal cross-section through the obtained vertical force field matrix at  $z = 2200$  nm is shown in figure 9-3. We can easily observe the development of the force field with voltage in the area. These results show that it is possible to get very good EFM measurements on microelectrodes using a cantilever with a  $\text{SiO}_2$  sphere as spacer.

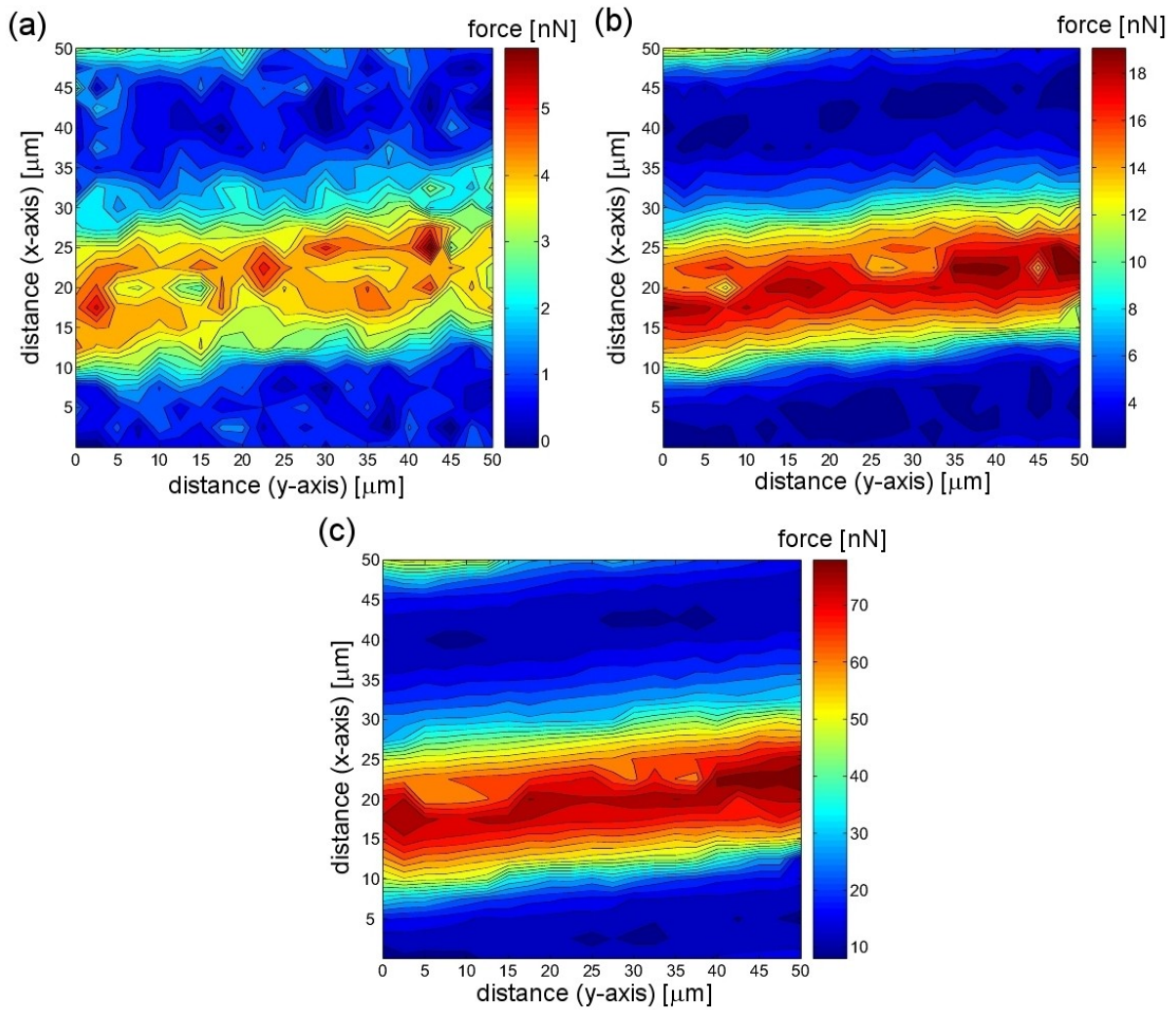
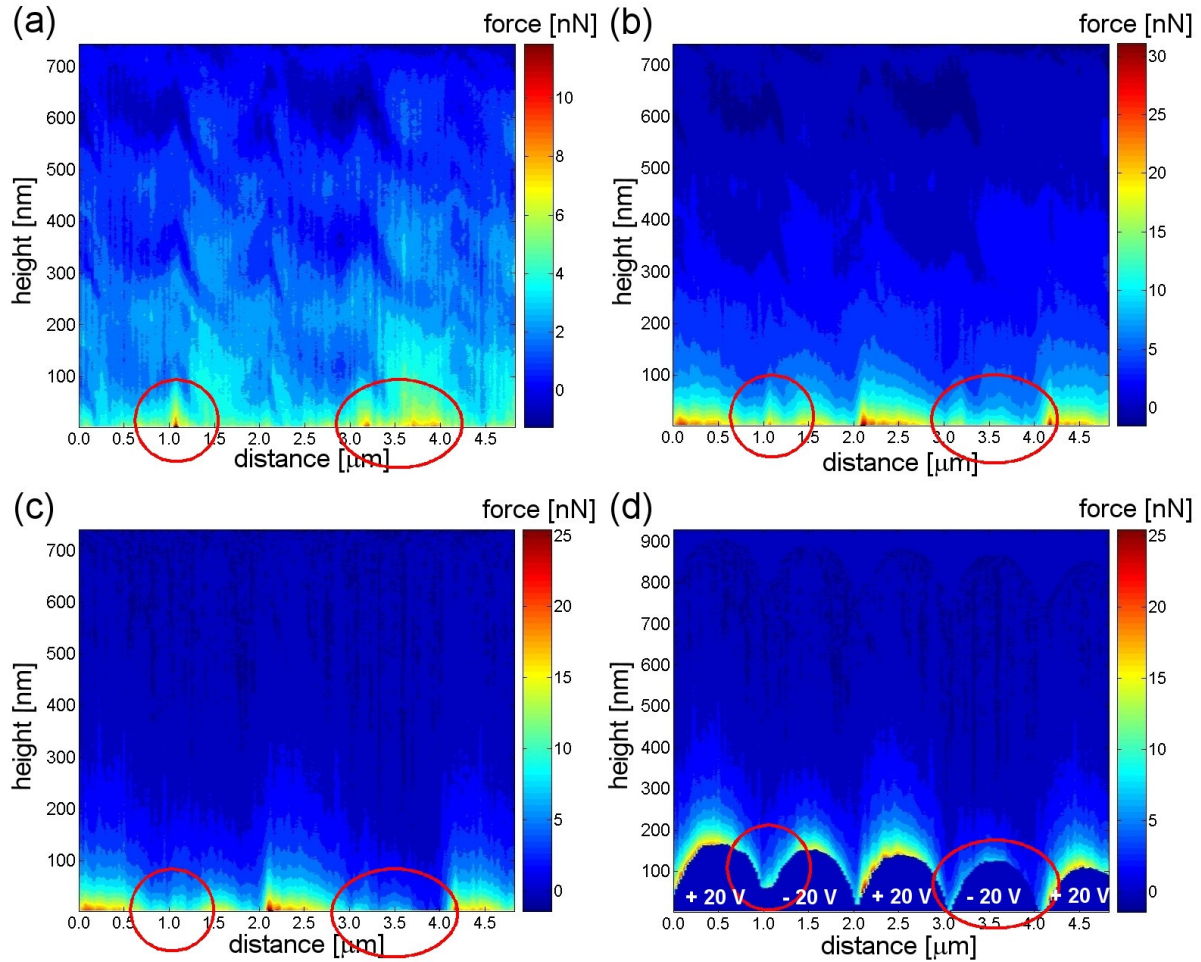


Figure 9-3: Measured vertical force field of 10  $\mu\text{m}$  electrodes, obtained with a grounded cantilever with a  $\text{SiO}_2$  sphere and with 0 Volt and (a) + 5 V / (b) + 10 V / (c) + 20 V applied on the electrodes, alternately.

## 9.2) Charge Injection

A typical problem for nanoelectrodes is the work function depended injection of charges into the oxide between the electrodes. Due to high electrostatic fields between the electrodes charge injection into the oxide can occur even at low voltages. Figure 9-4 shows one EFM measurement of 500 nm pitch interdigitated electrodes performed with our new EFM method. As mentioned, we perform two FDC measurements (with and without applied voltage) and a topographical measurement simultaneously.

Figure 9-4 (a) to (d) shows these measurements separately and enable one to observe two kinds of charge injection cases:



*Figure 9-4: Vertical force field of 500 nm electrodes, obtained with (a) no voltage applied on the electrodes; (b)  $\pm 20$  V applied alternately; (c) difference of (a) and (b); (d) difference of (a) and (b) combined with topographical information.*

(a) shows the resulting force field when no voltage is applied on the electrodes. The two red circles mark two places with charging. The left one is between the electrodes, the right one on top of one electrode; (b) shows the resulting force field when  $\pm 20$  V are applied on the electrodes, alternately. The in (a) observed charges influence clearly the force field. The injected charges shield a part of the electrical field, this reduces the measured forces. The new EFM method presented in chapter 6, subtracts the force field without

voltage from the one with voltage to exclude other forces and, as well, other electrostatic forces. The results of this subtraction is shown in (c). Due to the subtraction, the charging and shielding effect the force field in the charged areas, is almost vanished. (d) finally includes also the topography of the electrode array. The information given by the 4 figures, obtained in one single scan enables the detection and investigation of charge injection in nanostructures. This opens new possibilities for research and development of new semiconductor chips.

However, two open questions are still remaining:

1. Why do we have charge injection in-between and on top of our electrodes?

Charge injection due high electric fields between nanostructures, like our interdigitated electrodes with small pitch, is well known and described in literature<sup>7</sup>. The on the work functions of the materials dependent effect is even used for new memory applications<sup>8</sup>.

The charge injection on top of the electrodes results of the touching tip. The touching tip represents the top electrode of a capacitor, which is separated by a thin oxide layer (usually only 50 nm) from the counter electrode that is a electrode of the electrode array. We simply “wrote” these charges into the oxide, during a previous scan. Figure 9-4(a), however, shows that only two electrodes are charged. This suggest that we have only one for charging favourable configuration of material work functions. The work function of Ti (3.9 eV) is lower than the one of Pt (5.7 eV), therefore it is easier for the electrons to leave the Ti of the electrodes as the Pt of the tip. Hence, the charging likely occurs only on the negative electrode. However, due to the humid environment charges written with the Pt-tip on the SiO<sub>2</sub> surface will be fast discharged. Therefore, more detailed investigations would be needed to clarify this question.

Charge injection can be partly avoided by increasing the oxide



thickness, which changes the “capacitor” properties. However, the charge injection can be used to study easily charge injection into different materials.

2. How long do these charges stay in the oxide and how can these charges be removed?

Concerning the lifetime of the injected charges and their removal no clear conclusions could be drawn from our experiments. The lifetime of the charges can be several days, if the charges are written at low relative humidity and afterwards stored at higher relative humidity. However, this fluctuated a lot.

The removing of the charges remains challenging. We investigated several discharging methods, but only one method successfully removed sometimes the charges. The method is based on the application of an AC signal, which must have a frequency of about 100 kHz and a amplitude similar to the before applied DC voltage. The amplitude was reduced in several steps within 1 hour to 0 V. After this procedure, the charges were often removed.

### **9.3) Practical Advices for Nanoelectrode Handling**

Finally, we want to give a few practical advices on how to avoid electrical destruction of the nanoelectrodes? In our experience there exist three main causes for destruction:

1. Electrical shorts that are made during the fabrication, which lead to a breakdown at low voltages.

This can be avoided, most of the time, by SEM inspection. However, one has to take care that the SEM dose no carbon deposition during observation, which could lead again to electrical shorts.

2. The second cause is characterized by a burning through of the electrodes during the measurement. This usually happens when the oxide has a poor quality or is simply too thin. The tip touches the oxide above the first electrode, a high current flows between tip and electrode causing the electrode to melt.

This can be avoided by measuring the oxide quality and performing breakdown voltage calculations.

3. The third cause are barely visible damages created during the deposition of the oxide. The electrodes are damaged due to side effects (e.g. higher  $\text{Ga}^+$  implantation during FIB) or poor  $\text{SiO}_2$  sputtering. Often the electrode looks fine and the electrical properties are good as well. However, there exist several defects, which will lead to a burn through as soon as the tip comes close to it.

There exist badly no possibility for avoiding this kind of problem.

Figure 9-5 shows AFM contact scans of two damaged electrodes as examples. Electrode (a) is completely damaged, whereas electrode (b) has only two unconnected fingers.

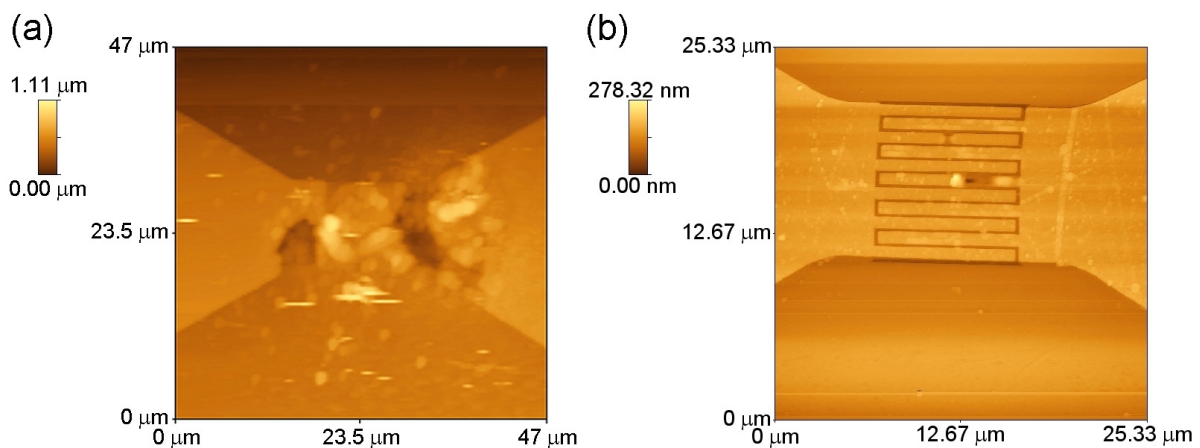


*Figure 9-5: AFM scans of damaged electrodes.*



## 9.4) Bibliography of Chapter 9

1. Sacha, G.M. and J.J. Saenz, *Cantilever effects on electrostatic force gradient microscopy*. Applied Physics Letters, 2004. **85**(13): p. 2610-2612.
2. Cleveland, J.P., S. Manne, et al., *A Nondestructive Method for Determining the Spring Constant of Cantilevers for Scanning Force Microscopy*. Review of Scientific Instruments, 1993. **64**(2): p. 403-405.
3. Frohe, H., *Elektrische und magnetische Felder*. 1994: Teubner Verlag. 482.
4. Hudlet, S., M.S. Jean, et al., *Electrostatic forces between metallic tip and semiconductor surfaces*. Journal of Applied Physics, 1995. **77**(7): p. 3308-3314.
5. Hudlet, S., M. Saint Jean, et al., *Evaluation of the capacitive force between an atomic force microscopy tip and a metallic surface*. The European Physical Journal B - Condensed Matter and Complex Systems, 1998. **2**(1): p. 5-10.
6. Kopanski, J.J., J.F. Marchiando, et al., *Scanning capacitance microscopy measurements and modeling: Progress towards dopant profiling of silicon*. Journal of Vacuum Science & Technology B, 1996. **14**(1): p. 242-247.
7. Yamada, K., S. Yoshii, et al., *Effects of dot density and dot size on charge injection characteristics in nanodot array produced by protein supramolecules*. Japanese Journal of Applied Physics Part 1-Regular Papers Brief Communications & Review Papers, 2007. **46**(11): p. 7549-7553.
8. Kohno, A., H. Murakami, et al., *Memory operation of silicon quantum-dot floating-gate metal-oxide-semiconductor field-effect transistors*. Japanese Journal of Applied Physics Part 2-Letters, 2001. **40**(7B): p. L721-L723.



## Micro- and Nanogripping

In this chapter we concentrate on the application of the fabricated structures, presented methods and the knowledge gained in the last chapters for micro- and nano-gripping. We will not give a general overview nor a detailed introduction in micro- and nano-gripping. This can be found elsewhere<sup>1</sup>. Here we will concentrate on the principle of micro- and nano-gripping with electrodes and some possible improvements.

### 10.1) Introduction

In micro- and nanogripping the balance between attraction (snap-in) and adhesion (snap-out) forces is very important. This balance determines if an object can be picked at one place and released at another place. For this “pick and place” operation the forces between gripper and object have to be controlled. One can use, for example, interdigitated electrodes to vary the electrostatic force on the gripper, as shown in figure 10-1. On the left side of figure 10-1 the picking-up of a sphere is shown. The adhesion force at the gripper-sphere interface must be higher than the adhesion force at the substrate-sphere interface. The middle part shows the transfer of the sphere. On the right side the release is shown. The force at the substrate-sphere interface has to be higher than at the gripper-sphere interface. Hence, the ideal micro- and nano-gripper has the following properties:

- The force at the gripper-sphere interface without applied voltage must be as low as possible.
- The force at the gripper-sphere interface with applied voltages must be as high as possible.

The bigger this difference the better “pick and place” operations can be performed on different substrates and in different environments.

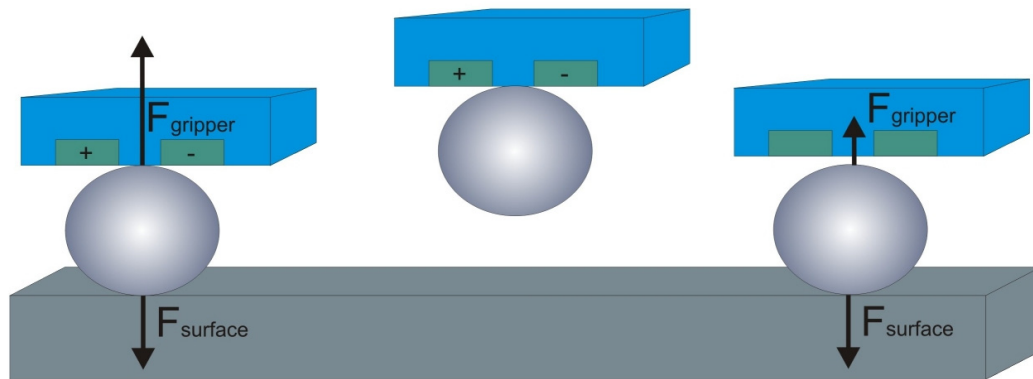


*Figure 10-1: Principle of electrostatic microgripping. A sphere is picked up on the left side, transferred and then released on the right side. The forces during the manipulation are shown schematically.*

With electrostatic gripping, the successful manipulation of conductive<sup>2</sup> and non-conductive objects<sup>3</sup> has been shown. The high influence of surface roughness<sup>4</sup> on the adhesion force, and with it on gripping, is presented. Other important effects, such as the variation of the adhesion force with humidity<sup>5</sup> have been studied for particle systems, but never in connection with electrostatic microgripping. Both effects, roughness and humidity, are studied in the following sub chapters for a specific system.

## 10.2) Tests for Electrostatic Microgripping

In order, to determine the best conditions for our pick and place studies we performed several experiments. As seen in the previous chapters the electrostatic field of the nanoelectrodes does not exceed the first 150 nm (figure 9-3). Due to this small interaction volume (surface to maximal extension of the electric field) one has to position the gripper very accurately on the gripping object, in order to pick it up. It is easier to use interdigitated electrodes with 1  $\mu\text{m}$  pitch, which have a much bigger interaction volume. In

addition, the electrodes are much easier to fabricate and bigger pitches allow one to apply higher voltages, which enables one to apply higher forces and perform more tests.

To know how far the electrostatic force field extends, we measured it as described in chapter 6, but without topographical measurement (figure 10-2).

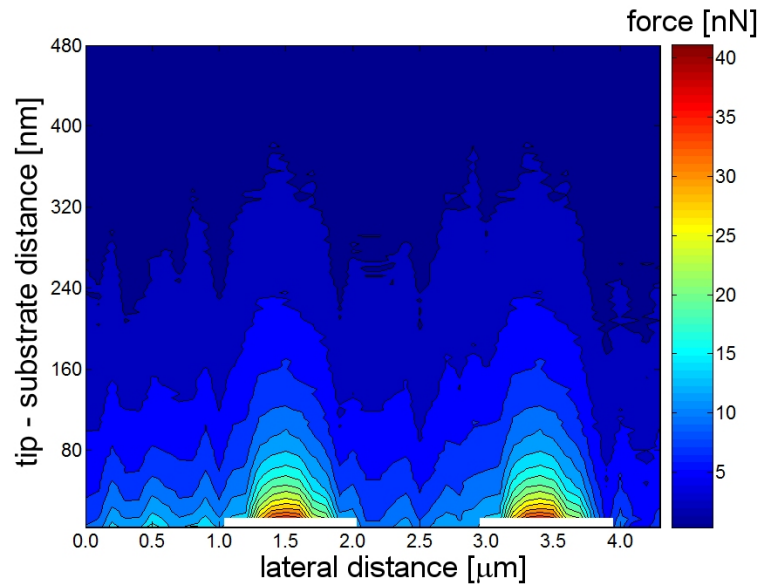


*Figure 10-2: Vertical electrostatic force field of 1  $\mu\text{m}$  pitch electrodes. Measured with  $\pm 20$  V applied alternately on the electrodes (white rectangles), and a grounded cantilever with tip (about 350 nm tip radius).*

With  $\pm 20$  V applied alternately, the electrostatic force field of the 1  $\mu\text{m}$  pitch interdigitated electrodes reaches about 2.5 times as far as the one of the 500 nm pitch electrodes. This distance and the applied force will increase with the applied voltage. To estimate the maximal voltage we can theoretically apply between the electrodes we assumed: The electrodes are fully buried in  $\text{SiO}_2$  with a breakdown voltage of 10 MV/cm. With these assumptions we calculated the maximal voltage to be 1000 V. However, this value will never be reached, because our electrodes are not fully buried in  $\text{SiO}_2$ . Measurements have show that the maximal potential difference that can safely be applied is about 130 V.

Another important parameter for the adhesion force is the roughness of the electrode area. The adhesion on rough surfaces is much lower than on flat surfaces. To determine the roughness of the electrodes the topography of the electrodes was measured using an AFM contact scan (figure 10-3 (a)). A line scan taken at the position indicated in figure 10-3 (a) and presented in (b) reveals that 38 % of the electrode area are below the electrodes. This means that the contact area between the electrode and the gripping object will be about 38 % smaller than on a flat surface, which corresponds to roughness values of:  $R_a = 49.68$ ,  $RMS = 57.00$ .

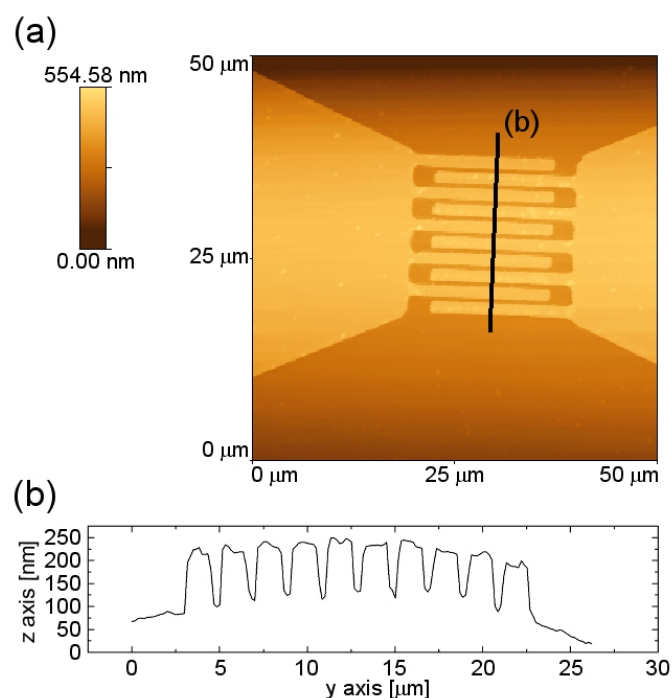


*Figure 10-3: Contact AFM scan (a) of 1  $\mu\text{m}$  pitch electrodes. A line scan (b) is taken on the line indicated in (a).*

After the determination of the force field and roughness some preliminary gripping tests are performed using a model system. Our model system consists of 4 samples and a Si cantilever with a  $\text{SiO}_2$  sphere of 10  $\mu\text{m}$  diameter, which is coated with a 130 nm thick Ti/Pt layer (see chapter 4.2). The 4 samples are two 1  $\mu\text{m}$  pitch interdigitated electrodes and two planar Si wafer chips. All

samples are O<sub>2</sub> plasma (50 W, 15 min.) treated prior to every set of measurements. Two samples (one of each sort) are vapour coated for 30 min. with a perfluoroalkylsilane layer (hydrophobic layer) (PFS)<sup>6</sup>. The other two samples (DOX) are stored during this time in a box under N<sub>2</sub> atmosphere. Afterwards, all samples are placed in the environmental box with the AFM (chapter 3) and the box is flushed for 12 h with a gas composition with appropriate relative humidity. The particular gas compositions were: N<sub>2</sub> atmosphere (0 %rh) and N<sub>2</sub> / Air mixtures resulting in 30 %rh and 60 %rh. We performed 15 FDCs on all samples at two different positions. The attraction and adhesion force of each of the 30 measurements is determined and the results are averaged. Figure 10-4 shows the results of the measurements on the Si-chips.

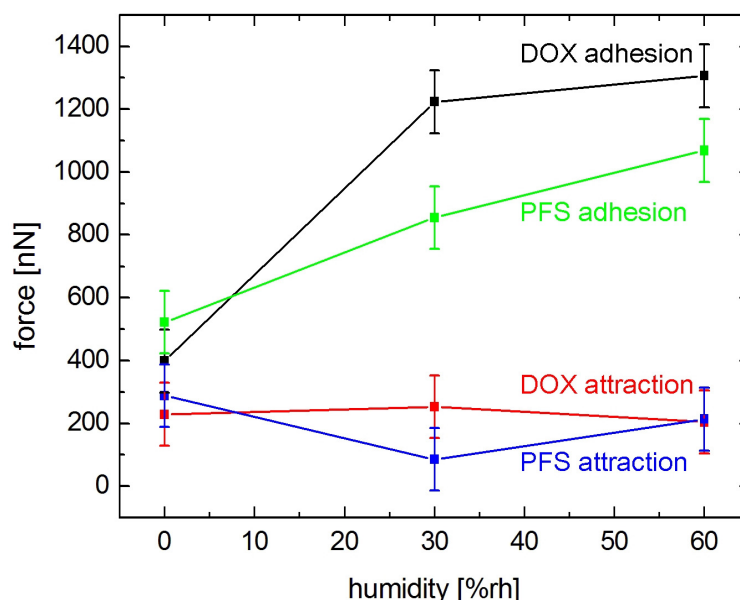


*Figure 10-4: Attraction and adhesion forces on a flat Si-wafer with and without PFS coating, at different humidities. The PFS coating decreases the adhesion force at 30 %rh and 60 %rh, but has no influence on the attraction force and the adhesion force at 0 %rh.*

The attraction force on the Si-chips is (in this scale) about constant with changing humidity. The adhesion force on the DOX samples increases rapidly ( $\Delta F_{0-30\%rh} \approx 800\text{nN}$ ) with humidity until 30 %rh and increases then more slowly

( $\Delta F_{30-60\%rh} \approx 200\text{nN}$ ) until 60 %rh, which conforms to the literature<sup>11</sup>. The adhesion force on the PFS sample increases constantly with the humidity until 60 %rh and is for 30 %rh and 60 %rh below the one of the DOX sample.

The silane layer(PFS) is a hydrophobic coating. This layer decreases the capillary force. The capillary force is a strong adhesion force that results from the surface tension of a water layer. This means that the sphere needs to be in contact with the sample surface and one needs to have a water layer on either the sample or the sphere or on both. Therefore, the contribution of the capillary force to the adhesion force is negligible for 0 %rh and the attraction force, but contributes important to the adhesion force at 30 %rh and 60 %rh. This is as well what is shown in figure 10-4. At 30 %rh and 60 %rh the adhesion force is reduced due to the PFS coating by about 400 and 250 nN, respectively. This corresponds to 1/6 to 1/3 of the total force.

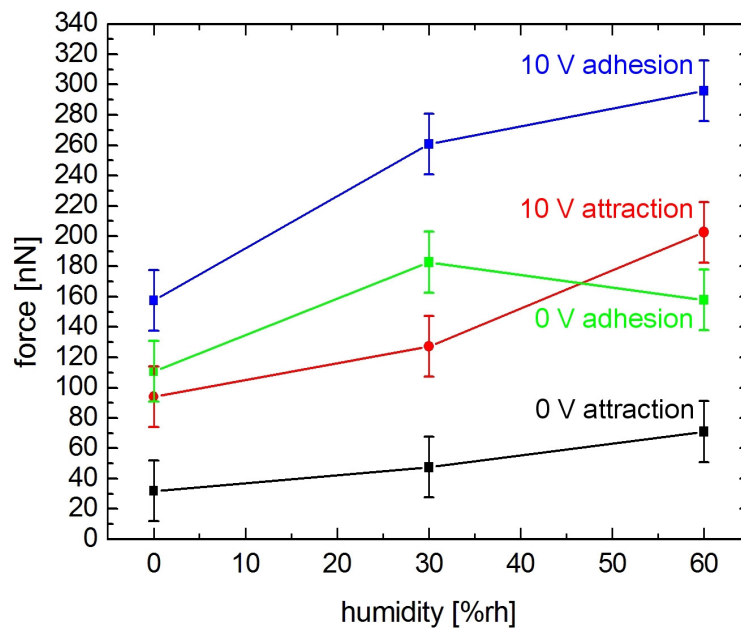


*Figure 10-5: Attraction and adhesion forces on 1  $\mu\text{m}$  pitch electrodes, embedded in  $\text{SiO}_2$ . The forces are measured without and with  $\pm 10\text{ V}$  applied alternately, at different humidities.*

Figure 10-5 and figure 10-6 show the changing of the attraction and adhesion force with humidity and voltage on the not coated (DOX) and coated (PFS)



electrodes.

The attraction and adhesion forces on the electrodes are without any applied voltage about 10 times smaller than on the flat Si-chips (figure 10-4). This results from the previously mentioned roughness of the electrodes and the sphere diameter. A sphere of 10  $\mu\text{m}$  diameter does not touch the whole electrode area. Depending on the position of the sphere on the electrodes the sphere touches only on a few points on the electrode. This explains the large decrease of the adhesion force.

Due to applying  $\pm 10$  V alternately on the interdigitated electrodes, the attraction force increases in the order of 60, 80 and 120 nN for 0 %rh, 30 %rh and 60 %rh, respectively. The adhesion force increases by about 50, 80 and 140 nN for 0 %rh, 30 %rh and 60 %rh, respectively. This corresponds to an average increase of 2.5 times of the attraction force and 1.7 times of the adhesion force. The force to pick up the sphere with the gripper would be therefore 2.5 higher, in comparisons with a surface of the same roughness. However, to pick up the sphere from a flat substrate would be impossible, because the adhesion force on the flat substrate is 2 to 10 times higher (figure 10-4) than the adhesion force on the electrodes with  $\pm 10$  V applied. If we assume a quadratic increase similar to the one for the electrostatic force in figure 8-10 for the adhesion force with an applied voltage, we would need to apply 35 V to be able to pick up the sphere from a flat surface at 0 %rh.

If we coat the electrodes with the hydrophobic coating, the adhesion on the electrodes is further reduced at 30 %rh and 60 %rh, by about 60 nN. (figure 10-6). Hence, a hydrophobic coating on the electrodes is not advantageous, for the presented case.

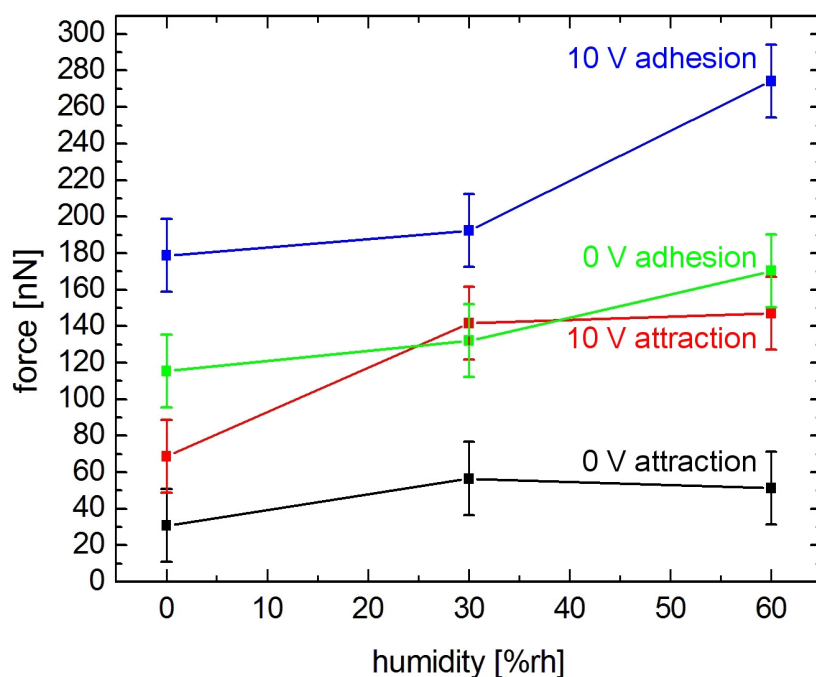


Figure 10-6: Attraction and adhesion force on  $1\mu\text{m}$  pitch electrodes, embedded in  $\text{SiO}_2$  and PFS coated. The forces are measured with and without  $\pm 10\text{ V}$  applied alternately. The humidity is varied between 0 and 60 %rh.

### 10.3) Electrostatic Gripping Measurements

After the pre-tests described in chapter 10.2 we performed pick and place studies in collaboration with the LSRO2 group at EPFL<sup>7-9</sup>. We used the same interdigitated microelectrodes presented as in chapter 10.2. The design of the microelectrodes allows mounting in a special holder (figure 10-7 (a)). It contains, as well, alignment marks, which enable the automatic recognition of the position of the interdigitated electrodes (figure 10-7 (b)).

Metallic spheres are not commercially available, therefore, we used  $50\mu\text{m}$  polystyrene beads instead. The main problem with polystyrene bead is that they easily charge during contact with other dielectric surfaces. In addition, the attraction of dielectrics in electrostatic fields is much lower than that of metals. Therefore, we expect to grip the PS spheres at higher voltages than calculated for the metal coated spheres and a strong variation of the results

due to charging effects. To avoid charging the tests were carried out at about 30 %rh on (rough) microscope glass slides, which are coated with our hydrophobic PFS coating.

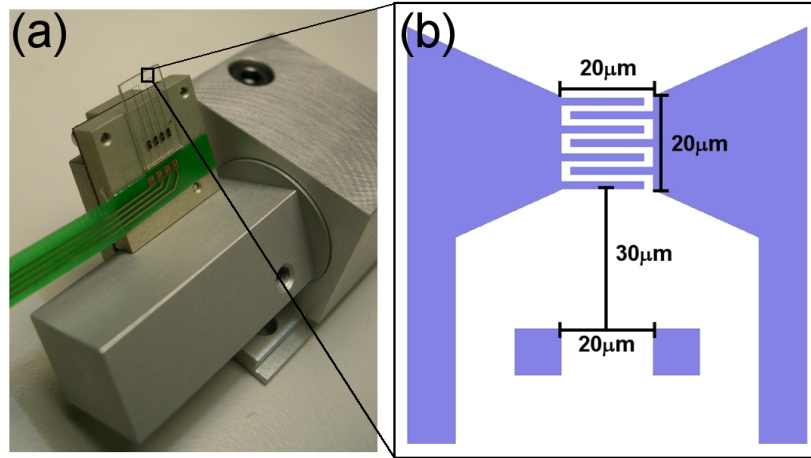


*Figure 10-7: Mounted electrostatic gripper (a) and its design(b). The design allows an automatic recognition of the interdigitated electrode position.*

Seventeen manipulations (pick and place) per volt span are preformed and the success rate calculated using:

$$success\ rate = \left( \frac{number\ of\ successful\ manipulations}{total\ number\ of\ manipulations} \right) * 100 \quad Eq. 10-1$$

The results of the tests are shown in figure 10-8.

We achieved the highest success rate with applied potentials between 50 and 60 V. Potentials between 70 and 90 V delivered, as well, good results, but we observed a charging increase for voltages above 70 V. We also observed releasing problems on the microscope glass slides, in this case, we tried to release the sphere on a second PS sphere lying on the glass slide. This usually worked well.

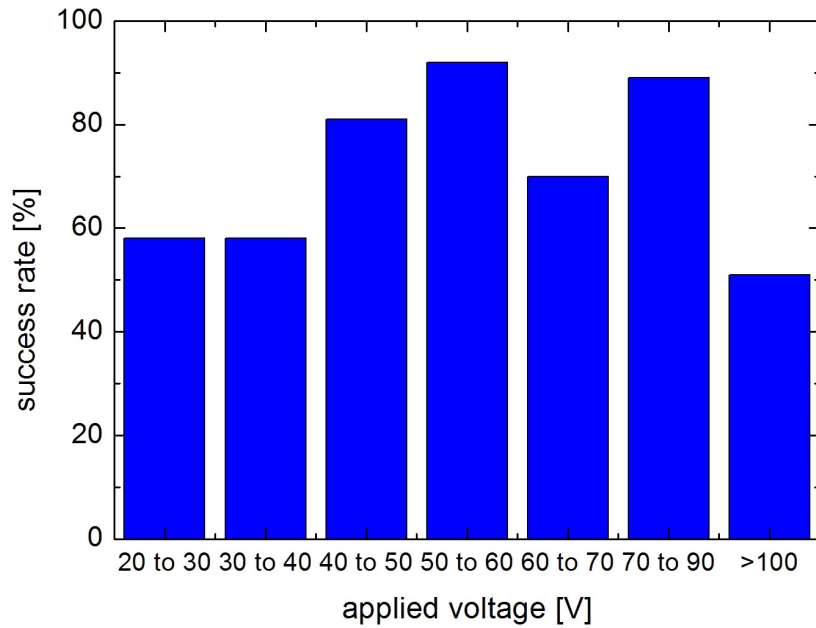


*Figure 10-8: Electrostatic gripping test results. The tests were carried out with the electrostatic gripper setup shown in figure 10-7 and 50  $\mu\text{m}$  polystyrene beads as gripping objects.*

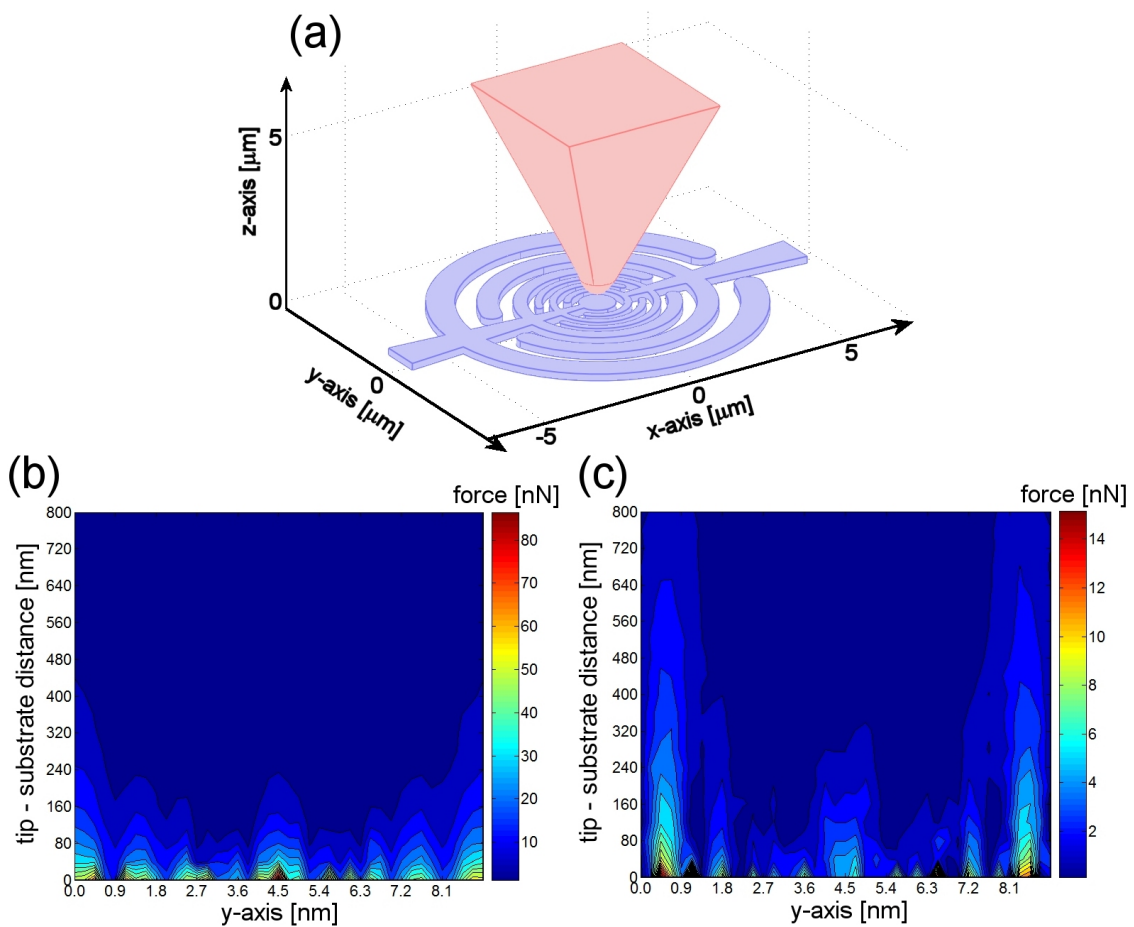
#### **10.4) Proposed Improvements for Electrostatic Gripping**

Figure 10-5 and 10-6 show that the difference between the attraction and adhesion force with no and with applied potentials increases with humidity. In chapter 8.5 we presented the reason for this behaviour. The dielectric constant of air increases with increasing humidity, thus, influencing the gripping force dramatically. The force on the electrode surface increases and the range of the electrostatic force decreases. Depending on the material and shape of the object this can either decrease or increase the applied force on the object. As well side effects like charging or discharging are influenced. This should systematically be investigated in a further work using the presented methods as shown in chapter 9-2.

We observed during the measurements that a better control of the placement of the particle is needed. To improve the control we designed an electrode, with electrostatic force centering effect (Figure 10-9 (a)). The

automatic centering effect allows the positioning of smaller parts with much higher accuracy. Figure 10-9 (b/c) presents numerical simulations as described in chapter 7 applied on the new design.

(b) Shows the vertical force field (z-direction). The vertical force field decreases rapidly from the outer ring to the inner ring. Due to this force gradient all attracted parts will be guided to the inner ring. (c) Confirms this effect, because it shows the force field parallel (y-direction) to the electrodes. The parallel force of the electrodes decreases as well from the outer to the inner ring.



*Figure 10-9: Special designed electrodes for electrostatic gripping. The design is shown in (a). The numerical simulated (b) vertical (z-force) and (c) parallel (y-force) electrostatic force field shows a centering effect for this design.*

As already mentioned, a problem of electrostatic gripping is its sensitivity to charged dielectric objects. This could be avoided, if another gripper principle is used. To do this one has to change the whole gripping setup. In addition, other gripper principles have other disadvantages (too high gripping force, introduces liquids, rapid temperature changes are needed...). It would be much more convenient, to use the same setup and to add only an active coating on the gripper. This coating changes for example its surface energy, to enable gripping by changing the capillary force.

To do this one needs a chemical layer, which can be influenced by an electrical field. Furthermore, the electrostatic field has to be confined in this polymer layer. Our force field measurements in the previous chapters have shown that this is possible by using electrodes of 1  $\mu\text{m}$  pitch and below. After some discussion with Prof. Hilborn (Uppsala University) we identified one polymer, which can be influenced by the E-field. A modified Polytrimethylenecarbonate (=PTMC)<sup>10</sup> with protonated amino-head groups (figure 10-10) and  $\text{Cl}^-$  counter anions should be sensitive enough to the electrostatic field to enable such changes in surface energy. The protonated amino-head groups of the polymer should be in a humid environment on the surface of a layer of this material. Such a layer is hydrophilic. In presence of the E-field the positive charged end groups should be pulled into the surface and the hydrophobic backbone of the polymer should remain at the surface.

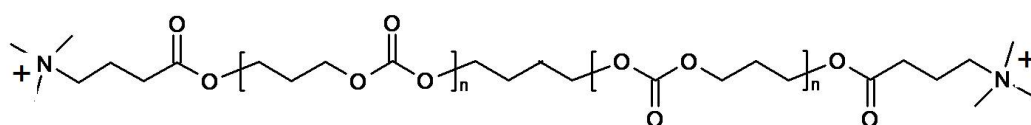


*Figure 10-10: Modified Polytrimethylenecarbonate (=PTMC)<sup>10</sup> with positive amino head groups. (counter ion =  $\text{Cl}^-$ )*

To prove this behaviour we spin coated a layer of PTMC on 5  $\mu\text{m}$  pitch electrodes (chapter 2.1) and measured the contact angle change of a water droplet with applied voltage on the electrodes. The results of this measurement are presented in figure 10-11. The contact angle of the water

droplet increases with applied voltage from 27 to 65°. To exclude other changes of the surface during the measurement we performed identical measurements on another place of the electrodes, without applied voltage. These measurements are shown as well in figure 10-11 (red line). The contact angle decreases slowly with the number of experiments if no voltage is applied. Hence, one can exclude surface changes as a cause for the increasing contact angle. On the other hand, an influence of the electric field on the water droplet cannot be excluded. However, a water droplet in an electric field reduces its contact angle, because the water dipoles are attracted by the electric field. This led to the conclusion that our polymer changes its surface energy only due to the applied electrostatic field. However, we were not able to change the contact angle back to its initial value. Therefore, further research needs to be performed on such surfaces in order to enable gripper applications.

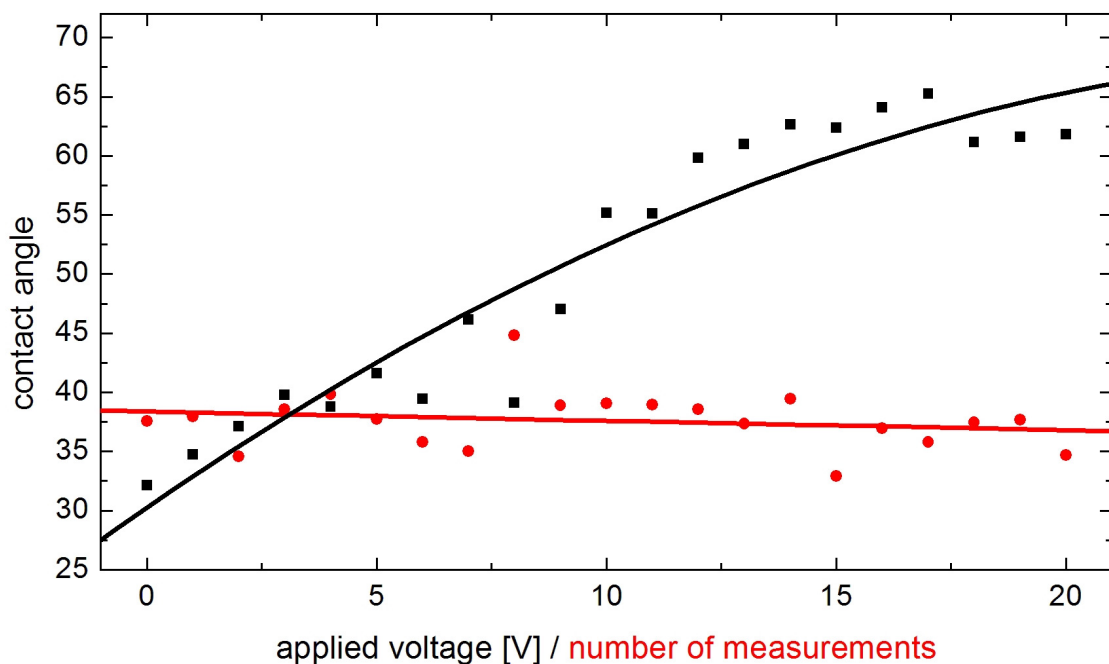


*Figure 10-11: Water contact angle measurements on modified PTMC. The contact angle change is measured with (black line and square dots) and without (red line and round dots) applied voltage on the underlining 5  $\mu\text{m}$  pitch electrodes.*

## 10.5) Bibliography of Chapter 10

1. Lambert, P., *A Contribution to Microassembly: a Study of Capillary Forces as a gripping Principle*, in *Faculté des sciences appliquées*. 2004, Université Libre de Bruxelles: Bruxelles.
2. Enikov, E.T., L.L. Minkov, et al., *Microassembly experiments with transparent electrostatic gripper under optical and vision-based control*. *Ieee Transactions on Industrial Electronics*, 2005. **52**(4): p. 1005-1012.
3. Hesselbach, J., J. Wrege, et al., *Micro Handling Devices Supported by Electrostatic Forces*. *CIRP Annals - Manufacturing Technology*, 2007. **56**(1): p. 45-48.
4. Lhernould, M.S., A. Delchambre, et al., *Electrostatic forces in micromanipulations: Review of analytical models and simulations including roughness*. *Applied Surface Science*, 2007. **253**(14): p. 6203-6210.
5. Jones, R., H.M. Pollock, et al., *Inter-particle forces in cohesive powders studied by AFM: effects of relative humidity, particle size and wall adhesion*. *Powder Technology*, 2003. **132**(2-3): p. 196-210.
6. Hoffmann, P.W., M. Stelzle, et al., *Vapor Phase Self-Assembly of Fluorinated Monolayers on Silicon and Germanium Oxide*. 1997. p. 1877-1880.
7. Dafflon, M., B. Lorent, et al. *A micromanipulation setup for comparative tests of microgrippers*. in *International Symposium on Robotics*. 2006. München, Germany.
8. Dafflon, M., B. Lorent, et al. *Characterization of micro manipulation tasks operated with various controlled conditions by microtweezers*. in *5th International Workshop on MicroFactories (IWMF)*. 2006. Besançon, France.
9. Dafflon, M., B. Lorent, et al. *Characterization of an inertial micro gripper based on adhesion forces*. in *5th International Wordshop on MicroFactories (IWMF'06)*. 2006. Besançon, France.
10. Atthoff, B., F. Nederberg, et al., *Synthetic Biodegradable Ionomers that Engulf, Store, and Deliver Intact Proteins*. 2006. p. 2401-2406.
11. Opitz, A., *Nanotribologische Untersuchungen von ultradeunnen Wasserfilmen auf hydrophoben und hydrophilen Siliziumoberfleachen*, in *Mathematik und Naturwissenschaften*. 2003, Technische Universiteit Ilmenau: Ilmenau. p. 110.



## Conclusions and Perspectives

We tested in this thesis electron beam lithography, electron beam deposition, focused ion beam milling and focused ion beam gas assisted milling as methods for the fabrication of interdigitated nanoelectrodes. Gas assisted focused ion beam milling, as best method, was used for fabricating interdigitated nanoelectrodes with pitches down to 50 nm on fused silica and oxidized Si wafers, with a prestructured Ti layer on top. After SiO<sub>2</sub> coverage, the 50 nm pitch electrodes had a resistance of  $2 \pm 0.5 \text{ G}\Omega$ , the 200 and 500 nm pitch electrodes of about  $14.8 \pm 5 \text{ T}\Omega$ .

The vertical components of the electrostatic force fields above the 500 and 50 nm pitch interdigitated electrodes are measured using a new EFM method. This method is based on simple static force distance curves. It allows one to measure accurately, and simultaneously the topography, the vertical electrostatic force field, and the adhesion and attraction forces.

For these measurements we fabricated Pt coated cantilevers with tip radii between 100 and 600 nm. These tip radii close the gap between conventional tips with small tip radius ( $\approx 10 \text{ nm}$ ) and cantilevers with glued spheres ( $\geq 2 \text{ }\mu\text{m}$ ). It was shown that the tip radius ( $R$ ) of these tips depend linearly on the deposited thickness ( $T$ ) and follows in our case the equation:  $R = 0.542 * T + 13$ , where 13 is the real tip radius and the factor 0.542 results from the geometry of the tip and the deposition chamber.

The fabricated tips did not degrade during several thousand's of FDC measurements and are therefore much better than commercial available tips. These tips are a small but significant step forward for the EFM measurement community.

The spring constant of these Pt coated cantilevers with different tip radii is determined using a modified dimensional method and the dynamical method of Sader. This allows the accurate determination of the force.

A 3D numerical and an analytical model of the new EFM method were developed. The combination of measurements and theoretical calculations allowed us to study in more detail our method and EFM in general. We investigated the influence of small tip shape discrepancies and showed their big influence (up to 50 % force increase) on the measured or simulated electrical force fields. The position of the tip shape discrepancies on the other hand had no big influence, if they are within the E-field and not closer to the surface than the main tip.

We determined the resolution of the force field measurements and discovered that a pitch to tip radius ratio of 2 to 2.5 delivers a good resolution for all presented pitches. We have shown that this ratio is unfavorable for parallel topography measurements with good quality. Compromises between topographical and force measurement have to be made.

We investigated the influence of relative humidity changes on electrical force field measurements. The vertical electrostatic force increases significantly (up to 45 %) with increasing relative humidity, because the relative permittivity of the gas between tip and electrodes increases accordingly. Furthermore, a strong force increase at low distances to the surface is measured. We believe this increase is caused by the water film on the surface. The closer the tip comes to the surface the higher is the contribution of the water film to the relative permittivity between tip and electrodes. Similar to the relative permittivity increase with the relative humidity, as described before.

We have shown that the cantilever is not measurably attracted during our nanoelectrode measurements, whereas the attraction of the cantilever has to be taken into account for EFM measurements on microelectrodes. We used this effect for measuring the electrostatic field above 10  $\mu\text{m}$  pitch interdigitated electrodes using a cantilever with a glass sphere.

We have demonstrated that the new EFM method enables one to identify and characterize regions with trapped charges within electrical force fields. In parallel it is shown how charges can be written in oxides and consecutively measured. This allows one to study the trapping behavior of materials and opens new possibilities for research and development in semiconductor industry where trapped charges are used to store information.

The fabricated electrodes and the new EFM method were used to improve micro- and nano-gripping. The electrostatic force field above 1  $\mu\text{m}$  pitch interdigitated electrodes and the change of the adhesion force with humidity and applied potential was measured. The change of the adhesion force on flat Si-chips, without and with a hydrophobic chemical coating (perfluoroalkyl-layer) was measured, as well. According to these measurements the best conditions for the manipulation of a metallic sphere of 10  $\mu\text{m}$  diameter is at 0 %rh with a voltage of about 35 V applied on 1  $\mu\text{m}$  pitch interdigitated electrodes. Pick and place operations with a polystyrene (PS) sphere of 10  $\mu\text{m}$  diameter have shown that a voltage of about 60 V applied on the 1  $\mu\text{m}$  pitch interdigitated electrodes delivers the best results for dielectric spheres.

Moreover, a new electrode design for micro- and nano-gripping has been proposed and simulated. Objects gripped with the new design are automatically centered on these electrodes. This allows one to grip objects with higher position accuracy and smaller objects. The fabrication and implementation of the new gripper design will result in a significant step forward in micro- and nano-gripping. The centering effect of this new design could be measured with our new EFM method, for this, torsional deflection changes of the cantilever have to be measured. This possibility is already integrated in the AFM software written in this PhD.

A detailed study of the influence of the water film under different humidity and temperature conditions on the electrical force field could be very interesting for several applications. The humidity measurements indicate that it is possible to determine with the new EFM method, the thickness of the

water film on the surface due to its effect on the force field. This could be used to study the distribution of the water film on different surfaces.

The results of this work are also important for EFM measurements on future chips, potentially including nanowires and nanotubes. We showed that the measurement of very small structures can be done with a tips radius much bigger than the actual structure, if one is not interested in the real topography. This enables one to measure much smaller forces, and to have a much better signal to noise ratio.

## Appendix

### 12.1) SiO<sub>2</sub>

Silicon dioxide is used within this work for electrical insulation. In order to have a good control on the quality of the used oxides we tested the chemical composition of different silicon dioxides.

Three oxides are tested : Thermally grown silicon dioxide, reactive gas assisted sputtered silicon dioxide and evaporation of SiO in oxygen environment. The produced oxides were analysed by Auger spectroscopy (figure 12-1).

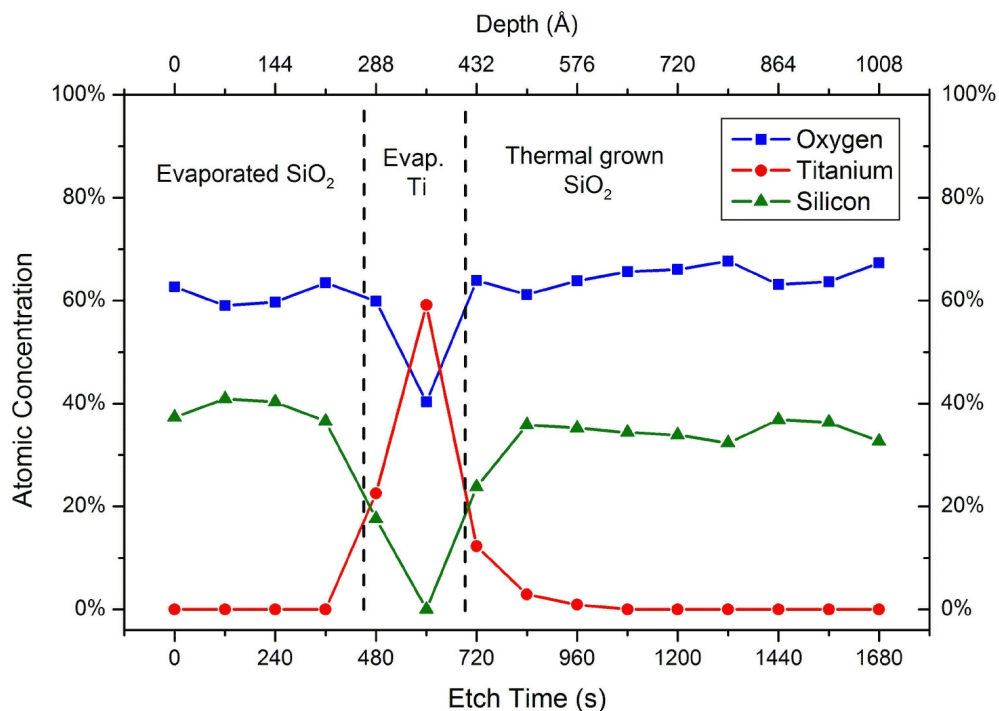


Figure 12-1: Auger spectroscopy measurement of a thermal oxidised silicon wafer with evaporated titanium and under O<sub>2</sub> pressure evaporated SiO on top.

The following table presents the Si to O ratios found by this fabrication methods:

	Si to O ratio
Thermal SiO <sub>2</sub>	1:1.91
Sputtered SiO <sub>2</sub>	1:1.89
Evaporated SiO <sub>2</sub>	1:1.68

The best oxides are the thermal and in O<sub>2</sub> environment sputtered SiO<sub>2</sub>.

## 12.2) Thermal Noise Method

We presented and applied in chapter 5 the method of Sader for the calibration of our cantilevers. We introduced as well the thermal noise method but did not use it, because it was never proven that this method delivers correct values for cantilevers with thick metal coating. In the following we want to give a small introduction to this important method for non coated cantilevers:

The thermal noise method (sometimes as well called thermal tune method) is based on the equipartition theorem of the thermodynamic theory<sup>1-9</sup>. The equipartition theorem states that for a generalized position or momentum coordinate (denoted here as  $X$ ), which stores energy according to  $E_x \propto X^2$ , the average energy stored in  $X$ ,  $E_x$  is given by:

$$\langle E_x \rangle = \frac{1}{2} k_B T \quad \text{Eq. 12-1}$$

where  $k_B$  is the Boltzmann's constant and  $T$  the absolute temperature in kelvin.

If one consider only small cantilever deflections, the force and deflection are linearly related, therefore, the energy stored in the deflection ( $d_c$ ) can be written accordingly as:

$$\langle E_x \rangle = \frac{1}{2} k \langle d_c^2 \rangle \quad \text{Eq. 12-2}$$

Equating equation 12-1 with equation 12-2 results in:

$$k = \frac{k_B T}{\langle d_c^2 \rangle} \quad \text{Eq. 12-3}$$

Thus measuring  $\langle d_c^2 \rangle$  (total power in thermal vibrations) and  $T$  allows theoretically to calculate the spring constant. However, in practice the situation is a bit more complicated.

It is theoretically possible to calculate  $\langle d_c^2 \rangle$  by integrating  $P_d$  (chapter 5.2) over all frequencies. In practice this is not possible because  $P_d$  contains as well background noise and for some cantilevers not all resonance frequencies are accessible or are hidden in the background noise.

Butt et al.<sup>2</sup> found a relationship between the power in the lowest resonance peak and the total power using a vibrational mode analysis and introduced a factor for compensation into equation 4-13:

$$k = 0.971 \frac{k_B T}{\langle d_1^2 \rangle} \quad \text{Eq. 12-4}$$

$\langle d_1^2 \rangle$  can be now easily obtained by integrating  $P_d$  over the first resonance peak (chapter 5.2).

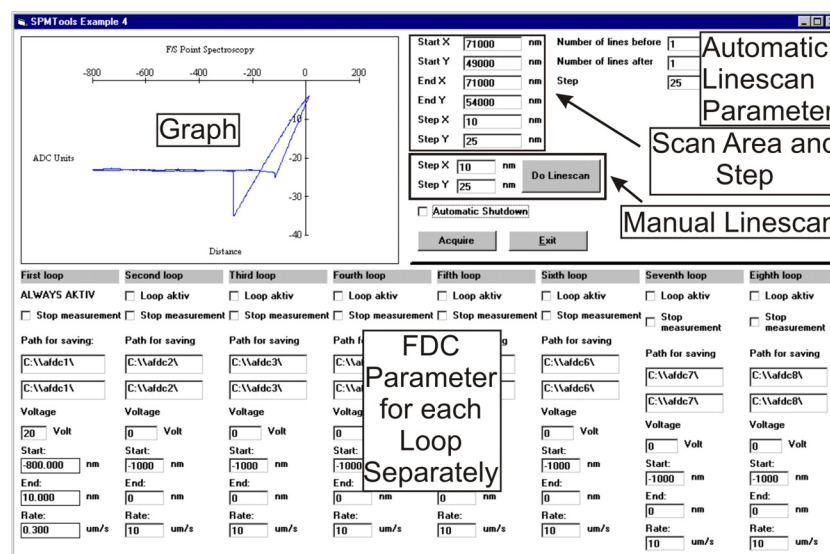
1. Burnham, N.A., X. Chen, et al., *Comparison of calibration methods for atomic-force microscopy cantilevers*. Nanotechnology, 2003. **14**(1): p. 1-6.
2. Butt, H.J. and M. Jaschke, *Calculation of thermal noise in atomic force microscopy*. Nanotechnology, 1995. **6**(1): p. 1-7.
3. Heim, L.O., M. Kappl, et al., *Tilt of Atomic Force Microscope Cantilevers: Effect on Spring Constant and Adhesion Measurements*. Langmuir, 2004. **20**(7): p. 2760-2764.
4. Hutter, J.L., *Comment on Tilt of Atomic Force Microscope Cantilevers: Effect on Spring Constant and Adhesion Measurements*. Langmuir, 2005. **21**(6): p. 2630-2632.

5. Hutter, J.L. and J. Bechhoefer, *Calibration of atomic-force microscope tips*. Review of Scientific Instruments, 1993. **64**(7): p. 1868-1873.
6. Levy, R. and M. Maaloum, *Measuring the spring constant of atomic force microscope cantilevers: thermal fluctuations and other methods*. Nanotechnology, 2002. **13**(1): p. 33-37.
7. Proksch, R., Sch, et al., *Finite optical spot size and position corrections in thermal spring constant calibration*. Nanotechnology, 2004. **15**(9): p. 1344-1350.
8. Schäffer, T.E., *Calculation of thermal noise in an atomic force microscope with a finite optical spot size*. Nanotechnology, 2005. **16**(6): p. 664-670.
9. Walters, D.A., J.P. Cleveland, et al., *Short cantilevers for atomic force microscopy*. Review of Scientific Instruments, 1996. **67**(10): p. 3583-3590.

## 12.3) AFM Software

### a.) FDC force field scan

The new EFM method is based mainly on a modification of the AFM software and data treatment. The user interface for the AFM software programmed in this thesis is the following:





The Visual Basic code important for the acquisition of the FDC curves and the topography with our AFM is the following:

```
Private Sub Acquire_Click()  
Dim zpiezo, zpiezo2 As Double  
Dim count As Long  
Dim fso, txtfile  
Dim i2 As Integer  
Dim Layer As Integer  
Dim pullback As Integer  
Dim linename, runtxt As String  
Dim runx, runy As Double  
Dim fso7, txtfile7  
Layer = 600  
pullback = -4000  
    Call vSetSpectParam(s, 0)  
    Acquire.Enabled = False  
    valstartx = Val(Textstartx.text)  
    valstarty = Val(Textstarty.text)  
    valendx = Val(Textendx.text)  
    valendy = Val(Textendy.text)  
    valstepx = Val(Textstep.text)  
    valstepy = Val(Textstep2.text)  
    movebool = False  
    specbool = False  
    s.iAvgPoint = 8  
    s.fDelaySample = 10  
    s.iLayers = Layer  
    s.fVzPullback = pullback  
    Call vSetSpectParam(s, 0)  
    count = 0  
    send Val(2), "Output OFF", stat%  
    send Val(2), "Apply P25V," & Text1.text & ",0.001", stat%  
    send Val(2), "Apply N25V,-" & Text1.text & ",0.001", stat%  
    For runx = valstartx To valendx  
        If (Check2.Value = 0) Then  
            runtxt = Format(Str(runx), "#####0")  
            linename2 = "lineactiv" + runtxt  
            filename7 = path.text + linename2  
            Set fso7 = CreateObject("Scripting.FileSystemObject")
```

```

Set txtfile7 = fso7.CreateTextFile(filename7, True)
End If
For runy = valstarty To valendy
If (Check2.Value = 0) Then
    movebool = bMoveToXY(runx, runy, 500, XYMOVE_DIST)
    For i = 1 To 2000
        Next i
    Call vGetPresentZvoltage(zpiezo)
    For i = 1 To 20000
        Next i
    send Val(2), "Output ON", stat%
    For i2 = 1 To 2
        For i = 1 To 20000000
            Next i
        Next i2
    specbool = bSampleSpectroscopy(IData(0), ipt(0), itypes(0), nHalf)
    For i = 1 To 20000
        Next i
    filename1 = path.text + "volt\alpha\" + Str(runx) + "_" + Str(runy) + ".txt"
    filename2 = path.text + "volt\r\" + Str(runx) + "_" + Str(runy) + ".txt"
    filename3 = path.text + "volt\old\" + Str(runx) + "_" + Str(runy) + ".txt"
    Call vDrawGraph
    send Val(2), "Output OFF", stat%
    For i2 = 1 To 3
        For i = 1 To 20000000
            Next i
        Next i2
    specbool = bSampleSpectroscopy(IData(0), ipt(0), itypes(0), nHalf)
    For i = 1 To 20000
        Next i
    filename1 = path2.text + "0\alpha\" + Str(runx) + "_" + Str(runy) + ".txt"
    filename2 = path2.text + "0\r\" + Str(runx) + "_" + Str(runy) + ".txt"
    filename3 = path2.text + "0\old\" + Str(runx) + "_" + Str(runy) + ".txt"
    Call vDrawGraph
    send Val(2), "Output OFF", stat%
    count = count + 1
    Call vGetPresentZvoltage(zpiezo2)
    xvaltxt = Format(Str(runx), "#####0.#####0")
    yvaltxt = Format(Str(runy), "#####0.#####0")
    zvaltxt = Format(Str(zpiezo), "#####0.#####0")
    zvaltxt2 = Format(Str(zpiezo2), "#####0.#####0")

```

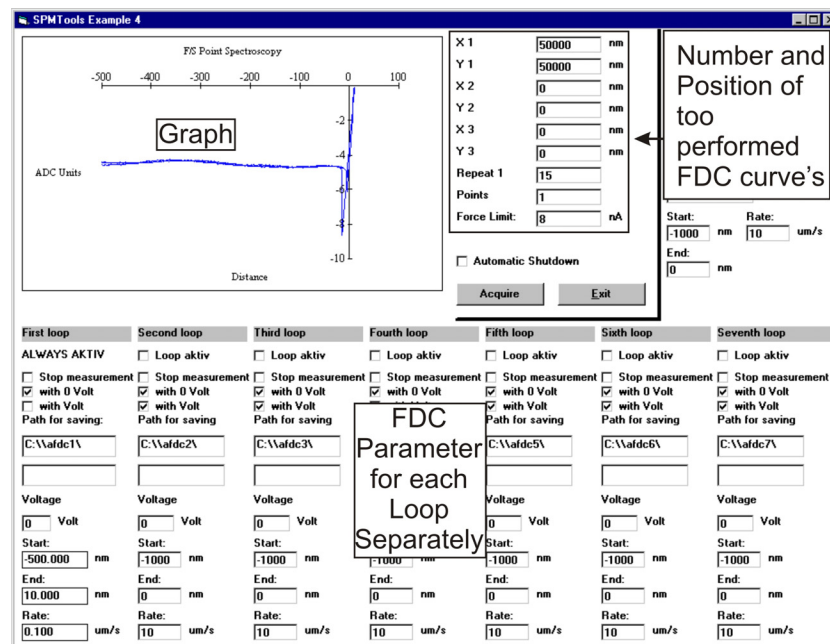
```

txtfile7.WriteLine (xvaltxt + ";" + yvaltxt + ";" + zvaltxt + ";" + zvaltxt2 + ";")
End If
runy = runy + valstepy - 1
Next runy
txtfile7.Close
runx = runx + valstepx - 1
Next runx

```

## b.) FDC point measurements

The FDC point measurements conducted for chapter 11 are performed with the following user interface:



and Visual Basic code:

```

Private Sub Acquire_Click()
Dim count As Long
Dim fso, txtfile
Dim i2 As Integer
    valx1 = Val(Textx1.Text)

```

```

valy1 = Val(Texty1.Text)
valx2 = Val(Textx2.Text)
valy2 = Val(Texty2.Text)
valx3 = Val(Textx3.Text)
valy3 = Val(Texty3.Text)
flimit = Val(flimit.Text)
valrepeat1 = Val(Textrepeat1.Text)
valpoints = Val(Textpoints.Text)
movebool = False
specbool = False
count = 0
s.fVzLimit = flimit
Call vSetSpectParam(s, 0)
Acquire.Enabled = False
send Val(2), "Output OFF", stat%
send Val(2), "Apply P25V," & Text1.Text & ",0.01", stat%
send Val(2), "Apply N25V,-" & Text1.Text & ",0.01", stat%
For run = 1 To valpoints
If (run = 1) Then
valx = valx1
valy = valy1
End If
If (run = 2) Then
valx = valx2
valy = valy2
End If
If (run = 3) Then
valx = valx3
valy = valy3
End If
For run2 = 0 To valrepeat1
If (Check2.Value = 0) Then
movebool = bMoveToXY(valx, valy, 100, XYMOVE_DIST)
If (Check5(0).Value = 1) Then
send Val(2), "Output ON", stat%
'For i2 = 1 To 15
' For i = 1 To 20000000
' Next i
'Next i2
For i2 = 1 To 2
For i = 1 To 20000000

```

```

Next i
Next i2
For i = 1 To 200000
Next i
specbool = bSampleSpectroscopy(IData(0), ipt(0), itypes(0), nHalf)
For i = 1 To 200000
Next i
'specbool = bSampleSpectroscopy(IData(0), ipt(0), itypes(0), nHalf)
'For i = 1 To 200000
'Next i
filename1 = path.Text + "volt\alpha\" + Str(run) + "_" + Str(run2) + ".txt"
filename2 = path.Text + "volt\r\" + Str(run) + "_" + Str(run2) + ".txt"
filename3 = path.Text + "volt\old\" + Str(run) + "_" + Str(run2) + ".txt"
Call vDrawGraph
End If
If (Check6(0).Value = 1) Then
send Val(2), "Output OFF", stat%
For i2 = 1 To 3
For i = 1 To 2000000
Next i
Next i2
specbool = bSampleSpectroscopy(IData(0), ipt(0), itypes(0), nHalf)
For i = 1 To 200000
Next i
filename1 = path.Text + "0\alpha\" + Str(run) + "_" + Str(run2) + ".txt"
filename2 = path.Text + "0\r\" + Str(run) + "_" + Str(run2) + ".txt"
filename3 = path.Text + "0\old\" + Str(run) + "_" + Str(run2) + ".txt"
Call vDrawGraph
End If
send Val(2), "Output OFF", stat%
runx = runx + valstepx - 1
count = count + 1
End If
Next run2
Next run

```

## 12.4) Datatreatment Software

After the acquisition of the FDC curves, extensive data treatment had to be performed, as described in the previously. The essentially matlab code for the final treatment is the following:

```
%Input
file = ['F:\']; %path
zscalediv = 2;
zscalexmax = -50;
zscalexmin = -750;
cal1nAnm = 0.063;
cal2nNnA = 1;
cut = -750;
xstart = 56000;
ystart = 19500;
xend = 56000;
yend = 39900;
decx = 10;
decy = 50;
%load
zscale = (zscalexmin:zscalediv:zscalexmax);
xscale = (xstart:decx:xend);
yscale = (ystart:decy:yend);
filenameline = [file 'linescan.mat'];
load (filenameline);
%max detection
steigval1 = 20;
steigdeg1 = 0.1;
posarea1 = 20;
steigval2 = 80;
steigdeg2 = 0.01;
posarea2 = 60;
%crossection
x = xstart;
y = ystart;
x2 = 0;
```

```

y2 = 0;
figure;
figure;
figure;
figure;
while x < xend + decx
x2 = x2 + 1;
    while y < yend + decy
        y2 = y2 + 1;
        stx = num2str(x);
        sty = num2str(y);
        %read files
        filename1 = [file '0\alpha\' stx '_' sty '.txt'];
        filename2 = [file 'voltage\alpha\' stx '_' sty '.txt'];
        fdca0 = dlmread(filename1, ';');
        fdcaV = dlmread(filename2, ';');
        figure(1);
        plot(fdca0(:,1), fdca0(:,2));
        hold all;
        plot(fdcaV(:,1), fdcaV(:,2));
        hold off;
        [m1,n1] = size(fdca0);
        %attraction part 0V
        total0 = 0;
        count0 = 0;
        clear run1 run2 run3 run2max steig minfdca0;
        for run1 = 1:m1
            if fdca0(run1,1) < cut
                total0 = total0 + fdca0(run1,2);
                count0 = count0 + 1;
            end
        end
        average0 = total0/count0;
        run2 = m1;
        run3 = 1;
        steig = fdca0(run2,2) - fdca0((run2-steigval1),2);
        while steig > steigdeg1
            steig = fdca0(run2,2) - fdca0((run2-steigval1),2);
            run2 = run2 - 1;
        end
        if (run2+posarea1)> m1

```

```

    run2max = m1;
else
    run2max = run2 + posarea1;
end
for run1 = (run2-posarea1):(run2max)
    minfdca0(run3,1) = fdca0(run1,1);
    minfdca0(run3,2) = fdca0(run1,2);
    run3 = run3 + 1;
end
[C0h,l0h] = min(minfdca0);
l0h(2) = find (fdca0(:,1) == minfdca0(l0h(2),1));
min0h = (m1-l0h(2));
for run1 = 1:min0h
    run2 = m1 - (run1 - 1);
    if fdca0(run2,2) > average0
        height10 = fdca0(run2,2);
        pos0 = fdca0(run2,1);
    end
end
height20 = fdca0(l0h(2),2);
attractionforce1 = height10 - height20;
attgradient0 = (fdca0(l0h(2)+10,2)-fdca0(m1,2))/(fdca0(l0h(2)+10,1)-fdca0(m1,1));
for run1 = 1:m1
    fdca0new(run1,2) = fdca0(run1,2) - average0;
    fdca0new(run1,1) = fdca0(run1,1) - (fdca0new(run1,2)/callnAnm) - pos0;
end
pos02(x2,y2) = pos0;
%attraction part with V
clear run1 run2 run3 run2max steig minfdcaV;
totalV = 0;
countV = 0;
for run1 = 1:m1
    if fdcaV(run1,1) < cut
        totalV = totalV + fdcaV(run1,2);
        countV = countV + 1;
    end
end
averageV = totalV/countV;
run2 = m1;
run3 = 1;
steig = fdcaV(run2,2) - fdcaV((run2-steigval2),2);

```



```

while steig > steigdeg2
    steig = fdcaV(run2,2) - fdcaV((run2-steigval2),2);
    run2 = run2 - 1;
end
if (run2+posarea2)> m1
    run2max = m1;
else
    run2max = run2 + posarea2;
end
for run1 = (run2-posarea2):(run2max)
    minfdcaV(run3,1) = fdcaV(run1,1);
    minfdcaV(run3,2) = fdcaV(run1,2);
    run3 = run3 + 1;
end
[CVh,IVh] = min(minfdcaV);
IVh(2) = find (fdcaV(:,1) == minfdcaV(IVh(2),1));
minVh = (m1-IVh(2));
for run1 = 1:minVh
    run2 = m1 - (run1 - 1);
    if fdcaV(run2,2) > averageV
        height1V = fdcaV(run2,2);
        posV = fdcaV(run2,1);
    end
end
height2V = fdcaV(IVh(2),2);
attractionforce2 = height1V - height2V;
attgradientV = (fdcaV(IVh(2)+10,2)-fdca0(m1,2))/(fdcaV(IVh(2)+10,1)-fdca0(m1,1));
for run1 = 1:m1
    fdcaVnew(run1,2) = fdcaV(run1,2) - averageV;
    fdcaVnew(run1,1) = fdcaV(run1,1) - (fdcaVnew(run1,2) /cal1nAnm) - posV;
end
%plot corrected FDCS
figure(2);
plot(fdca0new(:,1), fdca0new(:,2));
hold all;
plot(fdcaVnew(:,1), fdcaVnew(:,2));
hold off;
clear run1 run2 run3 run4 run2max steig minfdcaV;
%subtract FDCS and plot resulting graph
newpos0 = find(fdca0new(:,1) > -10, 1);
newposV = find(fdcaVnew(:,1) > -10, 1);

```

```

if isempty(newpos0) == 1 | isempty(newposV) == 1
    y = y + decy;
else
    fdca0new2(:,1) = zscale;
    fdcaVnew2(:,1) = zscale;
    fdca0new2(:,2) = interp1(fdca0new(1:newpos0,1),fdca0new(1:newpos0,2),zscale,'linear');%,
'extrap');
    fdcaVnew2(:,2) = interp1(fdcaVnew(1:newposV,1),fdcaVnew(1:newposV,2),zscale,'linear');%,
'extrap');
    figure(3);
    plot(fdca0new(:,1), fdca0new(:,2));
    hold all;
    plot(fdcaVnew(:,1), fdcaVnew(:,2));
    plot(fdca0new2(:,1), fdca0new2(:,2));
    plot(fdcaVnew2(:,1), fdcaVnew2(:,2));
    hold off;
    diff(:,1) = fdca0new2(:,1);
    diff(:,2) = fdca0new2(:,2) - fdcaVnew2(:,2);
    figure(4);
    plot(diff(:,1), diff(:,2));
    fdca0new3(x2,y2,:) = -fdca0new2(:,2);
    fdcaVnew3(x2,y2,:) = -fdcaVnew2(:,2);
    %correction for height (contact linescan)
    % scale change Volt to nm
    ind1 = find(linex2 == y);
    linerunconv(:,1) = linex2;
    linerunconv(:,2) = lineynew2;
    [CV1,IV1] = min(linerunconv);
    linerunconv(:,2) = linerunconv(:,2) - CV1(2);
    lineyval = linerunconv(ind1,1);
    linezval = linerunconv(ind1,2);
    [CV2,IV2] = max(linerunconv);
    [m2] = size(zscalnew2);
    m4 = m2(2);
    [m3,n3] = size(diff);
    pos = abs(find(zscalnew2 >=(zscalemax-linezval)));
    pos2 = pos(1);
    run4 = m3;
    for run3 = 1:m3
        diff2(x2,y2,(pos2-run4+1)) = diff(run3,2);
        run4 = run4 - 1;
    end
end

```

```

for run3 = 1:m3
    diff2old(x2,y2,run3) = diff(run3,2);
end
clear difftest;
difftest(:, :) = diff2(x2,y2,:);
figure(5);
plot(difftest);
%attraction force
attractionforce(x2,y2) = attractionforce2 - attractionforce1;
%gradient attraction part
attgradientVolt(x2,y2) = attgradientV;
attgradient0Volt(x2,y2) = attgradient0;
y = y + decy;
end
end
y2 = 0;
y = ystart;
x = x + decx;
end

```

## 12.5) Simulation Software

Each numerical simulation conducted in this thesis needs its own individual matlab code. In the following the matlab-comsol code for the numerical simulation of a tip with 500 nm radius on 500 nm pitch electrodes is presented. The code for the other pitches and tips is similar to it.

```

% COMSOL Multiphysics Model M-file
flclear fem
% COMSOL version
clear vrsn
vrsn.name = 'COMSOL 3.3';
vrsn.ext = 'a';
vrsn.major = 0;
vrsn.build = 511;
vrsn.rcs = '$Name: $';
vrsn.date = '$Date: 2007/02/02 19:05:58 $';

```

```

fem.version = vrsn;
% Geometry
% Import CAD data
garr = geomimport('E:\sim_newr4\tipigs\500nm.IGS');
[g1]=deal(garr{:});
% Geometry
g2=cadconvert(g1);
% Geometry
g2=scale(g2,1e-6,1e-6,1e-6,0,0,0);
g3=block3('5.0E-7','1.0E-5','1.0E-7','base','corner','pos',{2.23528E-6,-2.5E-6,6.5E-6},'axis',{0,0,1},'rot',0);
[g4]=geomcopy({g3});
[g5]=geomcopy({g4});
g5=move(g5,[1.0E-6,0,0]);
[g6]=geomcopy({g4});
g6=move(g6,[2.0E-6,0,0]);
[g7]=geomcopy({g4});
g7=move(g7,[3.0E-6,0,0]);
[g8]=geomcopy({g4});
g8=move(g8,[-1.0E-6,0,0]);
[g9]=geomcopy({g4});
g9=move(g9,[-2.0E-6,0,0]);
[g10]=geomcopy({g4});
g10=move(g10,[-3.0E-6,0,0]);
g11=block3('1.1E-5','1.1E-5','1.1E-5','base','corner','pos',{-3.01472E-6,-3.01472E-6,-4.2E-6},'axis',{0,0,1},'rot',0);
x = 1;
z = 1;
while x <= 22
while z <= 11
clear appl bnd equ fcns fem fem0 lib map s units vrsn l1 intbound;
% Analyzed geometry
clear s
s.objs={g2,g3,g5,g6,g7,g8,g9,g10,g11};
s.name={'CO1','BLK1','BLK2','BLK3','BLK4','BLK5','BLK6','BLK7', ...
'BLK8'};
s.tags={'g2','g3','g5','g6','g7','g8','g9','g10','g11'};
fem.draw=struct('s',s);
[fem,map]=geomanalyze(fem);
% (Default values are not included)
% Application mode 1
clear appl

```

```

appl.mode.class = 'ElectrostaticsGeneralized';
appl.module = 'ACDC';
appl.border = 'on';
appl.assignsuffix = '_emqv';
clear bnd
bnd.V0 = {0,0,-15.0,15};
bnd.type = {'r','V','V','V'};
bnd.ind = [1,1,1,1,1,3,3,3,3,3,2,2,2,2,4,4,4,4,4,3,3,3,3,3,2,2,4, ...
    4,4,4,4,4,2,3,3,3,3,3,4,4,4,4,4,3,3,3,3,3,3,1];
appl.bnd = bnd;
clear equ
equ.sigma = {0,'mat2_sigma','mat3_sigma'};
equ.ind = [1,2,3,2,2,2,2,2,2];
appl.equ = equ;
fem.appl{1} = appl;
fem.frame = {'ref'};
fem.border = 1;
clear units;
units.basesystem = 'SI';
fem.units = units;
% Library materials
clear lib
lib.mat{1}.name='Air, 1 atm';
lib.mat{1}.varname='mat1';
lib.mat{1}.variables.nu0='nu0(T[1/K])[m^2/s]';
lib.mat{1}.variables.eta='eta(T[1/K])[Pa*s]';
lib.mat{1}.variables.C='Cp(T[1/K])[J/(kg*K)]';
lib.mat{1}.variables.rho='rho(p[1/Pa],T[1/K])[kg/m^3]';
lib.mat{1}.variables.k='k(T[1/K])[W/(m*K)]';
lib.mat{1}.variables.cs='cs(T[1/K])[m/s]';
clear fcns
fcns{1}.type='inline';
fcns{1}.name='nu0(T)';
fcns{1}.expr='(-7.887E-12*T^2+4.427E-08*T+5.204E-06)/(1.013e5*28.8e-3/8.314/T)';
fcns{1}.dexpr={'diff((-7.887E-12*T^2+4.427E-08*T+5.204E-06)/(1.013e5*28.8e-3/8.314/T),T)'};
fcns{2}.type='inline';
fcns{2}.name='cs(T)';
fcns{2}.expr='sqrt(1.4*287*T)';
fcns{2}.dexpr={'diff(sqrt(1.4*287*T),T)'};
fcns{3}.type='inline';
fcns{3}.name='Cp(T)';

```

```

fcns{3}.expr='0.0769*T+1076.9';
fcns{3}.dexpr={'diff(0.0769*T+1076.9,T)'};
fcns{4}.type='inline';
fcns{4}.name='rho(p,T)';
fcns{4}.expr='p*28.8e-3/8.314/T';
fcns{4}.dexpr={'diff(p*28.8e-3/8.314/T,p)','diff(p*28.8e-3/8.314/T,T)'};
fcns{5}.type='inline';
fcns{5}.name='eta(T)';
fcns{5}.expr='-7.887E-12*T^2+4.427E-08*T+5.204E-06';
fcns{5}.dexpr={'diff(-7.887E-12*T^2+4.427E-08*T+5.204E-06,T)'};
fcns{6}.type='inline';
fcns{6}.name='k(T)';
fcns{6}.expr='10^(0.8616*log10(abs(T))-3.7142)';
fcns{6}.dexpr={'diff(10^(0.8616*log10(abs(T))-3.7142),T)'};
lib.mat{1}.functions = fcns;
lib.mat{2}.name='Ti';
lib.mat{2}.varname='mat2';
lib.mat{2}.variables.nu='0.36';
lib.mat{2}.variables.E='40e9[Pa]';
lib.mat{2}.variables.sigma='2.6e6[S/m]';
lib.mat{2}.variables.alpha='8.60e-6[1/K]';
lib.mat{2}.variables.C='522[J/(kg*K)]';
lib.mat{2}.variables.rho='4506[kg/m^3]';
lib.mat{2}.variables.k='21.9[W/(m*K)]';
lib.mat{3}.name='Pt';
lib.mat{3}.varname='mat3';
lib.mat{3}.variables.nu='0.38';
lib.mat{3}.variables.E='168e9[Pa]';
lib.mat{3}.variables.sigma='8.9e6[S/m]';
lib.mat{3}.variables.alpha='8.80e-6[1/K]';
lib.mat{3}.variables.C='133[J/(kg*K)]';
lib.mat{3}.variables.rho='21450[kg/m^3]';
lib.mat{3}.variables.k='71.6[W/(m*K)]';
fem.lib = lib;
zposstart = 0.040E-6;
xposstart = -1.5E-6;
zpos = zposstart + ((z-1)*0.04E-6);
xpos = xposstart + ((x-1)*0.1E-6);
col = drawgetobj(fem,'CO1');
fem = drawsetobj(fem,'CO1',move(col,xpos,0,zpos));
[fem,map]=geomanalyze(fem);

```

```

fem.lib = lib;
% Multiphysics
fem=multiphysics(fem);
% Initialize mesh
fem.mesh=meshinit(fem, ...
    'hauto',6);
% Extend mesh
fem.xmesh=meshextend(fem);
% Solve problem
fem.sol=femstatic(fem, ...
    'solcomp',{'V'}, ...
    'outcomp',{'V'});
pause(1);
% Integrate
intbound(1) = find(map{3,1} == 12);
intbound(2) = find(map{3,1} == 13);
intbound(3) = find(map{3,1} == 14);
intbound(4) = find(map{3,1} == 15);
intbound(5) = find(map{3,1} == 28);
intbound(6) = find(map{3,1} == 29);
intbound(7) = find(map{3,1} == 36);
F5(x,z) = postint(fem,'(nD_emqv * Ez_emqv)', ...
    'unit','N', ...
    'dl',intbound, ...
    'edim',2);
numx = num2str(x);
numz = num2str(z);
string = strcat('E:\sim_newr4\500nmpitch\500\mat',numx,'_',numz,'.mat');
save(string);
pause(1);
z = z + 1;
end;
x = x + 1;
z = 1;
end;

```





## *Acknowledgements*

Many people have contributed in different ways to the achievement of this work. I thank you all for your help and for your support during these four and a half years! First, I need to thank Patrik, without whom I would never have started a PhD. Thank you for your motivation, expertise and help. Special thanks to Christian Santschi for the long and never-ending days of FIB and FEB sessions and the fruitful discussions. I would like to thank all the colleagues of the Institute for the nice atmosphere on this 4th floor. I thank as well Claude and Ronald, the technical staff of the Institute, who had always an open ear for my crazy ideas. Thanks as well to our secretaries, Yvette, Manuelle, and Doris, for the superb secretary service. All the staff from CMI is thanked for their, help, advices, machine trainings and open mind for new ideas. I thank Nicolas Xanthopoulos for the XPS and Auger investigations. All the students involved in semester or master projects (3 in total) are appreciatively acknowledged for their contributions. Special thanks as well to Cornelia, my girlfriend, for her support and patience during the writing time. I want to thank my mother, my father and my sister for being who you are, for believing in me and for your full support since ever.



## *Scientific Publications*

- **Jenke, M.G.**, C. Schreiter, Kim G. M., Vogel H., Brugger J., *Micropositioning and microscopic observation of individual picoliter-sized containers within SU-8 microchannels*. Microfluidics and Nanofluidics, 2007. **3**(2): p. 189-194.
- Danelon, C., **Jenke, M.G.**, et al., *Micro- and nanostructured devices for the investigation of biomolecular interactions*. Chimia, 2006. **60**(11): p. A754-a760.
- Santschi, C., **Jenke, M. G.**, Hoffmann, P., Brugger, J., *Interdigitated 50 nm Ti electrode arrays fabricated using XeF<sub>2</sub> enhanced focused ion beam etching*. Nanotechnology, 2006. **17**(11): p. 2722-2729.
- **Jenke M. G.**, Santschi, C., Hoffmann, P., *Characterization of Electrical Fields of Buried Interdigitated Nanoscale Ti-Electrode Arrays by a Novel Atomic Force Microscopy Measurement Procedure and Their Fabrication by FIB Milling*. NSTI-Nanotech2007, 2007. **4**: p. 97-100.
- **Jenke M. G.**, Santschi, C., Hoffmann, P., *Two-dimensional electrostatic force field measurements with simultaneous topography measurement on embedded interdigitated nanoelectrodes using a force distance curve based method*. Applied Physics Letters, 2008. **92**(6): p. 063113-3.

## *Conference Presentations*

- **Jenke, M.G.**, C. Schreiter, Kim G. M., Vogel H., Brugger J., *Transparent Multilayer SU-8 Patch Clamp Chip With Microfluidic Network*. EUROMAT, 2003
- **Jenke M. G.**, Santschi, C., Hoffmann, P., *Characterization of Electrical Fields of Buried Interdigitated Nanoscale Ti-Electrode Arrays by a Novel Atomic Force Microscopy Measurement Procedure and Their Fabrication by FIB Milling*. NSTI-Nanotech, 2007



# *Curriculum Vitae*

Nationality: German

Martin Jenke

Date of Birth: 10.04.1976

Frankfurter Str. 26  
D-84513 Töging / Inn

Single

E-Mail: [MartinJenke@web.de](mailto:MartinJenke@web.de)



## Education

### **PhD in Nanotechnology (2008)**

Swiss Federal Institute of Technology EPFL, Lausanne, Switzerland

### **Engineer in Physical Engineering with main focus on Microtechnology (2003)**

University of Applied Sciences Munich, Munich, Germany

## Key Skills

### **Micro- and Nano-scale production technologies:**

- Focused electron and ion beam induced processing techniques (lithography, deposition and etching).
- AFM Expert: calibration of AFM cantilevers (Sader, Cleveland, counter cantilever...), experience with divers modes (contact, non contact, tapping, friction, force distance curves).
- Cleanroom standard equipments and processes for integrated devices production and research.
- Standard machining techniques for micro-devices.
- Micro- and Nano-scale investigation techniques for surface characterization: SEM, TEM, XPS, contact angle.
- Manipulation of surface forces by chemical coatings. (SAM, Polymers)
- Fabrication and Characterization of Microfluidic and Biotechnology devices.

### **Academic / Teaching experiences:**

- Co-adviser for 4 master and semester projects for undergraduate students on various topics (biotechnology, micro- / nanotechnology).
- Assistant and examination expert for Bachelor and Master students for the following topics: Surface Chemistry, Nanotechnologies, Microtechnology.

**Computer skills:**

- Modeling using Matlab, Microcal Origin, Femlab (Comsol), Solid Works.
- Windows and Linux operative systems.
- Programming using Delphi, Visual Basic, Labview, C++, Dreamweaver.

**Languages:**

German (mother tongue), English (good), French (fair), Dutch (basic)

**Professional Experiences**

2003 to 2008	PhD at EPFL (Swiss Federal Institute of Technology Lausanne) in the field of Surface- and Nanoengineering (LOA/NRG) (Prof. Dr. René-Paul Salathé, Supervisor: MER Dr. Patrik Hoffmann; Jury: Prof. Dr. Bharat Bhushan, Prof. Dr. Ernst Meyer, Prof. Dr. Andreas Stemmer, Prof. Dr. Cécile Hébert)
2002 to 2003	Research Assistant at EPFL (Swiss Federal Institute of Technology Lausanne) in the field of Microengineering and Biotechnology (LMIS1) (Ass. Prof. Jürgen Brugger)
2000 to 2002	Infineon Technologies (Division: Corporate Research – Nano Processes) (Internship and Student Trainee)
2000	PTS Munich (Research centre for paper technologies) (Student Trainee)
1998	InfraServ Gendorf (formerly: Hoechst AG Gendorf) (Internship)